

AD-A203 665

SUPPORT OF MARK III OPTICAL INTERFEROMETER

Contract F00014-86-C-2105

Final Report

For the period 1 December 1985 through 31 May 1988

DTIC
SELECTED
JAN 11 1989
Dcs

Principal Investigator
Dr. Michael Shao

November 1988

Prepared for
National Research Laboratory
Washington, DC 20375

DISTRIBUTION STATEMENT A

Approved for public release
Distribution Unlimited

Smithsonian Institution
Astrophysical Observatory
Cambridge, Massachusetts 02138

The Smithsonian Astrophysical Observatory
is a member of the
Harvard-Smithsonian Center for Astrophysics

The NRL Technical Officer for this contract is Dr. Kenneth
Johnston, Code 4103, NRL, Washington, DC 20375.

88 12 12 066

↓

In the three year period of this contract we have built and installed a long baseline stellar interferometer on Mt. Wilson. A number of papers describing the instrument and results from that instrument have appeared [Shao et al. Astronomy and Astrophysics 193(1988):357; Shao et al. Astrophysical Journal 327(1988):905; Colavita et al. Applied Optics 26(1987):4106; Colavita et al. Applied Optics 26(1987):4113; Mozurkewich et al. Astronomical Journal 95(1988):1269]. The Mark III interferometer is the most astronomically productive interferometer to date. The success of the Mark III has led the USNO to decide to build a dedicated four element interferometer array for fundamental astrometry and NRL/ONR to build a six element imaging array.

To summarize the last three years, we list the major milestones.

- 9/86 first fringes with 12M N-S baseline
- 11/86 automated operation (165 obs/night)
- 11/86 first precise diameter measurements
- 5/87 8.6M E-S baseline in operation
- 7/87 star tracker using photon camera and correlation centroid estimator put into operation
- 8/87 modifications to enable simultaneous astrometric and diameter measurements
- 9/87 install laser metrology system
- 5/88 12M E-S baseline
- 5/88 design and build variable baseline (3-30 meters) components
- 6/88 design and build group delay correlator

In conclusion, we have successfully completed the task of building a long baseline interferometric observatory.

①

	<input checked="" type="checkbox"/> <input type="checkbox"/> <input type="checkbox"/>
By <i>per lti</i>	
Distribution /	
Availability Codes	
Dist	Avail and/or Special
A-1	

The Mark III stellar interferometer

M. Shao¹, M. M. Colavita¹, B. E. Hines², D. H. Staelin², D. J. Hutter³, K. J. Johnston³, D. Mozurkewich³, R. S. Simon³, J. L. Hershey⁴, J. A. Hughes⁴, and G. H. Kaplan⁴

¹ Smithsonian Astrophysical Observatory, 60 Garden Street, Cambridge, MA 02138, USA

² Massachusetts Institute of Technology, Department of Electrical Engineering and Computer Science, Cambridge, MA 02139, USA

³ E. O. Hulburt Center for Space Research, Naval Research Laboratory, Washington, DC 20375, USA

⁴ US Naval Observatory, Washington, DC 20390, USA

Received May 25, accepted July 23, 1987

Summary. The Mark III interferometer is an operational long baseline stellar interferometer on Mt. Wilson with four possible baseline configurations from 9 m NE-SW to 20 m N-S. The interferometer was designed to be a highly automated astronomical instrument to measure stellar positions and diameters to a magnitude limit of seven. Initial fringe observations were made in September 1986 with a 12-m N-S baseline. In the following months, semi-automated astrometric and stellar diameter measurements were also made. This paper describes the hardware and software components of the instrument and its operational characteristics.

The interferometer has several novel features. One is the use of optimal estimation and control algorithms (e.g. Kalman filters) in the control loops. Another is the ability to operate both as a closed-loop phased interferometer and eventually as an open-loop or absolute coherent interferometer. High thermal stability and mechanical accuracy should permit the instrument to point blind at an astronomical object and maintain optical path equality to within the limits set by the atmosphere. In this absolute interferometric mode of operation, it should be possible to observe faint astronomical objects that are too dim for phase tracking. In theory, measurements of amplitude, group delay, and closure phase will be possible to 14 mag.

Key words: stellar interferometry - astrometry - stellar diameters - optical array - proper motion

1. Introduction

The Mark III interferometer is the third of a series of stellar interferometers at Mt. Wilson Observatory. The first instrument demonstrated white-light fringe tracking in 1979 (Shao and Staelin, 1980). The second instrument observed fringes in 1982 and was used as a technology test bed for astrometric measurements until 1984 (Shao et al., 1987). Several devices critical to the operation of a stellar interferometer were developed for the Mark II interferometer. One such device was a high speed, ultra high accuracy, laser controlled optical delay line. An operational procedure for rapid switching between stars was also developed.

Send offprint requests to: M. Shao

Traditionally, the most difficult task of a stellar interferometer has been finding and tracking the central fringe. In rapid switching, this procedure is totally automated. Thus, operation of the Mark II helped identify the technical problems of making astrometric measurements with a long baseline interferometer.

Like the previous instrument, the Mark III interferometer was also designed to be a test bed for new techniques and technologies relevant to optical interferometry and synthetic optical aperture synthesis. However, the principal purpose of the Mark III interferometer was to initiate a test program of fundamental astrometric measurements to demonstrate a significant improvement in accuracy. Another goal was to initiate a program of accurate stellar diameter measurements. Most important of all, the instrument was designed to be astronomically productive.

Long baseline stellar interferometers have traditionally been considered one of the most technologically challenging astronomical instruments. In the Mark III interferometer, the goal has been to build an instrument that is reliable, easy to operate, and capable of extremely accurate astronomical measurements. In order to achieve these goals, a number of active subsystems were incorporated into the design of the instrument. In implementing these subsystems, the design philosophy involved keeping the mechanical and optical systems as simple as possible and shifting the bulk of the complexity into software.

Although the Mark III was originally designed as a closed loop phased interferometer, operational experience has shown that it has sufficient accuracy and stability to operate as an absolute interferometer. An absolute interferometer is one whose mechanical accuracy and stability in open loop operation, without fringe tracking, is sufficiently high that optical path errors are dominated by atmospheric turbulence. This level of accuracy and stability, usually associated with the primary mirror of a large astronomical telescope, is the level of accuracy exhibited by the Mark III interferometer with the 12-m baseline. Operation with the 20-m baseline is expected to exhibit the same level of accuracy and stability.

The ability to operate as an absolute interferometer makes possible three new modes of interferometric observations for long baseline interferometers. They are photon starved amplitude measurements, photon starved group delay astrometry, and photon starved closure phase measurements. Photon starved amplitude measurements have long been a part of speckle interferometry with single apertures. The importance of photon



Fig. 1. The Mark III interferometer on Mt. Wilson

starved observations is that they make possible astrometry and aperture synthesis of faint extragalactic objects. These three types of measurements are discussed after the description of the instrument.

2. The instrument

The interferometer is located in California on Mt. Wilson approximately 80 m east of the 100-inch telescope, near the site of the Mark II interferometer. Figure 1 shows a view of the site. Six and ten meters north, south, and east of the central building are the siderostat piers, which are each constructed of steel-reinforced concrete with a 4 x 4 foot base and a height of 8 feet, 4 feet of which is above ground. Siderostats are currently mounted on the innermost piers. Huts provide weather protection for the siderostats. These have hinged roofs which swing back exposing the siderostats to the sky. Currently, there are vacuum pipes between the huts and the central building to eliminate local seeing effects caused by heat in the main building. Initial operation involved only the 12-m baseline connecting the north and south siderostats; however, the east siderostat can be used in place of the north siderostat for a 9-m NE-SW baseline. The fourth window on the central building is for future expansion. In 1988, we plan to operate on the outer set of piers shown in Fig. 1, with 20-m N-S and 16-m NE-SW baselines.

Since the instrument's principal purpose is large angle astrometry, attention was paid to construction practices that affect astrometric accuracy. The central building is air conditioned during the day so that at night there will be a minimum temperature difference between inside and outside. The piers in the huts that hold the siderostats go down to bedrock and are not directly connected to the concrete pads on which the huts are built. The piers are also insulated by two inches of foam. The optics inside the main building that affect astrometric measurements are all located on a super-invar breadboard, except the mirrors in the optical delay line. However, the position of the optical delay line is monitored by a laser interferometer referenced to the same super-invar breadboard. The laser is frequency stabilized with better than 10^{-9} long-term stability.

The instrument can be divided into five subsystems: 1) the star tracker or autoguider, 2) the optical delay line, 3) the stellar fringe

acquisition and tracking system, 4) the laser metrology system, and 5) the siderostat pointing and observation sequencing system. A description of the optical layout of the instrument is followed by a more detailed explanation of the five subsystems.

2.1. Optical layout

Figure 2 is an optical schematic of the interferometer. Light from the two siderostats is directed toward the central building by fixed mirrors. These fixed mirrors are necessary to keep the polarization vectors from the two interfering beams parallel for observation of stars located over all parts of the sky. After the light enters the main building, the beams are directed by piezoelectrically controlled mirrors towards the vacuum delay lines. After the light reflects from the delay line retroreflectors, the beams are combined at the beamsplitter B. After the beamsplitter, part of the light is directed into optical fibers which feed GaAs phototubes located some distance from the central breadboard, and part of the light is directed toward the star tracker. Other optical components include the laser interferometers, and alignment lasers and telescopes.

2.2. Star tracker

The star tracker has been described in detail previously (Clark et al., 1986; Clark, 1986) and we will provide only a brief summary here. The star tracker system is designed to keep the two interfering wavefronts parallel to within a small fraction of an arcsecond. As with all servo systems, the star tracker is composed of an error sensor, a controller, and an actuator. For the Mark III interferometer, two different error sensors were built because a key component (a photon counting camera) for the original design was not delivered before initial observations were made in September 1986. Only the star tracker design that will be permanently attached to the interferometer is described.

An optical schematic of the star tracker is shown in Fig. 3. Light from the star in a 3-inch beam, intercepted by the two siderostats, is combined at a beamsplitter. Light from the south siderostat passes through an annular wedge that deflects the outer portion of the beam by 45° ; the inner 2-inch part of the beam is undeflected. After the light is combined at the beamsplitter, an annular mirror at one output of the beamsplitter directs the light in the annulus towards a telescope and imaging detector. The light in the central 2-inch core from both sides of the beamsplitter is fed to photomultipliers that detect the fringes.

When the two components of the light beam that enter the fringe detection phototubes are parallel (as they must be for proper operation of the interferometer), the two components of the annular beam entering the telescope will be tilted by 45° relative to each other because of the 45° wedge in the south arm of the interferometer. Thus two star images will appear on the face of the photon counting imaging detector. The optical arrangement of this star tracker is slightly different from that used for some other interferometers. The present design using one telescope for both star trackers eliminates the need to align the two optical systems to each other with subarcsecond accuracy. More important, the relative alignment of two separate optical systems would drift with time and temperature, whereas the star trackers for the Mark III interferometer will maintain alignment indefinitely.

The photon camera used in the star tracker is a commercial detector based on the PAPA camera (Papaliolios et al., 1985) with 256×256 pixels. The detector produces a pulse with an x, y address for every detected photon. The digital output of the

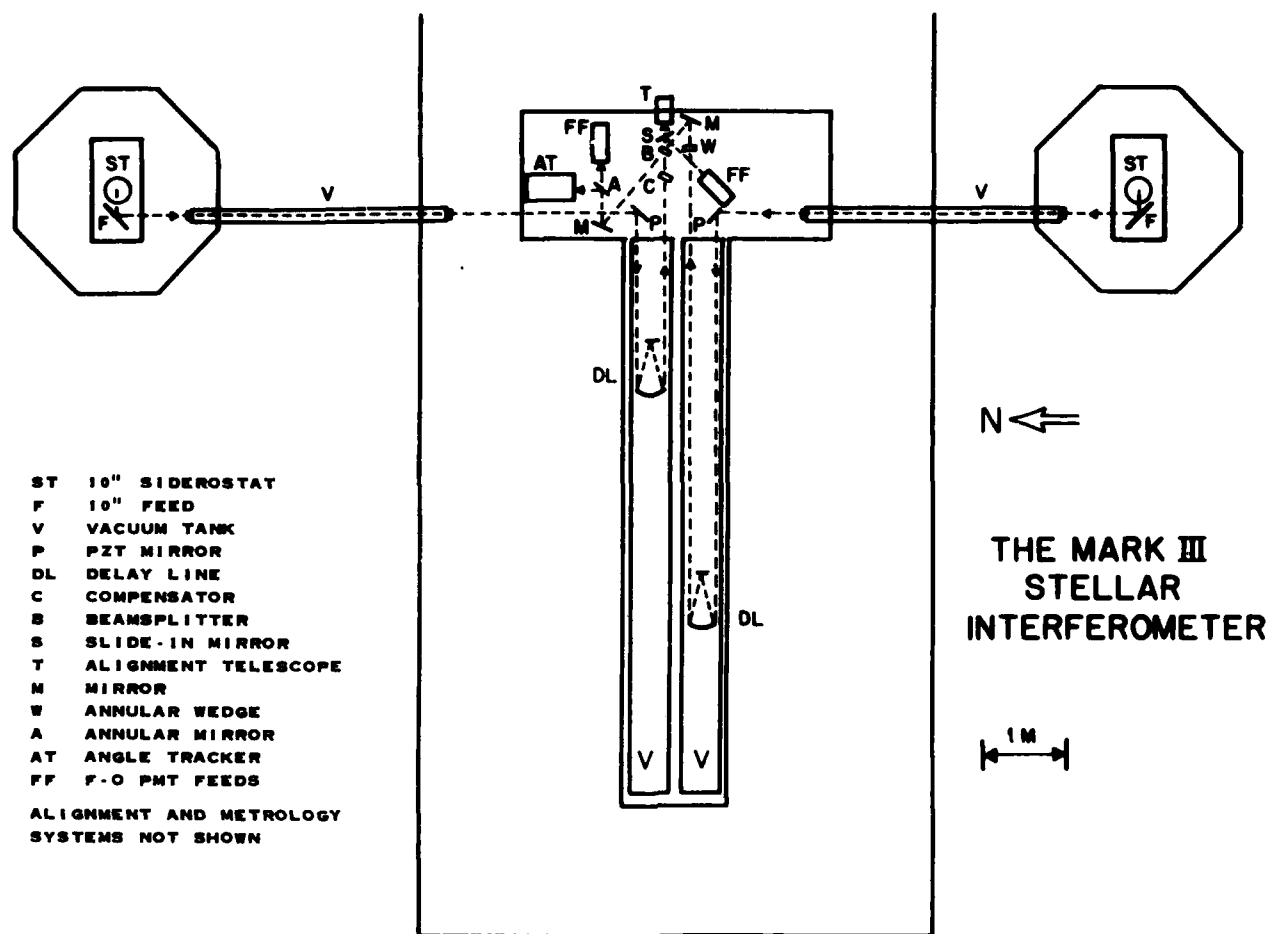


Fig. 2. Optical schematic of the Mark III interferometer

camera is interfaced to a high speed signal processor which locates the centroids of the two stellar images. Two additional optical, mechanical components are shown in Fig. 3. The variable neutral density filter is used to reduce the photon flux to the camera to prevent overloading of the camera electronics when observing bright stars. The setting of the filter is controlled by the star tracker computer. There are also two shutters, one in each arm of the interferometer, which are used for star acquisition. When the siderostats stop slewing, the two stellar images may be sufficiently far from their correct positions that proper identification, i.e., which star came from which siderostat, may not be possible. The shutters are used to remove this ambiguity.

The camera is the error sensor. The actuator is a PZT-driven gymbaled mirror. This 5-inch mirror is driven in two orthogonal directions with a 30" peak-to-peak motion. The bearings are cross flexure pivots and the mirror mount has its lowest resonance at 200 Hz.

The heart of the star tracker is the control system; it makes extensive use of optimal estimation techniques and only a brief outline is given here. A detailed description is given by Clark et al. (1986). The control problem is separated into a spatial filtering part and a temporal filtering part. The spatial filter takes the photon addresses generated by the photon camera and derives the

centroid of the star. The temporal filter takes current and past centroid estimates and generates a set of voltages to drive the piezoelectric actuators.

The image of the star on the camera face is the diffraction pattern of an annular telescope aperture. A cross-correlation centroid estimator was implemented. The estimated x coordinate of the centroid is given by

$$\hat{x} = \iint f(x, y) h_x(x, y) dx dy. \quad (1)$$

where f is the detected image and h_x is the correlation function for the x direction. The noise in the detected image is photon noise with a variance given by

$$\sigma_f^2 = f(x, y). \quad (2)$$

Since the theoretical shape of the image is known, there is a closed form solution for the optimal correlation function, i.e., that function $h(x, y)$ which gives a minimum variance for \hat{x} due to photon noise in the measurement of $f(x, y)$. The optimal correlation function is given by

$$h_{opt}(x, \beta) = \frac{[-\partial f(x, \beta) / \partial x]}{f(x, \beta)}. \quad (3)$$

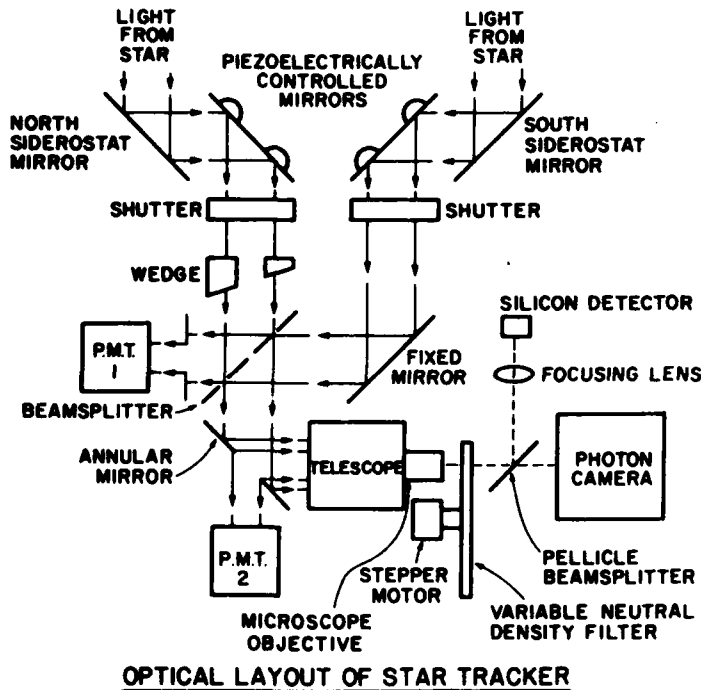


Fig. 3. Optical schematic of star tracker

Table 1

Correlation function	Single photon variance (arcsec) ²
Optimal [Eq. (3)]	0.303
Quad cell [Eq. (4)]	3.09
Linear [Eq. (5)]	6.14

This type of centroid estimator has limited dynamic range but very low variance. An analysis of this estimator for our annular aperture image was made relative to centroid estimators using quad cell and linear correlation functions:

$$\text{Quad cell: } h = \begin{cases} +1 & x > 0 \\ -1 & x < 0 \end{cases} \quad (4)$$

$$\text{linear: } h = x \quad (5)$$

The results are shown in Table 1. Note that the variance for the optimal correlator estimator is about an order of magnitude better than a quad cell.

The correlation integral [Eq. (1)] is performed by a custom digital signal processor. The processor calculates the integral on a photon by photon basis, rather than a pixel by pixel basis. This is more efficient computationally when the number of detected photons is much less than the number of pixels in the image. Currently, centroid estimates are calculated every 10 ms. The signal processor can operate at photon rates well above the capabilities of the camera. The optical correlation functions, one in x , and one in y for each of the two trackers are downloaded to the correlation processor from the main control computer. The

calculation of the optimal correlation function is not done in real time.

The second part of the control system is the temporal filter. While the spatial filter is implemented mostly in digital hardware and microcode, the temporal filter is implemented entirely in software on the star tracker control computer. The temporal filter is a discrete time Kalman filter. The Kalman filter assumes a state variable formulation of the tracking problem and is the linear filter which minimizes the mean square tracking error. This filter takes into account the observation noise (photon noise) by adaptively varying the tracker bandwidth according to the noise variance. The output of the filter is scaled and then directed to a D/A converter and high voltage amplifier to drive the PZTs.

In addition to the software for the Kalman filter, there is software for acquisition, data recording, and for utilities such as moving the shutters and controlling the camera. There is also software for complete automatic operation and for off-line diagnostics and analysis of tracker performance.

2.3. Optical delay line

Two optical delay lines are used to equalize the paths from the star to the beamsplitter via the two siderostats 12 m apart. The mechanical and optical arrangement is shown in Fig. 4. The mechanical design is similar to that used in delay lines for high resolution Fourier spectroscopy (Connes, 1975). The optical delay is changed by moving cat's eye retroreflectors along tracks which are housed in two 25-ft vacuum chambers. The peak-to-peak optical path difference of this system is 20 m, and the delay lines can be positioned under laser control to an accuracy of 10 nm, for a dynamic range of $2 \cdot 10^9$ resolution elements in optical path difference. The maximum slew rate is 1 m per second of optical path difference. Twenty seconds is required to go from one end to

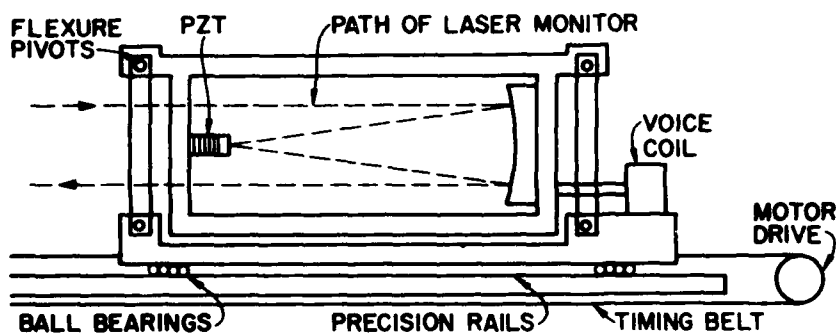


Fig. 4. Three stage (PZT, Voice Coil, Motor) optical delay line

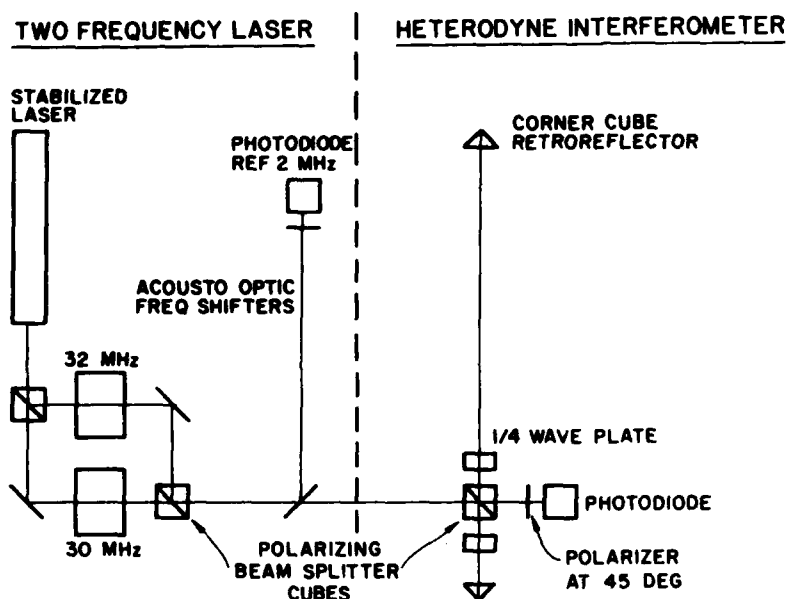


Fig. 5. Heterodyne laser interferometer for delay line

the other. The maximum tracking rate is 2 mm s^{-1} , at which point the rms position accuracy has degraded to 20 nm.

Figure 4 shows the optical path of the laser beam that measures the position of the cat's eye retroreflector. The cat's eye is an 8-inch $f/3$ parabola with a 1-inch flat mirror at its focus. The 1-inch mirror is mounted on a PZT stack that has a $5\text{-}\mu\text{m}$ peak-to-peak range. The cat's eye is suspended on a flexure bearing over a belt driven translation stage. A voice coil positions the cat's eye over the stage, while a motor at one end of the 25-ft track moves the stage via a timing belt. The voice coil has a 2-mm range and the motor has a $9\text{-}\mu\text{m}$ step size. The three actuators - PZT, voice coil, and motor - have considerable overlap in terms of resolution and dynamic range.

The delay line sensor is a heterodyne laser interferometer (Fig. 5). The light from a stabilized laser is split into two beams by a polarizing beamsplitter. They are then frequency shifted by two acousto-optic bragg cells with a 2-MHz frequency difference. When recombined, the beam has its two orthogonal polarizations at different frequencies with a 2-MHz frequency difference. The laser is a commercial transverse Zeeman stabilized HeNe laser with a one-day stability of 200 kHz at line center, 474 THz. The

interferometer is a standard polarization heterodyne interferometer. The phase of the 2-MHz signal from the interferometer is compared to the 2-MHz reference (Fig. 5) and a one wavelength change in the monitored optical path causes a 2π change in the relative phases of the interferometer and reference 2-MHz signals. A custom digital phase comparator circuit counts the fringes with $\lambda/64$ resolution at a maximum slew rate of $2 \cdot 10^6$ fringes per second.

Since the desired optical path difference is given by the difference between the positions of the two delay lines, it is only necessary to actively control one delay line. Thus, vibrations in one delay line are compensated by driving the other in exactly the same way.

The laser interferometers are read at a 1-kHz rate by the fringe tracker computer. The difference between the two interferometers is the measured position, which is subtracted from the desired position to give an error signal. The PZT servo is a simple first-order system, i.e., the PZT drive voltage is just the integral of the error signal. The necessary integral is performed in digital hardware, and the velocity of the PZT mirror is updated every millisecond by the computer. The closed-loop bandwidth of this

servo is approximately 100 Hz, for a time constant of 1 to 2 ms. The small-signal bandwidth of the entire delay line is the bandwidth of this innermost servo.

The voice coil servo is designed to keep the PZT system within its 5- μm dynamic range. The cat's eye flexure suspension has a 1.5-Hz resonance. Since a 5- μm accuracy requires a response significantly faster than 1.5 Hz, the voice coil servo has to be at least a second-order servo. The voice coil servo is implemented entirely in software. The error signal input to the voice coil servo is the distance the PZT mirror is from the center of its range. The output is a current to the voice coil. The closed-loop bandwidth of this servo is approximately 10 Hz.

The motor servo is designed to keep the voice coil in the center of its range. The input to this servo is the position of the voice coil as measured with a lateral-cell transducer. The motor is a microstep-driven stepper motor, interfaced to the computer through a programmable pulse generator. In the tracking mode, it operates as a first-order servo, with a small-signal closed-loop bandwidth of about 1 Hz.

The delay line control system was designed to interact with the rest of the interferometer through a simple interface. The rest of the interferometer does not see three separate actuators and control loops and a laser interferometer. Rather, the delay line subsystem is programmed by setting its position and velocity. At a given time, the delay line is programmed to move to a given position. Thereafter, the optical delay is changed at a rate determined by the programmed velocity. The delay line will move at this rate until the programmed position or velocity is changed.

The composite three-stage servo system has a moderately high bandwidth when the error signal is small (i.e., when delay line position minus target position is less than about 4 μm). However, when switching from one star to the next, the programmed position can suddenly change by 15 m. Since the PZT and voice coil have small dynamic ranges, and in addition have limits on their velocity and acceleration, these servo systems will not behave properly in response to such a large step. Left uncorrected, the resultant oscillations are sufficiently violent to misalign optics. Therefore, in addition to the linear tracking mode of operation described above, the delay line has several other modes of operation. A significant portion of the delay line servo code detects input conditions which would require a change in the servo mode so that the delay line remains well behaved under all conditions.

Table 2 shows the various modes of operation of the three delay-line loops. The modes of the various servos depend on the inputs to the delay line. Rapid changes in the programmed position or velocity is the usual reason for changes in operating mode. Hysteresis in the transition thresholds prevents oscillations caused by changes in the servo parameters between modes. Inputs from the limit switches can also cause changes in the servo modes. For example, two limit switches are used at each end of the track. The first informs the computer that the delay line should start decelerating in order to prevent the delay line from moving beyond the second limit switch, which disables the motors. Other interlocks prevent the laser fringe counter from running at 2 million fringes per second, taking the delay line with it, if the laser becomes misaligned. For a more detailed description of the delay line, the reader is referred to Holm (1986).

2.4. Stellar fringe detector

With proper operation of the star tracker and delay line, the two beams combined at the beamsplitter should interfere. This section

Table 2. Inputs: target position, target velocity, current laser positions (2), limit switches (8), voice coil position

Servo	Modes		
PZT	Linear track	Off	
Voice coil	Linear track	Damp	Off
Motor	Linear track	Accel./decel.	Constant vel. Off

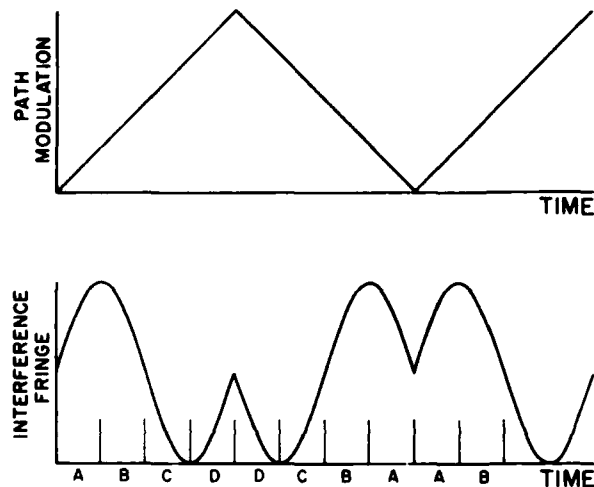


Fig. 6. Stellar fringe modulation demodulation

describes the procedure by which the amplitude and phase of the interference pattern are measured.

In the Mark III interferometer, the interfering wavefronts are parallel. Hence, the two outputs of the beamsplitter are uniform over the aperture and complementary. If the phase difference is 90 degrees, all then light will go to one of the two outputs; if the phase difference is -90 degrees, the light will go to the other output.

The fringe detection algorithm has been described previously (Shao and Staelin, 1977). The basic technique uses path length modulation and synchronous demodulation. The PZT controlled mirror in one of the vacuum delay lines is modulated with a 500-Hz triangle wave. If the path difference in the two arms of the interferometer is within the coherence length of the light (a few wavelengths), the intensity of light at the output of the beamsplitter will be as shown in Fig. 6. During one sweep of the PZT, the detected photons are grouped into four time bins denoted by A, B, C, and D. The amplitude and phase of the fringe are given by

$$\phi = \tan^{-1} \left(\frac{D - B}{C - A} \right) - \frac{\pi}{4} \quad (6)$$

$$\text{Amp} = \sqrt{(C - A)^2 + (D - B)^2} \quad (7)$$

In the above equations, the $C - A$ and $D - B$ terms are the sine and cosine components of the fringe.

The measured phase is unwrapped so that if the atmosphere moves the fringe position beyond $\pm\pi$, the correct error signal will

be used to track the fringe. The unwrapped phase is used as the error signal in a first-order servo. As mentioned before, the delay line is programmed by position and velocity. The unwrapped phase times a gain term is added to the previous programmed position of the delay line to yield the new programmed position. The programmed velocity is the sidereal rate. The closed-loop bandwidth of this servo is about 20 Hz. A similar fringe tracker was used on the Mark I and Mark II interferometers to track stellar fringes.

The fringe tracking servo, implemented entirely in software, is the simplest part of the stellar fringe detection subsystem. Other software components of the fringe detection subsystem perform functions such as stellar fringe search and initial acquisition, fringe recovery after tracker failure, central fringe identification, and automatic transition between operating modes. In addition to the above software components, other system components that affect the operation of the stellar fringe detector are the PZT stroke servo, and the optics for two color fringe measurements and for accurate visibility measurements.

The instrument was designed to make accurate astrometric measurements and accurate stellar diameter measurements on as many stars as possible. The design of a stellar fringe tracker is complicated by the fact that the requirements of high tracker sensitivity, low systematic astrometric error, and low visibility errors are not entirely consistent.

The stroke of the PZT can be varied by one of the control computers. Since the piezoelectric constant is temperature dependent, the peak-to-peak amplitude of the PZT triangle wave is monitored with a laser interferometer and the drive voltage is adjusted to maintain the proper amplitude to within 0.5 nm. For stellar diameter measurements, the stroke is set at the effective wavelength of the narrow bandpass filter. For astrometry, the stroke is set at the effective wavelength of the red channel.

When the interferometer is set to point at a star, the delay line is programmed to go to the expected position of the fringe plus 60 μm . From past experience, the calculated fringe position is never more than 30 μm in error if the baseline vector used in the calculation is derived from stellar fringe data less than a week old. The delay line is programmed to scan for the fringe at approximately 60 μm per second. The fringe amplitude is calculated every atmospheric coherence time, and if a fringe is detected, the scan is stopped and the servo turned on.

When the tracker loses the fringe, the delay line is moved back 5 μm and a search is restarted. After initial fringe acquisition, the search space is restricted to a 20- μm interval centered about the most recent position where the fringe was found. All of these search parameters are superimposed on the fringe motion due to earth rotation, which is calculated using a baseline vector typically derived from the previous night's data. When the seeing is exceptionally good, i.e., sub-arc-second seeing, the fringe tracker will stay locked on one fringe for many minutes, for up to 10^5 atmospheric coherence times.

If the fringe stays locked for more than one second, a central fringe identification algorithm is enabled. The visibility during that one-second interval is compared with a threshold. If the visibility is below the threshold, it is assumed that the tracker is on the wrong fringe and the tracker will jump one fringe to the right or left. The direction of the tracker jumps is determined by the visibility gradient. Since the tracker has an rms phase error of about 1/6 of a fringe, the visibility gradient can be determined by looking at the distribution of visibility versus phase. Since the central fringe has the highest visibility, the tracker will usually hop in that direction.

The operation of the various systems which comprise the star light fringe detector requires that a number of quantities: phase, amplitude, SNR, visibility gradient, etc. be calculated in real time. Although the system is rather complicated, the resulting tracker is extremely robust. The interferometer can be commanded to point at a star and the tracker will lock onto the fringe within 90 s. Thus, the software complexity was introduced to enable the instrument to operate efficiently under a wide variety of conditions with a minimum of operator intervention.

2.5. Laser metrology

During initial operation in 1986, the siderostat laser metrology system was not operational. However, the laser system is important for astrometry and should become operational in the summer of 1987. The basic laser interferometer used to measure changes in instrument geometry was described in the delay line section of this paper. Two such interferometers measure the position of the cat's eye retroreflectors. An additional 12 interferometers will be used to measure the position of the three siderostat mirrors.

The metrology system measures the motion of the pivot point of the siderostat by measuring the distance between four reference corner cubes in an invar plate, which is bonded to the concrete pedestal, and the surface of a zerodur sphere attached to the mirror as shown in Fig. 7. The sphere is made accurate to $\lambda/10$ and the center of the sphere is coincident with the mechanical pivot point to 20 μm . The interferometers have 5 nm resolution; the desired accuracy of the pivot point monitor is 100 nm for one-milliarcsec astrometry with a 20-m baseline. The measurements from these lasers will be used to correct for mechanical errors in the siderostat as well as thermal motion of the siderostat, as described below.

The basic model for the instrument is given by

$$\text{Fringe Pos} = \mathbf{S} \cdot \mathbf{B} + C, \quad (8)$$

\mathbf{S} is the unit vector to the star.

\mathbf{B} is the baseline vector.

C is the delay offset.

If the siderostats were perfect, the baseline vector would be the vector that joined the pivot points of the two siderostats. If the delay lines were commanded to move to their zero positions, the delay offset C would be the difference in the optical paths from the beamsplitter to the pivot points of the two siderostats. Motion of the siderostat pivot points affects both \mathbf{B} and C . Motion of the internal optics only affects C .

With our 12-m baseline on Mt. Wilson, the rms atmospheric fringe motion was 6 μm under conditions of good seeing. For stellar diameter measurements with the fringe tracker running, neither instrument drifts nor atmospheric motion is important. However, for astrometric measurements, the measured fringe position in Eq. (8) is made relative to the baseline vector and delay offset. Thus, it is necessary that both \mathbf{B} and C be constant over a period of time that is sufficiently long for the interferometer to be able to observe the fringe position of a number of stars.

The parameters \mathbf{B} and C can change for two reasons: imperfect siderostat bearings and thermal drift. Ideally, the siderostat pivots about a point on the surface of the mirror. In practice, the mirror translates as it rotates in a rather unpredictable way due to irregularities in the bearings and flexure of the mirror cell. The laser metrology system is designed to measure these imperfections. The result, in theory, is that baseline drifts will be limited to thermal drift of the top of the concrete pier to which the reference corner cubes in the laser system are attached. With rapid switching between stars, only baseline drift with a time scale faster than the

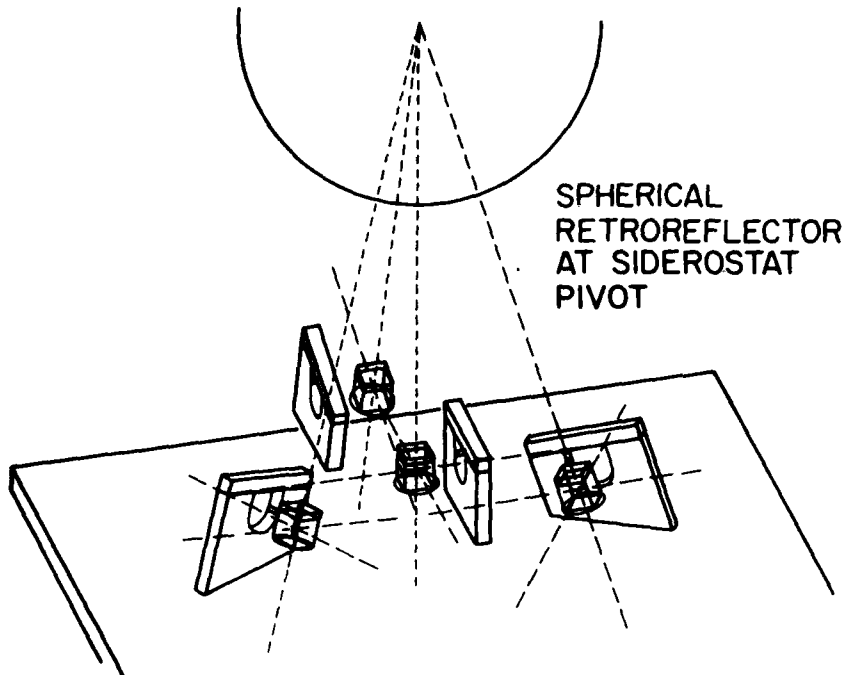


Fig. 7. Laser metrology system for baseline vector monitor

SIDEROSTAT WITH 4-LASER PLATE

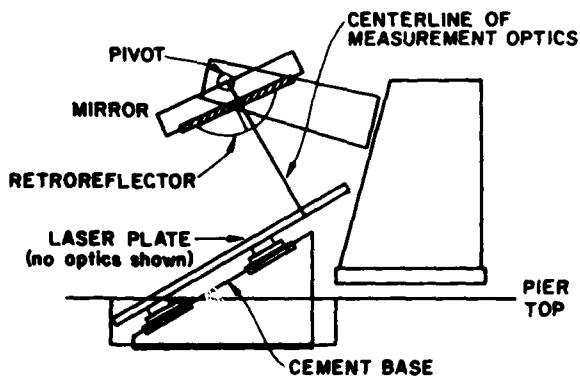


Fig. 8. Arrangement of siderostat and laser plate on Pier

switching cycle results in astrometric errors for large angle relative astrometry.

In order to monitor the position of the pivot point, a minimum of three interferometers is necessary. The fourth interferometer provides the redundancy necessary to solve for the position of the reference corner cubes. The interferometers measure the position of the center of the sphere. Certain parameters, such as the distance between the center of the sphere and the surface of the mirror must be derived from stellar data.

The mechanical accuracy of the instrument without the laser metrology system is approximately 10-15 μ m if the baseline was

calculated from the previous night's stellar data. The size of this error implies that searching for the fringe would take only a few hundred milliseconds, an insignificant amount of time compared to the 30 to 60 s needed for the siderostats to slew to a new star. The mechanical errors are roughly equivalent to the errors due to atmospheric turbulence, or to the errors in the primary mirror of a high quality large astronomical telescope. With the laser system we hope to improve this accuracy by two orders of magnitude.

While this higher mechanical accuracy is not necessary for stellar diameter measurements, it is crucial for ultra-high accuracy astrometry. This level of accuracy is also necessary for future space-based phase coherent long baseline interferometers.

2.6. Siderostat control

The siderostat control subsystem is in many ways similar to the computer controlled pointing system for a modern astronomical telescope. The siderostat itself is a two axis motorized gimballed mirror mount (Fig. 8), with the fixed axis tilted 75° from vertical towards the West. The siderostats use conventional precision worm and wheel gears and microstepped stepper motors. The control computer sets programmable pulse generators to control motor velocity. The average step size is 0.02° to provide smooth tracking, and the maximum slew rate is 1.8 per second. Typical backlash in the gear train is less than 1".

The control system performs several tasks. One is open loop or blind pointing, where a geometric model of the siderostat is used to point the siderostat and track the star. A second task is closed loop pointing, where the siderostat is moved to keep the high-speed PZT tilted mirrors in the center of their range. The third task is updating the parameters of the geometric model when a star is

Table 3. Siderostat model parameters

ϕ_F, θ_F	Angular orientation of feed beam (internal alignment)
Az, El (F)	Azimuth and elevation of fixed axis
θ_{axis}	Angle between fixed and movable axis
θ_{mirror}	Angle between movable axis and mirror normal
Z_F, Z_M	Zero point of motor position on the two axes

acquired. In addition, the siderostat control system controls the sequencing of observations during the night.

The geometry of the siderostat described earlier was that of an ideal siderostat. However, the stationary axis may not be exactly 15 degrees from horizontal; it may not be pointed due west, and the two axes may not be exactly perpendicular. Altogether, there are eight parameters in the geometric model of the siderostat. With values of these eight parameters, there is a closed-form relation between the angular positions of the motors and the pointing of the instrument. It is also possible to invert this problem in closed form. By pointing the siderostat at a number (> 4) of bright stars whose coordinates are known, and recording the positions of the motors when the stars are centered in the field of view of the interferometer, the eight parameters of the model can be determined in a least squares fashion. In our initial setup, we used the FK4 coordinates of a half dozen stars precessed to the night of observation.

Since the siderostats direct the starlight into the central beam-combining building, the alignment of the interferometer optics inside the building will affect the pointing of the siderostat. The internal alignment of the interferometer is represented by two of the eight parameters describing the siderostat. All of the parameters are listed in Table 3. No attempt was made to model errors in the precision worm and wheel gear or to model flexure. It is most likely that the residual errors are primarily in the gears. Residuals from a least-squares fit for the siderostat parameters are of order 5". Typical pointing errors for stars which are not used in the least-squares fit are approximately 7" to 10".

However, each new star that is observed provides some information on the eight siderostat parameters. Hence, rather than an off-line least-squares solution, a real time algorithm could be implemented to update the eight parameters every time the instrument locked onto a new star. In the Mark III, a Kalman filter is used to update the parameter vector. In operation, the initial values of the parameters at the beginning of the night are the parameters derived from the previous night's observations. These parameters are updated for every new star and, under normal conditions, the initial values would be essentially lost after approximately 6 stars. Thereafter, the parameter estimates would reflect thermal drift of the instrument during the night.

This complex siderostat model is used only for initial acquisitions. After the star tracker locks onto the star, the positions of the PZT tilt mirrors are sent to the siderostat control computer. The siderostat drive rates for the motors are then modified to keep the PZTs in the center of their range. Since the PZT tilt mirrors in effect represent realignment of the internal optics, the corrections to the sideral rate are generated by changing the parameters θ_F, ϕ_F .

The siderostat control computer also calculates the theoretical fringe position and velocity for the optical delay line. These values

are sent to the delay line control computer through a shared multiport memory every 2s. The theoretical fringe position is calculated from a baseline vector derived from the previous night's data. In the future, we plan to update the baseline vector with a Kalman filter in the same way the siderostat parameters are updated. On the first night of interferometric observations, the baseline vector was determined by conventional surveying techniques. The surveying error was approximately 1 mm, or about 20" of baseline tilt.

The last function of the siderostat control computer is the sequencing of observations. An abbreviated version of the FK4 catalog is kept on-line (In 1987, the FK5 catalog will be kept on-line). A menu driven program enables the operator to list and plot the stars visible at the present time and to easily define the stellar observation sequence. The siderostat control computer also communicates with the other two control computers to enable fully automatic operation once the observing sequence is programmed. The siderostat control computer signals the star tracker computer to initiate a star acquisition sequence. When the star tracker has locked onto a star it signals the fringe tracker computer to initiate a fringe acquisition sequence. When the allotted observing time for a star is over, the siderostat control computer signals the other two computers to disengage their servo systems. For additional information, the reader is referred to Kelly (1986).

3. Operational characteristics

The instrument was built and debugged over a 33 month period. Fringes were observed on the first night of operation, September 12, 1986. Over the following months, observational techniques were refined and automated. Figure 9 is a plot of the observations made on 1986, November 11. The vertical axis is the delay line position where fringes were observed. Each dot represents a 100-s observation. A total of 165 observations of 23 stars were made over a 10.5-h period. Stars over a declination range of 68° and an hour angle range of 8 h were observed. All these observations were of stars 3.0 magnitude or brighter.

The initial measurements in 1986 will be discussed in a series of separate papers. Wide-angle one-color astrometry shows night-to-night repeatability of about 0.04" (Mozurkewich et al., 1987), and the formal error for seven nights of data is 0.02" in declination. Significant improvements are anticipated when two-color analysis is applied and when the laser siderostat monitor is installed in the summer of 1987. Preliminary measurements on the atmospheric limitations of two color absolute astrometric measurements indicate that single observations of ~ 100 s should yield accuracies of about 0.01", a factor of 5 improvement over one-color observations (Colavity et al., 1987). Two-color observations should approach 0.003" for a single night's observation. Last of all, we have made preliminary stellar diameter measurements of β Gem and α CMi. Assuming a uniform disk, we measure 6.15 ± 0.25 mas for α CMi and 8.70 ± 0.15 mas for β Gem. The uniform disk diameter for α CMi is not in agreement with prior measurements (Hanbury Brown et al., 1974) in part due to the difference in observation wavelength and uniform disk assumption. A much more careful discussion of accurate stellar diameter measurements is given elsewhere (Shao et al., 1988).

The instrument was never operated near the limiting magnitude of the fringe tracker because the temporary star tracker we were using could not track stars fainter than 3 mag. The tracker using the photon camera should be capable of operation on faint

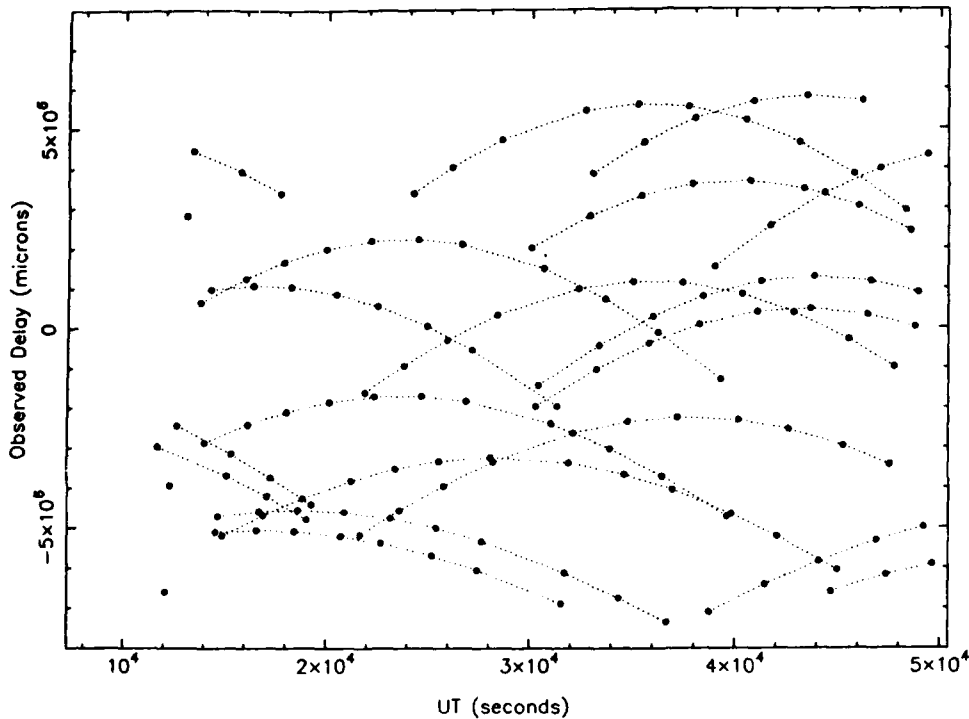


Fig. 9. Position of delay line where fringes were observed. 165 observations of 23 stars

sources, to 12 mag under good seeing conditions when only mechanical errors need to be tracked. When the new star tracker is installed in the spring of 1987, the limiting magnitude will be set by the fringe detection system. We plan to operate the interferometer in two distinct modes that have two very different magnitude limits. The two modes represent two types of interferometers. One is a closed loop phased interferometer. The second is an open loop coherent interferometer or absolute interferometer. We plan to test this second mode of operation in the next two years.

3.1. Phase-coherent interferometry

The Mark III was designed to be an active phased interferometer. In this mode of operation, the fringe tracker compensates for all optical path fluctuations, including atmospheric turbulence to $\sim \lambda/6$ rms. Fringe phase measurements in two colors are used for astrometric purposes, while light from a bandpass filter, $< 400 \text{ \AA}$, is used for stellar diameter measurements. It is also possible to measure the diameter of a star at emission or absorption lines. For diameter measurements in narrow spectral lines, we make use of the phase coherent property of an active interferometer. For narrow spectral lines, the photon flux in the line might be 10^{-3} of the total flux and the number of photons per atmospheric coherence time may be as low as 10^{-2} . However, since the active optics system is phase coherent, the coherent integration time is not limited to the atmospheric coherence time. By choosing a longer coherent integration time, > 1 s, a fringe visibility measurement can be made in 10^4 s with a signal-to-noise ratio of 100.

For astrometry, the fringe phase and the position of the optical delay line is recorded when the fringe tracker is locked on the

central fringe. In this case, the astrometric error due to photon noise is negligible and the major errors are instrumental. A detailed discussion of one- and two-color astrometry will be presented in separate papers (Colavita et al., 1987; Mozurkewich et al., 1988). However, the astrometric capability of the instrument affects all other modes of operation of the instrument.

With the known coordinates of FK 5 stars it is possible to derive the baseline vector and delay offset by measuring the fringe position of four stars. This derived baseline is as accurate as the coordinates of the FK 5 stars used. An accurate baseline vector in turn enables the instrument to find the fringe faster and to increase the number of observations from several per night to several hundred per night. This astrometric capability is the key to operation of the instrument as an absolute interferometer, described next.

3.2. Absolute interferometer

Within the next year we plan to install the software for real time baseline calibration. In this mode, the interferometer will rapidly switch between 4–6 FK 5 stars to calibrate the baseline, and then point blind at a faint astronomical object for about 10^3 s. This cycle will be repeated to yield the desired integration time on the faint object. Three types of measurements are planned, two of them in the near future. There are significant advantages to phase coherent operation and operation in the absolute mode is reserved for objects too faint for the fringe tracker, 9 mag for 10 cm apertures. All three types of measurements planned for the absolute interferometer are photon starved measurements. Under these conditions, direct phase measurements are not possible and the

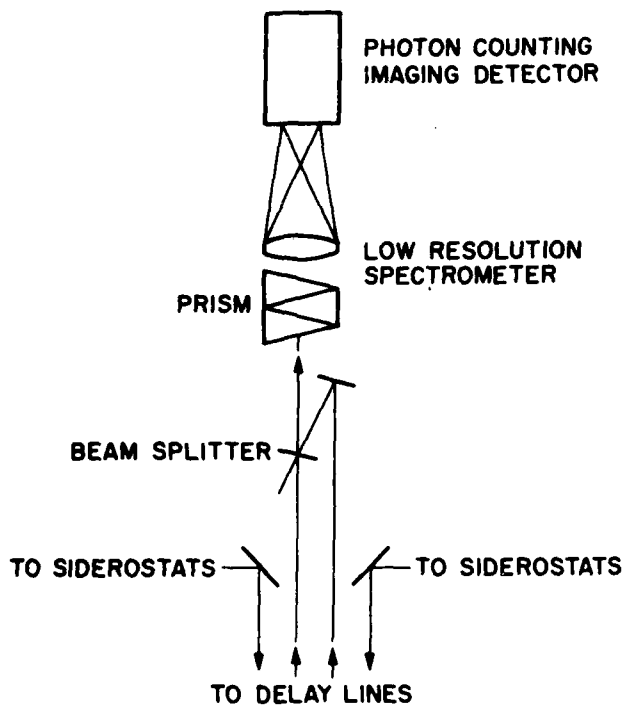


Fig. 10. Dispersed fringe detector schematic

only quantities that can be measured are amplitude, group delay, and closure phase. Photon starved conditions occur when the average number of photons per r_0 aperture, per τ_0 integration time, is less than 1 in the coherent optical bandpass.

In open loop operation, a 12-m interferometer will exhibit rms phase fluctuations of approximately 20λ at $0.6\mu\text{m}$ for 1" seeing. The fringe detector must be able to accommodate this lack of temporal coherence. On the other hand, to maximize sensitivity, light from all wavelengths should be used for interferometric measurements. The basic fringe detector (Fig. 10) consists of a prism spectrometer with an imaging photon counting detector. The required resolution of the spectrometer is of the order of

$$\Delta\lambda \approx \lambda \left(\frac{r_0}{L} \right)^{5/6} \quad (9)$$

where λ is the wavelength of observation, L the length of the baseline, and $r_0 \propto \lambda^{6/5}$ is equal to about 10 cm at $0.6\mu\text{m}$ for 1" seeing. Conservatively, 50 Å channels are assumed in the calculations below. In the following sections we briefly describe the signal processing of the output of the detector for the three different types of photon starved measurements.

3.2.1. Photon-starved amplitude measurements

The estimator for fringe amplitude must be modified to take into account a bias that is important at low photon rates. An unbiased estimator for visibility squared is given by

$$V^2 = \frac{\pi^2}{2} \left[\frac{\langle (A-C)^2 + (B-D)^2 - N \rangle}{\langle N - \text{Dark} \rangle^2} \right] \quad (10)$$

where $N = A + B + C + D = \text{total photon flux}$, $\text{Dark} = \text{dark count}$ and $\langle \rangle$ denotes time average.

The signal-to-noise ratio of the above visibility estimator has been extensively studied both for amplitude interferometry and speckle interferometry. There are two regions of interest, depending on photon rate. The dependence of integration time needed to achieve a given signal-to-noise ratio, given a photon flux N per r_0 aperture, per τ_0 integration time, per spectral channel is given by

$$\begin{aligned} \text{Integration time} &\propto N^{-1}, \quad N > 1, \quad N > \text{Dark} \\ &\propto N^{-2}, \quad 1 > N > \text{Dark} \end{aligned} \quad (11)$$

For stellar diameter measurements, the numerator and denominator of the expression in Eq. (10) must be evaluated every 10 ms for each spectral channel, typically 60 channels of 50 Å bandwidth for a 12-m baseline. If collecting apertures greater than r_0 (10 cm) are used, there must be a spectrometer for each r_0 subaperture. In photon starved operation there is no hard magnitude limit as there is in active phase coherent operation. As a practical limit we require a signal-to-noise ratio of 30 in 10^4 s of integration. Assuming an unresolved star, the required photon flux is $1.6 \cdot 10^{-2}$ photons in each of 60 spectral channels, per r_0 aperture per 10 ms. This corresponds to a magnitude limit of 14.3 for 10-cm apertures. With 1-m apertures, the limiting magnitude is about 16.8 (see Appendix). Accurate visibility measurements will require much higher signal-to-noise ratios and the magnitude limit will degrade. The optical efficiency of the spectrometer was assumed to be 100% and the quantum efficiency of the imaging photon counter was assumed to be 10%. For these reasons, these estimates should be considered optimistic.

3.2.2. Photon-starved group delay astrometry

The signal from the spectrometer can be processed in a different way to yield astrometric information at faint magnitudes. When the optical path difference in the two arms of the interferometer is different by many wavelengths, say $3\mu\text{m}$, there will be constructive interference at $\lambda = 0.5\mu\text{m}$ and $0.6\mu\text{m}$, and destructive interference in between. More precisely, the spectrometer output will exhibit a fringe pattern due to the interference of light from the two siderostats as given by

$$I(\nu) = I_0(\nu) (1 + \sin 2\pi\nu\tau) \quad (12)$$

where $I_0(\nu)$ is the spectrum of the star, ν is optical frequency ($1/\lambda$) and τ is the optical path difference in the two arms of the interferometer, i.e., the group delay. Equation (12) has a sine rather than a cosine because the Mark III uses a dielectric beamsplitter to combine the beams. The Fourier transform of the "fringed" spectrum $I(\nu)$ will have a delta function at τ . At this delay, the Fourier transform has both an amplitude and phase. In the photon starved mode, where

$$\int I(\nu) d\nu < 1 \text{ photon}/r_0^2/10 \text{ ms} \quad (13)$$

the phase is not measurable.

The basic signal processing algorithm is to average the power spectrum of $I(\nu)$. As in the previous section, each r_0 subaperture must be separately processed if the collecting apertures are large. Since τ changes due to turbulence, a time average of the power spectrum is a gaussian distribution of delta functions. For a 12-m baseline, the standard deviation of this gaussian is $\sim 12\mu\text{m}$ for 1" seeing. A SNR of 30 in this case means that the peak in the gaussian is approximately 30 times the rms fluctuations in the rest of the power spectrum. For 10-cm apertures, the magnitude limit is approximately 14.3 mag. For 1-m apertures, the corresponding limit is 16.8 (see Appendix).

3.2.3. Photon-starved closure phase

Closure phase measurements were first made with radio interferometers (Jennison, 1958), and subsequently suggested for optical interferometers (Rogstad, 1968). Recently, closure phase measurements were made at visible wavelengths by masking the aperture of a large telescope (Baldwin, 1986; Readhead, 1988) at photon rich levels. In closure phase measurements, three interferometers, whose baselines form a closed triangle, measure three complex visibilities corrupted by turbulence. However, the closure phase, the sum of the phases of the three complex visibilities, is independent of the atmosphere. In photon starved measurements, raw phases cannot be measured. Instead, the product of the complex visibilities is averaged, i.e.,

$$\text{triple product} = \langle A_1 e^{i\phi_1} A_2 e^{i\phi_2} A_3 e^{i\phi_3} \rangle, \quad (14)$$

where $A_1 e^{i\phi_1}$ is the complex visibility from interferometer 1. The importance of averaging the complex visibilities comes from the fact that the product of complex visibilities is not biased in the photon starved region. The closure phase is simply the imaginary part of the log of the triple product (see Appendix). The triple product was first used in high resolution optical imaging for reconstruction of speckle images (Weigelt, 1977), a technique called speckle masking. This technique extends the sensitivity of closure phase measurements more than an order of magnitude beyond conventional photon rich measurements.

For long baseline interferometers, the triple product must be calculated every 10 ms, for each spectral channel, and each r_0 aperture. The signal-to-noise ratio (SNR) of the triple product is qualitatively different from the SNR for amplitude measurements. At high photon fluxes, $N \gg 1$, the SNR of all these quantities varies as \sqrt{N} . At low photon fluxes, $N < 1$, the SNR for amplitude measurements varies as N , and that of the triple product varies as $N^{3/2}$ (see Appendix). Again, assuming an SNR of 30 in 10^4 s ($\Delta\phi$ measured to $\lambda/180$), the magnitude limit with 10-cm apertures is approximately 12.5 mag, or a photon flux of 0.08 photons per r_0 , per 10 ms, per 50 Å bandwidth. The limiting magnitude for 1-m apertures is 14.2.

Although three siderostats will be in operation in 1987, closure phase measurements are not planned for the immediate future. In order to operate three interferometers simultaneously the second delay line must be converted to high precision operation. Operation as an absolute interferometer will then enable closure phase measurements to be made with a one to two order-of-magnitude increase in sensitivity over active phase coherent operation.

4. Conclusion

In the past seventy years a number of stellar interferometers have been proposed and built. Starting with Michelson, the instruments have gotten progressively more complex and sophisticated (Koechlin et al., 1985; Labeyrie et al., 1986; Davis et al., 1986). The Mark III incorporates many of the ideas proven by these previous instruments. The major differences between this interferometer and others reside primarily in its operational characteristics - it is fully automated, it is easy to operate, and it is mechanically accurate and thermally stable. It is also capable of making literally hundreds of observations in one night; both astrometric and stellar diameter measurements are possible. Last of all, this instrument has the potential to operate as an absolute interferometer which, from an astronomical point of view, holds tremendous promise for observation of faint objects.

To fully exploit the possibilities of absolute interferometry, and to construct images of faint extragalactic objects at milliarcsec resolution, even more complex interferometers with large, multiple apertures will be needed. During the next several years the Mark III should demonstrate much of the necessary technology, as well as produce some of the scientific results that would motivate the construction of a large optical array.

Acknowledgements. The authors wish to acknowledge the important contributions of P. Cheimets, J. Pohlman, and C. Papa in the design and construction of the precise mechanical components of the system as well as the staff of Mt. Wilson Observatory for their cooperation and aid during the construction of the instrument. This project was made possible with support from the following grants and contracts: N 00014-84-C-2082, N 00014-84-C-2137, N 00014-85-C-2212, N 00014-86-C-2105, N 00014-86-C-2114 from the Naval Research Laboratory; from the Smithsonian Institution directly and through its Scholarly Studies Program; AST 79-19553 from the National Science Foundation; NAS-2-50 and NSG-7176 from NASA; ONR N 00014-80-C-0348 from the Office of Naval Research.

Appendix: photon-starved interferometry

The photon-starved signal-to-noise ratio for the three interferometric quantities: amplitude, group delay, and closure phase are discussed in this Appendix. We present limiting magnitudes for these quantities extrapolated from our experience with the Mark III interferometer. Recently, there has been considerable interest in the use of light scattered from the ionosphere from a pulsed laser in order to provide a probe of atmospheric turbulence to operate an active-optics system (Foy and Labeyrie, 1986). The application of this technique is not considered in our calculations.

Estimates of amplitude, group delay, and closure phase each have slightly different magnitude limits. Qualitatively, different effects degrade the sensitivity for the different quantities. In all cases, we assume that the fringe detector is a dispersive spectrometer followed by an imaging photon-counting detector. We also assume that the resolution of the spectrometer is a few times greater than what is needed to maintain high fringe contrast in the presence of the optical path fluctuations caused by atmospheric turbulence. Magnitude limits are calculated assuming an unresolved star, a 12-m baseline, 10-cm collecting apertures, a 10 ms coherent integration time, a 60-channel, 50 Å resolution spectrometer, unit fringe visibility, a total integration time of 10^4 s, and a final signal-to-noise ratio of 30. The detector dark count is neglected, and a total system efficiency of 0.1 is assumed. We ignore the reduction in fringe visibility and hence signal-to-noise ratio due to the use of coherent apertures of 10 cm and integration times of 10 ms. In practice, the seeing would have to be somewhat better than 1" for these magnitude limits to be achieved. Scaling formulae are given for the case of different seeing conditions.

At high photon fluxes, when the number of photons per r_0 aperture, per atmospheric coherence time τ_0 , per spectral channel $\Delta\lambda$, is much greater than one, the signal-to-noise ratio is proportional to the square root of the photon flux for estimates of all three interferometric quantities. We define the quantities N and M as

$$N = \text{No. of detected photons per frame, i.e., per } r_0, \tau_0, \Delta\lambda,$$

$$M = \text{No. of frames} = \left(\frac{D}{r_0}\right)^2 \left(\frac{T}{\tau_0}\right) \left(\frac{BW}{\Delta\lambda}\right),$$

where D = diameter of telescope, T = total integration time, and BW = total optical bandwidth of the spectrometer (assumed 0.4 to 0.7 μm). The terms photon-rich and photon-starved apply to the cases $N > 1$ and $N < 1$, respectively.

The signal-to-noise ratio for fringe amplitude measurements has been extensively studied for many types of interferometers. It is usually more convenient to consider estimates of V^2 rather than of V . The signal-to-noise ratio for estimates of V^2 can be written (Tango and Twiss, 1980)

$$SNR(V^2) = \frac{1}{4} M^{1/2} N V^2 \left[1 + \frac{1}{2} N V^2 \right]^{-1/2} \quad (\text{A } 1)$$

For the case of a fringe-scanning interferometer with 4 bins per scan, N is replaced by $(8/\pi^2)N$. The qualitative feature of this expression is that at low photon fluxes, $N < 1$, the signal-to-noise ratio is proportional to N , rather than to $N^{1/2}$. Thus, if a star is dimmer by a factor of 10, the number of frames M must increase by a factor of 100 to give the same signal-to-noise ratio.

The noise behavior of the group-delay estimate is similar to the V^2 estimate. The "fringed" spectrum as detected by the spectrometer is

$$I(v) = I_0(v) (1 + \sin 2\pi v \tau'), \quad (\text{A } 2)$$

where $I_0(v)$ is the spectrum of the star, v is optical frequency, and τ' is the group delay. The group delay changes due to atmospheric turbulence. Over long time intervals, τ' is a gaussian-distributed random variable with mean τ_1 , determined by the position of the star and optical delay line, and variance $\sigma_{\tau'}^2$, which depends on the seeing and baseline length. The variance is given by

$$\sigma_{\tau'}^2 = 6.88 (\lambda/2\pi)^2 (L/r_0)^{5/3}, \quad (\text{A } 3)$$

where L is the baseline length and r_0 is the atmospheric coherence diameter.

Each coherence time τ_0 , the power spectrum, $P(\tau)$, of $I(v)$ is calculated. The power spectrum is then averaged for the length of the observation. There are three important features: a peak at the origin attributable to the Fourier transform of $I_0(v)$, a uniform bias due to photon noise, and a gaussian distribution at the mean group delay τ_1 due to atmospheric turbulence. The averaged power spectrum is given by

$$\langle P(\tau) \rangle = \langle | \int e^{2\pi i v \tau} I_0(v) (1 + \sin 2\pi v \tau') dv |^2 \rangle, \quad (\text{A } 4)$$

where $\langle \rangle$ represents an ensemble average over both group delay τ' and photon statistics.

A better estimator is the unbiased, normalized power spectrum $Q(\tau)$, given by

$$Q(\tau) = \frac{\langle P(\tau) - \int I(v) dv \rangle}{\langle \int I(v) dv \rangle^2}, \quad (\text{A } 5)$$

where $N_s = \int I(v) dv$ is the total photon flux in a 10 ms interval. Comparison of this expression with the estimator (11) shows that (A5) is just the V^2 estimator evaluated at a particular group delay. Thus, the performance of the group delay estimator can be calculated using (A1).

Given a spectrometer with a bandwidth of 0.4 μm to 0.7 μm , the delay resolution is $\Delta x = (1/0.4 - 1/0.7)^{-1} \sim 1 \mu\text{m}$. Since the group delay fluctuates with a standard deviation of $\sigma_{\tau'}$, the gaussian distribution of group delay in $Q(\tau)$ will be spread over approximately $\sigma_{\tau'}/\Delta x$ bins, while the amplitude of the gaussian will be reduced by approximately $\sigma_{\tau'}/\Delta x$. Photon-starved statistics apply for $(1/2) N_s V^2 < \sigma_{\tau'}/\Delta x$, and using (A1), the signal-to-noise

ratio for an estimate of the amplitude of the gaussian using a matched filter is given by

$$SNR(Q(\tau)) = \frac{N_s V^2 M^{1/2}}{7.5} \sqrt{\frac{\Delta x}{\sigma_{\tau'}}}, \quad (\text{A } 6)$$

where N_s is the total photon flux in the spectrum. In (A6) sampling losses are neglected, and it is assumed that $\sigma_{\tau'} \gg \Delta x$. Using (9) and (A3) to write (A6) in terms of N , rather than N_s , yields a signal-to-noise ratio for group delay estimates which is nearly identical to the signal-to-noise ratio of a conventional amplitude estimate.

For the case of group-delay, an estimate of the centroid of the group-delay distribution is desired. The standard deviation of such an estimate can be written

$$\sigma_p = \sqrt{2\sigma_{\tau'}} / SNR, \quad (\text{A } 7)$$

where the SNR is given by (A6). A Monte Carlo simulation was performed which verified the above analytically derived expressions.

Under photon-starved conditions, the measurement of closure phase is qualitatively different from the measurement of amplitude. The definition of the triple product, Eq. (14), is repeated below:

$$\text{triple product} = \langle A_1 e^{i\phi_1} A_2 e^{i\phi_2} A_3 e^{i\phi_3} \rangle, \quad (\text{A } 8)$$

In photon-counting measurements, if zero photons are detected in any one of the three interferometers, the triple product is zero. For a frame to contain some information on the closure phase, at least one photon must be detected in all three interferometers. The Poisson probability function is given by

$$P(m) = \frac{N^m e^{-N}}{m!}, \quad (\text{A } 9)$$

where $P(m)$ is the probability of detecting m photons given an average arrival rate of N . For $N \ll 1$ the probability of detecting one photon is N . Thus, the probability of detecting one photon in all three interferometers is N^3 , so that the variance for estimates of closure phase should be proportional to N^{-3} under photon starved conditions.

More precisely, the variance of the closure phase calculated via the triple product can be written

$$\sigma_{\phi}^2 = 3 \left(\frac{2}{N^{1/2}} \right) + 6 \left(\frac{2}{N^{1/2}} \right)^2 + 4 \left(\frac{2}{N^{1/2}} \right)^3 \quad (\text{A } 10)$$

for a signal-to-noise ratio $SNR = 1/\sigma_{\phi}$. In this expression N is the average number of detected photons in each interferometer. Equal visibilities V have been assumed for each of the three interferometers. Thus, at high photon fluxes, the variance is three times the variance in a photon-rich phase measurement. At low photon fluxes, the variance is proportional to N^{-3} , as given by the last term of (A10). For this term, V is the geometric mean of the visibilities in the three interferometers. A Monte Carlo simulation for closure phase measurements was also conducted, which verified the above expression.

The integration time needed to achieve a signal-to-noise ratio of 30 versus photon flux N is given in Fig. 11 for measurements of visibility squared and group delay, and closure phase. For astronomical measurements, a photon flux corresponding to an SNR of 30 on an unresolved star allows a diameter measurement of 4% on a partially-resolved source. An SNR of 30 for group delay corresponds to an astrometric measurement of 0.6 μm in

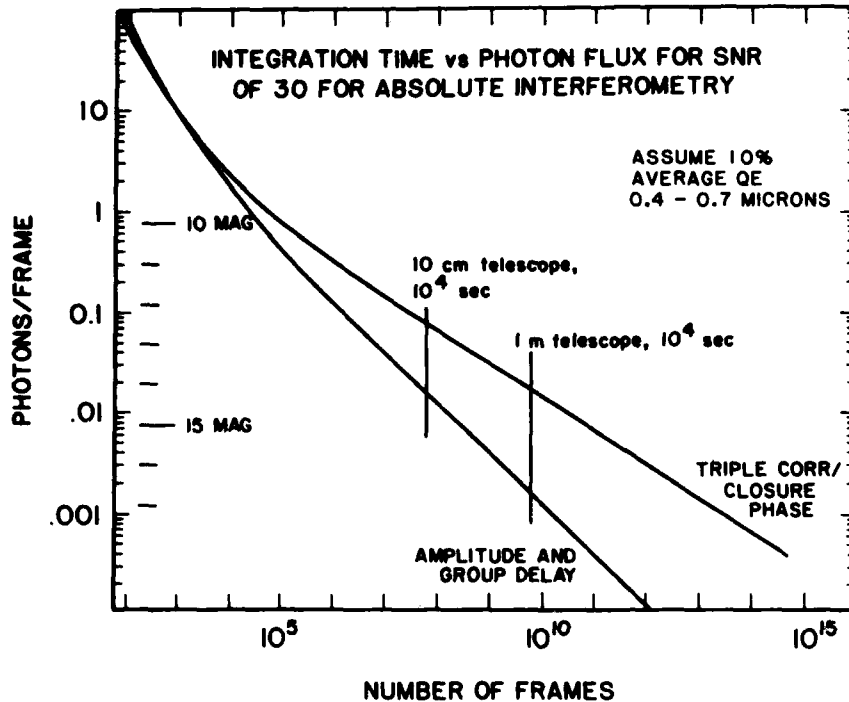


Fig. 11. Integration time vs. magnitude for photon-starved measurements

delay, or 0.01 in angle. An SNR of 30 for the triple product corresponds to an error of $\lambda/180$ in closure phase. The limiting magnitudes for a single- r_0 system are approximately 14.3 and 12.5 for visibility/group delay and closure phase. With 1-m apertures, the limiting magnitudes are approximately 16.8 and 14.2, respectively.

If r_0 and τ_0 are different from the nominal values assumed, the magnitude limits will change. In general, an instrument will have a fixed collecting aperture. Thus, if r_0 increases, the number of photons, N , per r_0 increases, but the number of frames, M , decreases. Similarly, given a fixed 10^4 s for a measurement, an increase in r_0 will also increase N and decrease M . If the signal-to-noise ratio were dependent on N and M evenly, the final SNR would be independent of seeing. This is the case for photon-rich measurements where the SNR is proportional to \sqrt{NM} .

For photon-starved measurements, this is not the case. The signal-to-noise ratio for amplitude and delay measurements follow the scaling relation $NM^{1/2}$, while the SNR for closure phase follows the relation $N^{3/2}M^{1/2}$. Two additional facts should be considered. As r_0 improves, the rms path length fluctuation between the apertures decreases proportionally. Hence, the number of required spectral channels that must be separately analyzed decreases according to (9). In addition, since the temporal fluctuations of phase are usually modeled by assuming frozen turbulence translating past the instrument at a constant wind speed, τ_0 should increase with r_0 . Thus, the scaling of N and M with r_0 is approximately given by

$$N \propto r_0^4, \quad (\text{A11})$$

$$M \propto r_0^{-4}. \quad (\text{A12})$$

The scaling of the magnitude limits for photon-starved measurements with seeing is then given by

$$\text{Amplitude/delay sensitivity} \propto r_0^2, \quad (\text{A13})$$

$$\text{Phase closure sensitivity} \propto r_0^{8/3}. \quad (\text{A14})$$

These results should be compared to the case of a wideband phase tracking system. In this case, only N , not M is important, and since the fringe is tracked, there is no need for the spectrometer. Thus, the sensitivity scales with seeing as r_0^3 .

References

- Baldwin, J.E., Haniff, C.A., Mackay, C.D., Werner, P.J.: 1986, *Nature* **320**, 595
 Connes, P.: 1975, *Appl. Opt.* **14**, 2067
 Clark, L.D., Shao, M., Colavita, M.M.: 1986, *Proc. SPIE*, **627**, 838
 Clark, L.D.: 1986, M.S. Thesis, Dept. of E.E.C.S., M.I.T., Cambridge, MA
 Colavita, M.M., Shao, M., Staelin, D.H.: 1987, *Appl. Opt.* **26**, 4106 and 4113
 Davis, J., Tango, W.J.: 1986, *Nature* **323**, 234
 Foy, R., Labeyrie, A.: 1986, *Astron. Astrophys.* **152**, L29
 Hanbury Brown, R., Davis, J., Allen, L.R.: 1974, *Monthly Notices Roy. Astron. Soc.* **167**, 121
 Holm, W.H.: 1986, M.S. Thesis, Dept. of E.E.C.S., M.I.T., Cambridge, MA
 Jennison, R.C.: 1958, *Monthly Notices Roy. Astron. Soc.* **118**, 276

- Kelly, M.J.: 1986, M.S. Thesis, Dept. of E.E.C.S., M.I.T., Cambridge, MA
- Koechlin, L., Rabbia, Y.: 1985, *Astron. Astrophys.* **153**, 91
- Labeyrie, A., Schumacher, G., Dugué, M., Thom, C., Bourlon, P., Foy, F., Bonneau, D., Foy, R.: 1986, *Astron. Astrophys.* **162**, 359
- Mozurkewich, D., Hutter, D.J., Johnston, K.J., Simon, R.S., Shao, M., Colavita, M.M., Staelin, D.H., Hines, B.E., Hershey, J.L., Hughes, J.A., Kaplan, G.H.: 1988, *Astrophys. J.* (in press)
- Papaliolios, C., Nisenson, P., Ebstein, S.: 1985, *Appl. Opt.* **24**, 287
- Readhead, A.C.S., Nakajima, T.S., Pearson, T.J., Neugebauer, G., Oke, J.B., Sargent, W.L.W.: 1988, *Astron. J.* (in press)
- Rogstad, D.H.: 1968, *Appl. Opt.* **7**, 585
- Shao, M., Staelin, D.H.: 1977, *J. Opt. Soc. Am.* **67**, 81
- Shao, M., Staelin, D.H.: 1980, *Appl. Opt.* **19**, 1519
- Shao, M., Colavita, M.M., Staelin, D.H., Johnston, K.J., Simon, R.S., Hughes, J.A., Hershey, J.L.: 1987, *Astron. J.* **93**, 1280
- Shao, M., Colavita, M.M., Hines, B.E., Staelin, D.H., Hutter, D.J., Johnston, K.J., Mozurkewich, D., Simon, R.S., Hershey, J.L., Hughes, J.A., Kaplan, G.H.: 1988, *Astrophys. J.* **327**, 358
- Tango, W.J., Twiss, R.Q.: 1980, in *Progr. Optics*, XVII, ed. E. Wolf, North-Holland, Amsterdam, p. 239
- Weigelt, G.P.: 1977, *Opt. Comm.* **21**, 55

INITIAL STELLAR DIAMETER MEASUREMENTS WITH THE MARK III INTERFEROMETER

M. SHAO AND M. M. COLAVITA
Smithsonian Astrophysical Observatory

B. E. HINES AND D. H. STAELIN
Massachusetts Institute of Technology

D. J. HUTTER, K. J. JOHNSTON, D. MOZURKEWICH, AND R. S. SIMON
Naval Research Laboratory, E. O. Hulburt Center for Space Research

AND

J. L. HERSHEY, J. A. HUGHES, AND G. H. KAPLAN
U.S. Naval Observatory

Received 1987 June 12; accepted 1987 October 1

ABSTRACT

We report initial stellar diameter measurements made with the Mark III stellar interferometer. The visibility measurements showed fluctuations of 1%–5% for a 10 s integration consistent with photon statistics as the predominant source of noise. Measurements of the unresolved star β Tau were used to calibrate the instrumental and atmospheric biases which reduce the measured visibility. We report angular diameters, at 706 nm, of 6.15 ± 0.25 mas, 8.70 ± 0.15 mas, 5.0 ± 0.5 mas, and 7.2 ± 0.4 mas rms for the stars α CMi, β Gem, α Per, and α UMa, respectively. These angular diameters were calculated, assuming a uniform disk, from the visibility measurements, the wavelength of observation, and the projected interferometer baseline. The angular diameters corrected for limb darkening are also presented. In the next observing season, the instrument should be able to make very precise diameter measurements on a large number of stars brighter than 7 mag.

Subject headings: instruments — interferometry — stars: diameters

I. INTRODUCTION

The Mark III interferometer is a joint project among the Smithsonian Astrophysical Observatory, the Massachusetts Institute of Technology, the Naval Research Laboratory, and the U.S. Naval Observatory. The instrument is located on Mount Wilson, California. First fringes were observed in 1986 September with a 12 m baseline.

Long-baseline optical stellar interferometers have traditionally been used to measure the diameter of stars. The Mark III interferometer (Shao *et al.* 1988), unlike other operational stellar interferometers (Labeyrrie 1975; Davis and Tango 1986), was designed principally for fundamental astrometry (Mozurkewich *et al.* 1987). Consequently, the instrument was designed with such characteristics as extreme thermal stability and submicron mechanical accuracy and makes extensive use of laser metrology. These features are not usually necessary for stellar diameter measurements. In addition, the instrument was optimized for high astrometric sensitivity through the use of very wide optical bandpasses, at the expense of some accuracy in the measurement of visibilities. It was subsequently modified to enable accurate visibility measurements to be made simultaneously with astrometric measurements, and a set of preliminary stellar diameter measurements were made in 1986 November. The next section describes the hardware used for making these initial visibility measurements, and the third section describes the observation and analysis procedure. The last section summarizes these initial measurements of α CMi, β Gem, α Per, and α UMa.

II. THE MARK III INTERFEROMETER

The instrument is an active-fringe-tracking long-baseline optical interferometer. Figure 1 shows a schematic of the

instrument. A star tracker, or autoguider, keeps the interfering wavefronts parallel to a fraction of an arcsec. The vacuum delay lines are monitored with laser interferometers with 5 nm resolution and can be set with 10 nm accuracy. An active fringe-phase-tracking servo-system keeps the optical paths in the two arms equal to a fraction of a wavelength of light in the presence of mechanical error, thermal drift, and atmospheric turbulence. Presently, light from one side of the beamsplitter is used for fringe tracking and light from the other side is used for visibility measurements through a narrow bandpass filter. In 1986, the magnitude limit of the instrument was set by an interim star tracker rather than by the fringe tracker. In 1987, an improved star-tracking system (Shao *et al.* 1988) will enable visibility measurements of $V = 7$ objects.

The fringe-detection scheme is based on a path-length modulation technique that was also used on two previous long-baseline stellar interferometers on Mount Wilson. A mirror on a piezoelectric stack (PZT) is moved in a 500 Hz triangle-wave pattern with a one-wavelength p - p motion. During each 1 ms sweep of the PZT, the number of detected photons in four equally spaced time bins is recorded, as shown in Figure 2. Successive 1 ms scans are co-added to yield the desired coherent integration time. These quantities— A , B , C , and D —are used to estimate the visibility. The amplitude of the path-length modulation is monitored by a laser interferometer and is controlled by a low-bandwidth servo with a precision of $\sim 0.1\%$ to reduce the systematic errors that arise when the modulation amplitude is different from the wavelength of observation. In order to minimize the systematic errors in the visibility measurements attributable to atmospheric turbulence, the amplitude measurements were made with an effective aperture of 2.5 cm, an optical bandwidth of 10 nm, and a

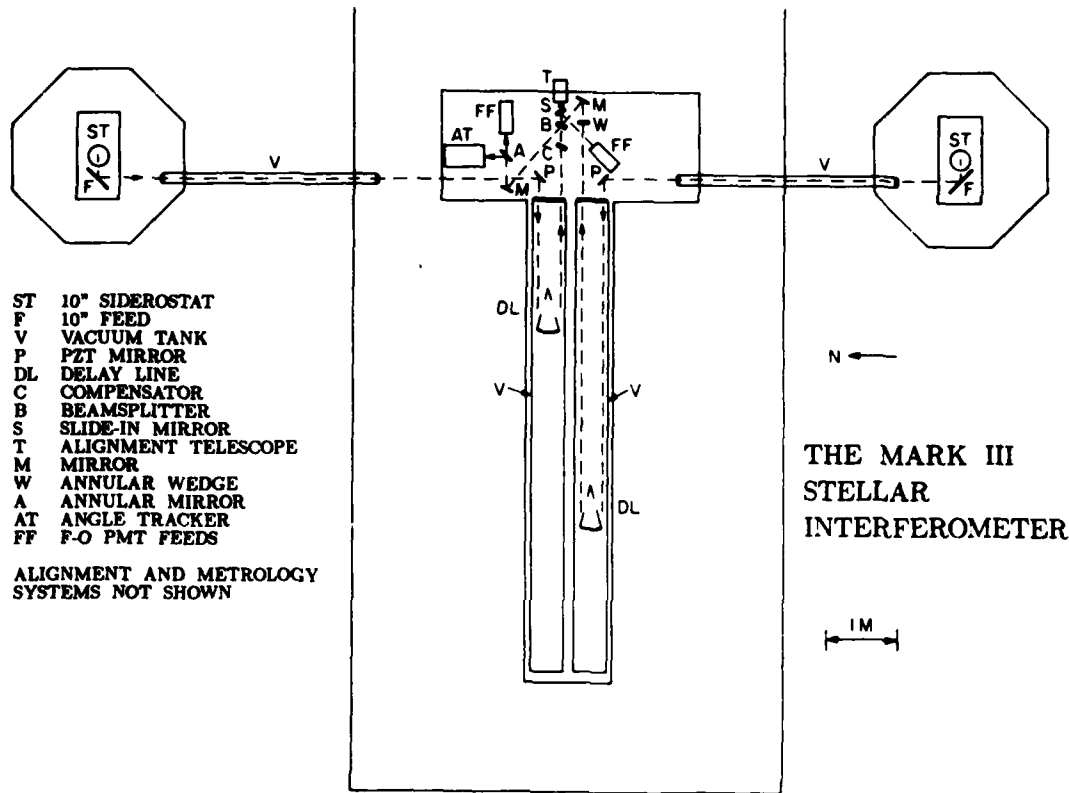


FIG. 1.—Schematic diagram of the Mark III stellar interferometer

coherent integration time of 4 ms. For a complete description of the instrument, see Shao *et al.* (1988).

The detectors used for the fringe measurements are GaAs PMTs cooled to -30°C . The dark count at this temperature is approximately 150 hz. The PMTs are fed with $200\ \mu\text{m}$ optical fibers and are sensitive to sky background in a 160° diameter field. Thus, to make accurate measurements of visibility, the

detector dark count and the sky background must be accurately measured. The measurement of these quantities was made part of the automated observing sequence.

III. OBSERVATIONS AND ANALYSIS

The measurements presented here were made on 1986 November 21. The stars to be observed, all FK4 stars, were programmed for observation at the beginning of the night. The control computers then directed the interferometer to make observations in the preprogrammed sequence. The program specified which stars were to be observed, in what order, and how much time was to be spent on each star. Data were recorded whenever the fringe tracker was locked on a fringe. These data, recorded at a 4 ms rate, included the time, the delay-line position, and the quantities *A*, *B*, *C*, and *D* for the amplitude and astrometric channels. After each stellar observation, while the siderostats were slewing to the next star, a 5 s measurement of dark count and sky background was also recorded. Amplitude measurements were made using a narrow-bandpass filter at 706 nm; some preliminary measurements at 604 nm were corrupted by scattered laser light and are not included here.

Using the bin counts *A*, *B*, *C*, and *D*, the square of the fringe visibility is calculated as

$$V^2 = \frac{\pi^2 \langle (A - C)^2 + (B - D)^2 - N \rangle}{2 \langle N - \overline{Dr} \rangle^2} \tag{1}$$

where $N = A + B + C + D$, \overline{Dr} is the average dark count per 4 ms, and angle brackets denote time average. This estimator

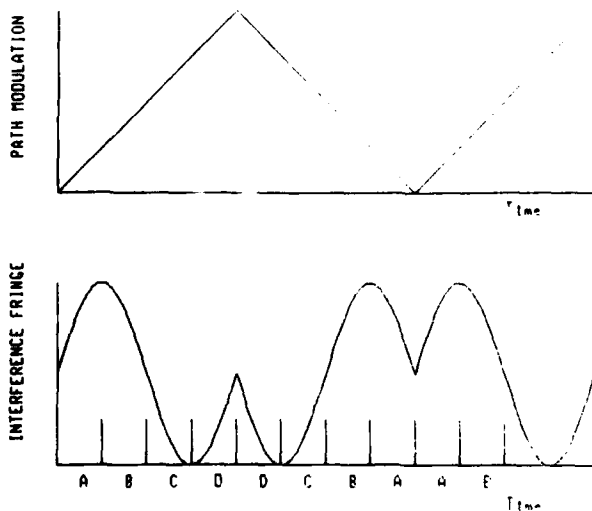


FIG. 2.—Stellar fringe modulation/demodulation

is unbiased with respect to photon noise and dark count. In addition, it can be shown that this estimator is not biased by scintillation on time scales slower than the coherent integration time (Tango and Twiss 1980).

Atmospheric turbulence produces systematic reductions in the measured visibility. The use of finite-diameter collecting apertures causes a reduction in visibility attributable to the relative tilts and curvatures of the interfering wavefronts. The use of a finite-length coherent integration time causes a reduction in visibility attributable to motion of the fringe during the interval. The reduction in visibility due to these effects can be approximated as (cf. Tango and Twiss 1980)

$$V_{\text{measured}} \approx V_{\text{true}} \exp \left[-1.03 \left(\frac{D}{r_0} \right)^{5/3} \right] \quad (2)$$

and

$$V_{\text{measured}} \approx V_{\text{true}} \exp \left[-0.5 \left(\frac{\tau}{\tau_0} \right)^{5/3} \right] \quad (3)$$

for D/r_0 and $\tau/\tau_0 \ll 1$. In these expressions, D and τ are the aperture diameter and coherent integration time; r_0 is the coherence diameter, i.e., that diameter aperture over which the rms wavefront fluctuations are approximately equal to 1 radian; and τ_0 is the coherence time, i.e., that time interval during which the rms fluctuations of the interference fringe are equal to 1 radian. Equation (2) assumes the use of a slow angle tracker—one which removes only systematic pointing errors. With a fast angle tracker, which removes some of the wavefront tilt, the reduction in visibility can be made smaller. For 1" seeing with a 10 m s^{-1} wind, $r_0 \approx 14 \text{ cm}$ and $\tau_0 \approx 12 \text{ ms}$ at 700 nm ; with $D = 2.5 \text{ cm}$ and $\tau = 4 \text{ ms}$, the visibility reduction is approximately 13.4%.

An additional source of error is finite temporal coherence. For example, with a bandpass filter which is 40 nm wide and a one-fringe servo tracking error, the reduction in fringe visibility is 0.5%. With the 10 nm wide filter used for these measurements, the visibility reduction due to partial temporal coherence is very small. This large usable optical bandpass is a significant advantage of stellar interferometers that track the central fringe.

A final source of bias is the instrument itself. An asymmetrical beamsplitter and the wavefront distortion caused by imperfect optics will both lower the visibility. Our calibration procedure for systematic errors due to the atmosphere and the instrument consists of observing a star whose intrinsic visibility is over 95%. Thus, as part of the observing sequence, unresolved stars are periodically measured.

The data analysis procedure begins with a data qualification step. Depending on the seeing, the fringe tracker will remain locked for a period of a few tenths of a second to several minutes. Data are recorded only when the fringe tracker is locked. In the data analysis, a short segment of data at the beginning and end of each lock representing the acquisition and loss of the fringe is discarded. In addition, if the length of the contiguous track of data is less than 0.5 s , the data is also discarded. From this qualified data, V^2 is calculated and averaged to 10 s .

After the quantity V^2 is averaged to 10 s , the next step is to correct for the biases described earlier. This is done by normalizing the measured visibilities by the visibility of an unresolved star. β Tau was used as the reference star for these observations. Its diameter can be estimated from its spectral type,

luminosity class, and magnitude as 1.3 mas , which yields an assumed visibility of 98.6% for a projected baseline of 12 m . (Comparable diameter estimates of 1.1 mas and 1.6 mas were found by Wesselink, Paranya, and De Vorkin 1972; and Hertzprung 1922, respectively.) From measurements of β Tau, the normalization constant for these measurements was determined as 0.751, i.e., a visibility reduction of 24.9%. α Leo, which has a measured diameter (Hanbury Brown, Davis, and Allen 1974) was not used as a calibrator because it was at a much larger zenith distance and was observed only for a short period of time.

Figure 3 shows the normalized visibilities for the seven stars observed. The gaps in the plot are caused by temporarily poor seeing during which the fringe tracker would not stay locked on the white-light fringe for more than 0.5 s ; these data are rejected by the data selection algorithm. Estimates of the coherence parameters for this data set are $r_0 \approx 20 \text{ cm}$ and $\tau_0 \approx 11.4 \text{ ms}$ (cf. Colavita, Shao, and Staelin 1987), corresponding to slightly better than 1" seeing. With these values, the visibility reduction due to the atmosphere is approximately 11.3%. Thus, given the normalization constant determined above, the reduction in visibility attributable to the instrument is approximately 15.4%.

In order to evaluate the stability and accuracy of our measurements, we measured the variance of the raw V^2 measurements, integrated for 10 s , over a period of 3 hr . This was compared to the theoretical variance due to photon noise. The photon noise variance for the V^2 estimator of equation (1) is given by

$$\sigma^2 = \frac{\pi^4}{4} \frac{1}{M} \frac{1}{N^2} \left(1 + \frac{4}{\pi^2} NV^2 \right), \quad (4)$$

where V is the raw visibility, N is the number of photons per frame (4 ms), and M is the number of frames. Table 1 shows the measured and theoretical variance of V^2 for the three stars β Tau, β Gem, and α CMi. There were insufficient data on the other stars for a meaningful variance measurement.

Table 1 shows that the fluctuations of the raw V^2 measurements are consistent with photon noise, which is at the 1%–3% level for a 10 s integration. As discussed earlier, the measured visibility is dependent upon the atmospheric seeing. Thus, if the seeing changes during a series of observations, i.e., if r_0 and τ_0 do not remain constant, the variance of the measured V^2 will be larger than the theoretical photon noise variance given by equation (4). The good agreement of the measured and theoretical values, which correspond to standard deviations of only 1.2% for β Gem and α CMi, indicates that atmospheric turbulence should not be a significant source of error in this set of measurements.

In general, the sensitivity of the measured visibility to changes in r_0 and τ_0 is easily determined from equations (2) and (3):

$$\frac{\Delta V_{\text{measured}}}{V_{\text{measured}}} \approx 1.72 \left(\frac{D}{r_0} \right)^{5/3} \left(\frac{\Delta r_0}{r_0} \right) \quad (5)$$

TABLE 1
MEASURED AND THEORETICAL VARIANCE OF V^2

Star	N	M	V^2 (raw)	σ_{theor}^2	$\sigma_{\text{measured}}^2$
β Tau	4.22	2500	0.548	10.6×10^{-4}	8.4×10^{-4}
β Gem	13.45	2500	0.137	0.94×10^{-4}	1.33×10^{-4}
α CMi	16.26	2500	0.337	1.31×10^{-4}	1.40×10^{-4}

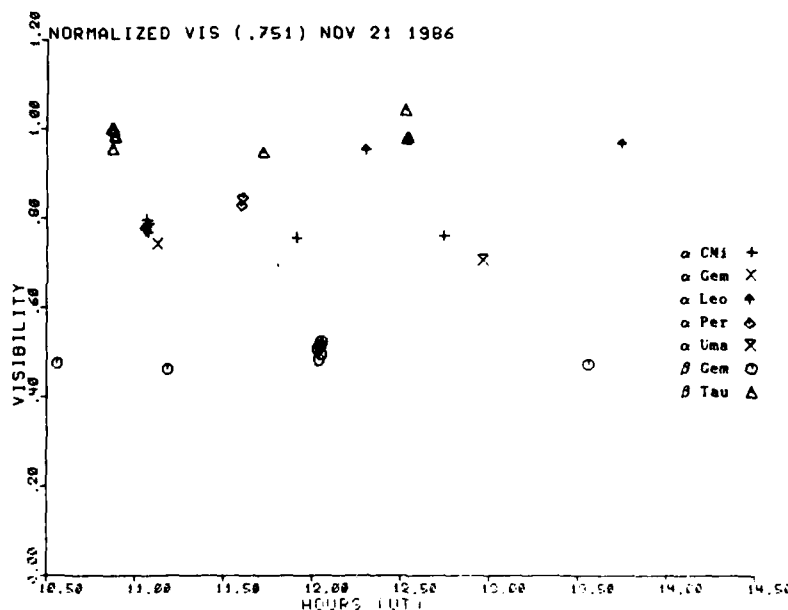


FIG. 3.—Normalized visibilities for seven stars observed on 1986 November 21

and

$$\frac{\Delta V_{\text{measured}}}{V_{\text{measured}}} \approx 0.83 \left(\frac{\tau}{\tau_0} \right)^{5/3} \left(\frac{\Delta \tau_0}{\tau_0} \right) \quad (6)$$

Using the estimated parameters for this data set, 10% changes in r_0 and τ_0 lead to changes in the measured visibility of 0.5% and 2.0%, respectively. In addition, the precise values of the coherence parameters depend on zenith angle. The coherence diameter r_0 is inversely proportional to the $\frac{2}{3}$ power of the turbulence strength, and thus has a zenith angle dependence $r_0 \propto \cos^{3/5} z$. The coherence time τ_0 is approximately proportional to r_0/W , where W is the wind speed normal to the propagation path. Averaging W with respect to wind direction yields for τ_0 an approximate zenith angle dependence $\tau_0 \propto 2 \cos^{3/5} z / (1 + \cos z)$. Using the estimated parameters for this data set, the systematic reduction in measured visibility at a 30° zenith angle is approximately 0.7%. These systematic visibility reductions have been factored into the normalized visibilities.

Beginning with our next observing season, when we begin observations of fainter stars, apertures larger than 2.5 cm and coherent integration times longer than 4 ms will be used. Consequently, turbulence-induced errors will increase, and careful calibration of atmospheric effects will be crucial. One analysis procedure that could be used to reduce these errors is to analyze the data with two different coherent integration times and two different coherent aperture sizes. With these measurements it will then be possible, in theory, to solve for both the true visibility as well as r_0 and τ_0 .

Stellar diameters are estimated from the normalized visibility, the effective wavelength of observation, and the projected baseline. The filter used for these observations was centered at 706 nm, and the projected baseline, routinely determined to one part in 10^6 as part of the astrometric data reduction, was nominally 12 m for observations at zenith. Assuming a uniform stellar disk, the diameters of several of the stars whose

normalized visibilities are shown in Figure 3 are presented in column (3) of Table 2. The uniform disk angular diameters were corrected for limb darkening based upon the appropriate model atmospheres from Carbon and Gingerich (1969) for α CMi, β Gem, and α UMa, and Parsons (1971) for α Per.

A cosine law was adopted and appropriate values for the limb-darkening coefficient were derived from the model atmospheres. The angular diameters were then corrected using the relationship between the limb-darkened diameter, the uniform disk diameter, and the limb-darkening coefficient given by Hanbury Brown and Twiss (1958). The estimated "true" diameters of the stars thus derived (Table 2, col. [4]) are 5%–7% larger than the equivalent uniform disks.

The errors given for the uniform disk diameters (col. [3]) are the formal rms errors in the measurement and in the normalization process. These errors include the effects of photon noise, as well as the uncertainties in the assumed angular diameter of the calibration star β Tau. As noted before, a true visibility of 98.6% was assumed for β Tau. We believe our estimate for the diameter of β Tau is good to $\pm 30\%$. A 30% error in the estimate of its diameter would produce a 1%

TABLE 2
STELLAR DIAMETERS AT 706 NANOMETERS

STAR (1)	TOTAL OBSERVED TIME (s) (2)	ANGULAR DIAMETER	
		Uniform Disk (mas) $\pm \sigma$ (rms) (3)	Limb Darkened Disk (mas) $\pm \sigma$ (rms) (4)
α CMi	80	6.15 \pm 0.25	6.44 \pm 0.25
β Gem	100	8.70 \pm 0.15	9.26 \pm 0.15
α Per	20	5.0 \pm 0.5 ^a	5.3 \pm 0.5 ^a
α UMa	10	7.2 \pm 0.4 ^a	7.6 \pm 0.4 ^a
α Gem	10	(multiple star)	
α Leo	20	(unresolved) >95% visibility	

^a Parentheses indicate theoretical photon noise error only.

change in the visibility used to normalize the other measurements. In addition, the errors include the effects of 10% rms fluctuations in the values of r_0 and τ_0 between observations of the calibrator of β Tau and the other stars. The errors in the limb-darkening corrections are estimated to be of the order of $\pm 0.5\%$ due to deviations in the (approximate) cosine relation used from the model atmospheres. This latter effect is included in the errors listed in column (4) of Table 2. While we believe all significant sources of error have been included, additional data with repeated observations at different baselines and at different wavelengths will be needed to confirm the accuracy of these diameter measurements.

IV. DISCUSSION

A limb-darkened angular diameter of 5.50 ± 0.17 mas was determined for α CMi by Hanbury Brown, Davis, and Allen (1974) from measurements at 440 nm made with the Intensity Interferometer. The limb-darkened angular diameters of β Gem and α Per found in the literature are 7.8 ± 0.6 mas (at 550 nm) by Faucherre *et al.* (1983) for β Gem, and 3.29 ± 0.25 mas (at 600 nm), and 2.9 ± 0.4 mas (at 550 nm) for α Per by Koechlin and Rabbia (1985) and Bonneau *et al.* (1981), respectively. Our measurement for α UMa shows reasonable agreement with an indirect estimate of the limb-darkened diameter based on absolute infrared photometry of 6.64 ± 0.21 mas by Blackwell and Shallis (1977).

Our diameter measurements are systematically larger than previous interferometric measurements. Consequently, we have looked for possible systematic biases to our measurements. α Leo was measured by Hanbury Brown to be 1.2 mas and should have given a visibility of 98.5%. Our measurement of α Leo gave a result of 96% with 2% rms photon noise. The discrepancy is 1.2σ . α Leo was not used as a calibrator because its photon statistics were poor. However, it does provide a check on our diameter measurements which are otherwise systematically different from previous measurements.

There are many possible sources of systematic error for our current and previous measurements. The seeing, r_0 , τ_0 can change with the seasons, the time of night, the average wind speed, and there may be effects that correlate with the magnitude and color of the star since the star tracker and fringe tracker work better on brighter stars and use detectors most sensitive to red light. The most important of these errors are included in our estimated errors in Table 2. We cannot explain the systematic difference between our recent measurements and previous measurements. However, these measurements were made at a longer wavelength than previous diameter measurements. In the past, observation of stellar fringes was a major accomplishment in itself. In the future, we expect the

emphasis will be on systematic errors such as the ones discussed in this paper and differences in measured diameters at different times would have astrophysical significance.

Future operation of the instrument will be different in three ways. Most important, with the installation of a new photon-counting camera as a part of the star-tracking system (1987 July), active fringe tracking and hence accurate visibility measurements will be possible for stars to at least $V = 5.0$ (probably to $V = 7$). These improvements will allow a dramatic increase in the number of stars available for study. We plan to conduct a long-term program to repeatedly observe the angular diameters of approximately 200 stars at many wavelengths.

In addition to providing direct measurements of photospheric angular diameters and limb darkening, we intend to observe a number of stars which are likely to possess extended atmospheres or shells through narrow-band filters or polarizers for evidence of resolved structures. Extended emission in H α from an envelope surrounding the Be star γ Cas has been reported by Thom, Granes, and Vakili (1986) from observations made with the CERGA I2T interferometer. We plan to observe this source as well as other Be stars with known IR excesses (Gehrz, Hackwell, and Jones 1974); supergiants such as ρ Cas, HR 8752 (Lambert, Hinkle, and Hall 1981), and P Cyg; and the Mira variables R Leo and χ Cyg. With the extension of the maximum baseline length to 20 m in 1987-1988, diameter measurements of the nearer Cepheid variables will be attempted.

Second, we plan to install a low-resolution spectrometer and photon-counting camera detector so that fringe visibility at all wavelengths can be measured simultaneously. Third, we plan to add software for real-time baseline calibration. This capability will allow operation as an absolute interferometer in order to make diameter measurements of objects up to 30 times fainter than the 7-mag limit of the fringe tracker using 5 cm apertures.

V. CONCLUSIONS

Stellar diameters of α CMi, β Gem, α Per, and α UMa measured with the Mark III stellar interferometer are reported. Values are given for the cases of uniform and limb-darkened disks. The measurements were performed using a totally automated instrument which will be capable of making measurements of stars brighter than $V = 7$ with diameters from $0''.003$ to $0''.015$ and located between 5° and 65° declination.

This work was made possible in part by NRL contract N00014-86-C-2105 and the Smithsonian Scholarly Studies Program.

REFERENCES

- Blackwell, D. E., and Shallis, M. J. 1977, *M.N.R.A.S.*, **180**, 177.
 Bonneau, D., Koechlin, L., Oneto, J. L., and Vakili, F. 1981, *Astr. Ap.*, **103**, 28.
 Carbon, D. F., and Gingerich, O. 1969, in *Theory and Observation of Normal Stellar Atmospheres*, ed. O. Gingerich (Cambridge, Mass.: MIT Press), p. 377.
 Colavita, M. M., Shao, M., and Staelin, D. H. 1987, *Appl. Optics*, **26**, 4106.
 Davis, J., and Tango, W. J. 1986, *Nature*, **323**, 234.
 Faucherre, M., Bonneau, D., Koechlin, L., and Vakili, F. 1983, *Astr. Ap.*, **120**, 263.
 Gehrz, R. D., Hackwell, J. A., and Jones, T. W. 1974, *Ap. J.*, **191**, 675.
 Hanbury Brown, R., Davis, J., and Allen, L. R. 1974, *M.N.R.A.S.*, **167**, 121.
 Hanbury Brown, R., and Twiss, R. Q. 1958, *Proc. R. Soc. London, A*, **248**, 199.
 Hertzsprung, E. 1922, *Ann. Sterrew. Leiden*, **14**, 1.
 Koechlin, L., and Rabbia, Y. 1985, *Astr. Ap.*, **153**, 91.

Labeyrie, A. 1975, *Ap. J. (Letters)*, 196, L71.

Lambert, D. L., Hinkle, K. H., and Hall, D. N. B. 1981, *Ap. J.*, 248, 638.

Mozurkewich, D., et al. 1987, *A. J.*, 93, 1280.

Parsons, S. B. 1971, *Ap. J.*, 164, 355.

Shao, M., et al. 1988, *Astr. Ap.*, in press.

Tango, W. J., and Twiss, R. Q. 1980, *Prog. Optics*, 17, 239.

Thom, C., Granes, P., and Vakili, F. 1986, *Astr. Ap.*, 165, L13.

Wesselink, A. J., Paranya, K., and De Vorkin, K. 1972, *Astr. Ap. Suppl.*, 7, 257.

M. M. COLAVITA and M. SHAO: Smithsonian Astrophysical Observatory, 60 Garden Street, Cambridge, MA 02138

J. L. HERSHEY, J. A. HUGHES, and G. H. KAPLAN: U.S. Naval Observatory, Washington, DC 20390

B. E. HINES and D. H. STAELIN: Massachusetts Institute of Technology, 26-339, Cambridge, MA 02139

D. J. HUTTER, K. J. JOHNSTON, D. MOZURKEWICH, and R. S. SIMON: Naval Research Laboratory, E. O. Hulburt Center for Space Research, Code 4130, Washington, DC 20375

Atmospheric phase measurements with the Mark III stellar interferometer

M. Mark Colavita, Michael Shao, and David H. Staelin

The Mark III interferometer is a phase-coherent stellar interferometer designed for astrometry. Operating through the turbulent atmosphere, the instrument is also a sensitive detector of atmospheric phase fluctuations. The effect of phase fluctuations on astrometric accuracy is reviewed, and phase measurements obtained with the instrument at Mt. Wilson using a 12-m base line are presented. These measurements agree well with the predictions of a simple Kolmogorov spatial spectrum over the frequency range of 0.001–100 Hz. From these measurements, the outer scale of turbulence for propagation through the entire atmosphere is estimated to be >2 km. The standard deviation for an absolute astrometric measurement estimated from these measurements is $\sim 0.14T^{-1/3}$ sec of arc for long integration times for conditions of 0.5-sec of arc seeing. For star-switched relative measurements, this error should decrease as the square root of the number of switching cycles.

1. Introduction

The Mark III astrometric interferometer is a phase-coherent white-light stellar interferometer designed for astrometry. It became operational on Mt. Wilson in Sept. 1986 using, at present, a 12-m N-S base line. It succeeds the 3.1-m Mark II interferometer¹ which operated on Mt. Wilson from Aug. 1982 until Sept. 1984 and incorporates a number of improvements over that instrument, especially in the area of thermal stability. The instrument measures the phase of the white-light fringe in two wide spectral channels covering ~ 0.6 – 0.9 and 0.4 – $0.6 \mu\text{m}$. The fringe phase in the red channel serves as the error signal for a white-light fringe servo which controls the position of a laser-monitored delay line, while the fringe phase in the blue channel is used with the two-color method. Continuous fringe tracks vary from a fraction of a second to tens of seconds, depending on the seeing. Figures 1 and 2 present a photograph of the Mark III interferometer site and a schematic diagram of the instrument. The instrument is discussed in detail in a separate paper.²

David Staelin is with Massachusetts Institute of Technology, Cambridge, Massachusetts 02139; the other authors are with Smithsonian Astrophysical Observatory, Cambridge, Massachusetts 02138.

Received 29 April 1987.

0003-6935/87/194106-07\$02.00/0.

© 1987 Optical Society of America.

Atmospheric turbulence is the fundamental factor limiting the performance of all ground-based astrometric instruments, affecting both sensitivity and accuracy. While in practice instrumental limitations can dominate performance, the intent in the design of the Mark III instrument was to keep systematic errors sufficiently small that atmospheric turbulence would be the only significant error mechanism when rapid star switching was employed. Section II describes the effects of turbulence on measurements of stellar position, both for the case of a simple Kolmogorov spatial spectrum, and for the case of a model incorporating a finite outer scale. Section III presents atmospheric phase measurements obtained with the Mark III interferometer at Mt. Wilson in the fall of 1986. Data from the Mark II instrument are also presented. Only one-color observations are considered in this paper. The use of two-color methods to reduce atmospheric errors is an important part of the operation of the Mark III instrument and is discussed in detail in a separate paper.³

II. Atmospheric Effects

After propagating through the turbulent atmosphere, an initially coherent wave will exhibit a finite coherence area and a finite coherence time. The coherence diameter r_0 is that aperture diameter over which the rms phase fluctuations of the wavefront are ~ 1 rad. With a slow angle tracker, this parameter is given by⁴

$$r_0 = 1.68 [k^2 \int_0^\infty dh C_n^2(h)]^{-3/5}, \quad (1)$$



Fig. 1. Site of the Mark III stellar interferometer at Mt. Wilson.

where k is a wavenumber, C_n^2 is the structure parameter, and the integration is over the propagation path. The spatial variance of the phase fluctuations across the interference fringe is approximately twice that of the fluctuations across a single wavefront. The coherence time T_0 is that time interval during which the rms phase fluctuations of the interference fringe are equal to 1 rad. With a slow fringe tracker, and for the case of

a long-base line interferometer, this parameter is given by⁵

$$T_0 = 1.36[k^2 \int_0^\infty dh C_n^2(h) V^{6/3}(h)]^{-3/5} \\ = 0.81(r_0/V), \quad V(h) = V, \quad (2)$$

where V is the wind speed. Finite values for r_0 and T_0 restrict the maximum usable subaperture size and the maximum usable coherent integration time for a stellar interferometer.

While atmospheric phase fluctuations limit the sensitivity of a ground-based interferometer, the more serious problem for astrometry is that the turbulent atmosphere corrupts the angle of arrival of the stellar wavefront, i.e., the apparent position of the star. The statistics of the angle-of-arrival process $\alpha(t)$ severely limit the accuracy possible from a single-color absolute astrometric measurement. The angle of arrival $\alpha(t)$ is related to fringe position $x(t)$ via $x(t) = \alpha(t)B$, where B is the interferometer base line and to phase difference $\Phi(t)$ via $\Phi(t) = kx(t)$, where $k = 2\pi/\lambda$ and λ is the wavelength of observation.

The most useful description of the angle-of-arrival process is its power spectrum $W_\alpha(f)$. In the geometric-optics approximation, the contribution to the power spectrum attributable to each atmospheric layer can

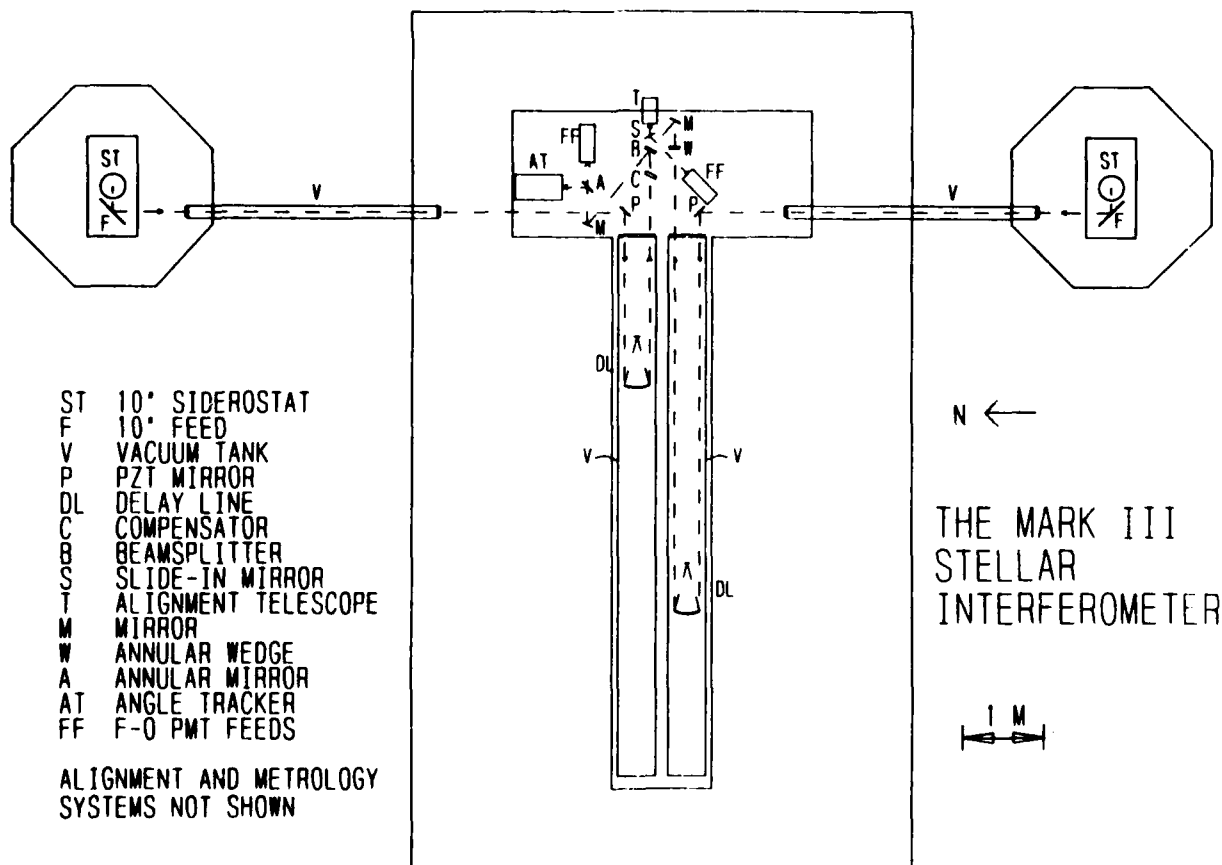


Fig. 2. Approximately to-scale schematic diagram of the Mark III stellar interferometer.

be computed independently⁶; the total spectrum is the sum of all such terms, taking into account the height dependence of C_n^2 and V . Using a spectral representation,⁷ the power spectrum $W_\alpha(f)$ can be written

$$W_\alpha(f) = 16\pi^2 B^{-2} \int_0^\infty dh V^{-1} \int_0^\infty du \\ \times \Phi \{ (u^2 + (\omega/V)^2)^{1/2} \} g(u, \omega), \quad (3)$$

where \vec{B} and \vec{V} are the base line and wind vectors, $\Phi(\kappa)$ is the refractivity spatial spectrum, and $\omega = 2\pi f$. The filter function $g(u, \omega)$ is given by $2[1 - \cos(B\omega/V)]$ when \vec{V} and \vec{B} are parallel ($\vec{V} \parallel \vec{B}$) and by $2[1 - \cos(u)]$ when they are perpendicular ($\vec{V} \perp \vec{B}$). Equation (3) is valid in the geometric-optics regime, i.e., for frequencies $f \ll V/\sqrt{\lambda L}$, where $\sqrt{\lambda L}$ is the Fresnel zone size and L is the height of the turbulent layer. The representation (3) can also be used to calculate the power spectra of relative and time-lagged relative astrometric measurements through the appropriate choice of the function $g(u, \omega)$.⁸

For the case $\vec{V} \parallel \vec{B}$ and a Kolmogorov spatial spectrum, $\Phi(\kappa) = 0.033C_n^2 \kappa^{-11/3}$, $W_\alpha(f)$ is given by⁹

$$W_\alpha(f) = 0.0654B^{-2} \int_0^\infty dh C_n^2 V^{6/3} [1 - \cos(2\pi f B/V)] f^{-8/3}, \quad (4)$$

where the nulls in Eq. (4) are artifacts of the frozen turbulence assumption. For the case $\vec{V} \perp \vec{B}$, the spectrum $W_\alpha(f)$ is smooth with a high-frequency asymptote equal to that of Eq. (4) and a low-frequency asymptote larger than that of Eq. (4) by the factor of $3/2$. Because of the uncertainty in the wind direction for most astronomical applications, Lindgren¹⁰ suggests averaging with respect to wind direction, which yields the average power spectrum

$$W_\alpha(f) = \frac{5}{4} 1.29 \int_0^\infty dh C_n^2 V^{-1/3} f^{-2/3}, \quad f \ll 0.20V/B, \quad (5a)$$

$$W_\alpha(f) = 0.0654B^{-2} \int_0^\infty dh C_n^2 V^{6/3} f^{-8/3}, \quad f \gg 0.20V/B. \quad (5b)$$

The error variance of a T -second absolute astrometric measurement can be written

$$\sigma_\alpha^2 = \int_0^\infty df W_\alpha(f) \text{sinc}^2(\pi f T), \quad (6)$$

where $\text{sinc}(x) = \sin(x)/x$. For $T \gg B/V$, Eq. (6) can be written¹⁰

$$\sigma_\alpha^2 = \frac{5}{4} 2.92 \left(\int_0^\infty dh C_n^2 V^{-1/3} \right) T^{-1/3}, \quad T \gg B/V. \quad (7)$$

For the case of 1-sec of arc seeing and a constant 10-m/sec wind speed, the value of $\int C_n^2 dh$ is $\sim 8.4 \times 10^{-13} \text{ m}^{1/3}$, and the error standard deviation can be written

$$\sigma_\alpha \approx 0.25 T^{-1/6} \text{ sec of arc}, \quad T \gg B/V. \quad (8)$$

These results are independent of the interferometer base line B and, implicit in the geometric-optics approximation, independent of wavelength. In addition, these results depend only weakly on integration time and wind speed, a consequence of the nearly $1/f$ nature of the atmospheric statistics. Very long inte-

gration times are thus required to obtain high absolute accuracies.

If a finite value for the outer scale L_0 is incorporated into the refractivity spatial spectrum, the astrometric error standard deviation in an absolute measurement will decrease more quickly than $T^{-1/6}$ for very long integration times. For the case $\vec{V} \parallel \vec{B}$, and a von Karman spatial spectrum,¹¹ $\Phi(\kappa) = 0.033C_n^2 (\kappa^2 + L_0^{-2})^{-11/6}$, the angle-of-arrival power spectrum (3) is given by¹²

$$W_\alpha(f) = 1.29 \int_0^\infty dh C_n^2 V^{-1/3} f^{-2/3} \\ \times [1 + (V/2\pi f L_0)^2]^{-4/3}, \quad f \ll 0.23V/B. \quad (9)$$

The $f^{4/3}$ low-frequency asymptote predicted by Eq. (9) makes strict demands on the validity of the frozen turbulence assumption,¹⁰ and this behavior would not be expected to be observed in practice.

A more conservative result of a flat low-frequency asymptote is obtained for the case $\vec{V} \perp \vec{B}$:

$$W_\alpha(f) = 6.6 \int_0^\infty dh C_n^2 V^{-1} \\ \times [L_0^{-2} + (2\pi f/V)^2]^{-1/3}, \quad f \ll 0.18V/B; \quad B \ll L_0 \quad (10a)$$

$$W_\alpha(f) = 6.6 \int_0^\infty dh C_n^2 V^{-1} \left(\frac{4}{3} \right) B^{-2} \\ \times [L_0^{-2} + (2\pi f/V)^2]^{-4/3}, \quad B \gg L_0. \quad (10b)$$

Averaging with respect to wind direction as in Eq. (5) yields low-frequency asymptotes equal to approximately one-half of the values given in Eq. (9), i.e.,

$$W_\alpha(f) = 3.3 \int_0^\infty dh C_n^2 V^{-1} L_0^{2/3}, \\ f \ll V/2\pi L_0; \quad B \ll L_0, \quad (11a)$$

$$W_\alpha(f) = 3.3 \int_0^\infty dh C_n^2 V^{-1} \left(\frac{4}{3} \right) (L_0/B)^2 L_0^{2/3}, \\ f \ll V/2\pi L_0; \quad B \gg L_0. \quad (11b)$$

Division of these results by $2T$ yields the error variance of an absolute astrometric measurement for integration times long compared with L_0/V . Thus, with a finite outer scale, the error standard deviation decreases as white noise for very long integration times. In addition, the standard deviation is smaller with a base line much longer than the outer scale. Unfortunately, it is likely that such base lines would be impractically large and would also resolve most of the stars of interest. Also, the base line necessary for a significant improvement in accuracy is dependent on the precise modeling of the low-spatial-frequency region of the refractivity spectrum. Using a Greenwood-Tarazano spatial spectrum^{13,14} rather than a von Karman spectrum to model this region yields a somewhat more pessimistic result than that presented in Eq. (11b).⁸

It seems highly likely that the appropriate value for the outer scale for vertical propagation through the atmosphere is significantly larger than the several-hundred-meter value often assumed. Dravskikh and Finkelstein¹⁵ estimate that the outer scale should be of

the order of the scale height of the troposphere, and that below this spatial frequency the 3-D spectrum should behave as $\kappa^{-8/3}$, a considerably more pessimistic result than either a von Karman or Greenwood-Tarazano model. From a number of observations of the phase structure function over base lines from 1 to 10 km obtained with the VLA radio-interferometric array, Armstrong and Sramek¹⁶ estimated a mean spatial spectrum obeying $\kappa^{-3.4}$ for those observations during which turbulent fluctuations were detectable. While the estimated $\kappa^{-3.4}$ power law represents a slight departure from a Kolmogorov spectrum at these base lines, their measurements do not appear to indicate an outer scale significantly smaller than that estimated above. While radio measurements are primarily sensitive to water vapor fluctuations, as opposed to temperature fluctuations for most optical measurements, it is expected that the outer scale for temperature turbulence should be at least as great as the outer scale for water-vapor turbulence.

The discussion above concerns only a single one-color absolute astrometric measurement. A significant improvement in error performance is obtained for relative measurements. The power spectra for such measurements have flat low-frequency asymptotes,¹⁰ even assuming an infinite outer scale, due to the rejection of low-spatial-frequency atmospheric energy. Relative astrometry with a single-beam interferometer is accomplished by star switching, in which the positions of a number of stars are repeatedly measured over a number of switching cycles. For such measurements, the error in the difference of two star positions, or in the difference between one star position and the centroid of the other positions, should decrease as the square root of the number of switching cycles. Since the absolute error has only a weak dependence on integration time, short dwell times per star per switching cycle are acceptable to maximize the number of cycles. In addition, short switching cycles are desirable to reject instrumental instabilities with time scales longer than the cycle time. Finally, it should be noted that a significant improvement in the error behavior of either an absolute or relative measurement can be obtained with the two-color method.³

III. Data from the Mark III and Mark II Interferometers

The data from the Mark III interferometer to be presented below were obtained in the fall of 1986 at Mt. Wilson. Common instrumental parameters for these observations were a 12-m N-S base line, 2.5-cm diam collecting apertures, and a 4-msec coherent integration time for the red channel. The effective wavelength in the red channel for these observations was $\sim 0.7 \mu\text{m}$. The observations below are of bright stars which provided at least 500 photons/4 msec at a visibility of ~ 0.5 . The high SNR simplified the phase unwrapping necessary to estimate the high-frequency atmospheric phase fluctuations. The first data set is from a short scan of α Aql starting at 2.8-h UT on 6 Nov. 1986. The second data set is from a 3-h observation of β Cas starting at 2.8-h UT on 25 Nov. 1986. The

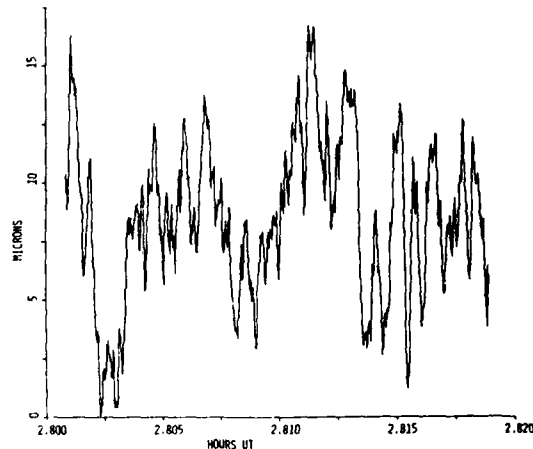


Fig. 3. Fringe position for α Aql, 6 Nov. 1986.

third data set is from a 1.4-h observation of β Gem starting at 12.2-h UT on 30 Oct. 1986. These data are excerpted from a much larger data set designed to evaluate instrumental stability and demonstrate rapid star switching; these astrometric observations are reported separately.¹⁷

The Mark III interferometer employs active fringe tracking. The white-light fringe position $x(t)$ is given by

$$x(t) = L(t) + \phi(t)/k, \quad (12)$$

where $L(t)$ is the position of the laser-monitored delay line, $\phi(t)$ is the fringe phase, and $k = 2\pi/\lambda$. The fringe phase ϕ is the tracking error of the white-light fringe servo. It is measured via a path-length modulation scheme and used to control the delay-line position. The following three figures illustrate the operation of the fringe tracker.

Figure 3 is a time domain plot of fringe position for α Aql at a resolution of 100 msec/point after subtraction of the systematic sidereal motion. Peak-to-peak excursion over ~ 72 sec are $\sim 16 \mu\text{m}$. This level of fluctuation, corrected for the high-pass filtering of the finite segment length, corresponds to ~ 0.3 -sec of arc seeing for this segment of data. In general, the variance of the fringe position fluctuations would be expected to be given by⁴

$$\sigma_x^2 = 6.88k^{-2}(B/r_0)^{5/3}. \quad (13)$$

Figure 4 is a plot of fringe phase, i.e., the error of the fringe servo. These data behave as a highpass-filtered version of the fringe position and exhibit rms fluctuations of $\sim 0.1 \mu\text{m}$. A clearer indication of the operation of the fringe servo is provided by the power spectra of these data presented in Fig. 5. These spectra are consistent with a first-order servo with a closed-loop bandwidth of 20 Hz, as implemented by the real-time system.

The next figure is for the 3-h track of β Cas. These data consisted of a number of separate fringe locks with a somewhat lower duty cycle toward the end of the data due to changing seeing. Again, a power spectrum

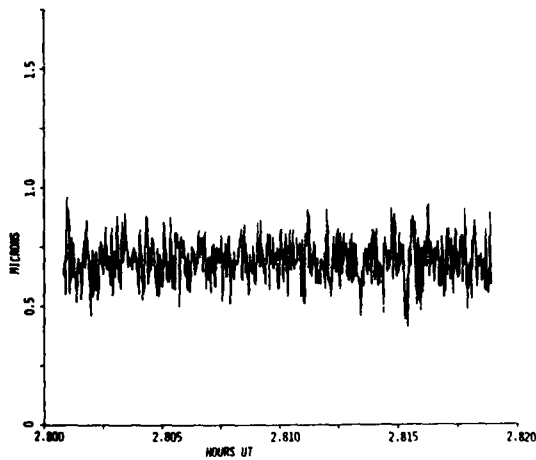


Fig. 4. Fringe servo error for α Aql, 6 Nov. 1986.

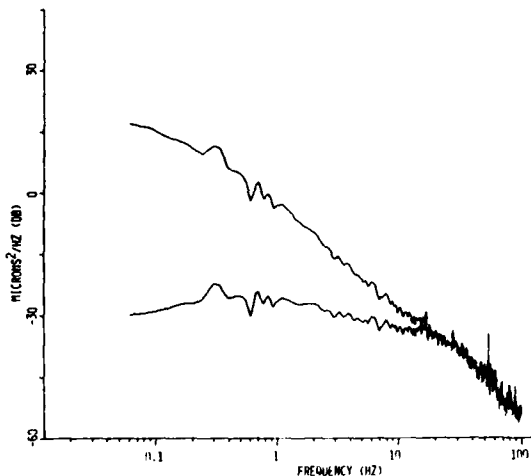


Fig. 5. Power spectra of fringe position and servo error for α Aql, 6 Nov. 1986.

provides the most information about the data, and one is presented in Fig. 6. Asymptotes corresponding to $f^{-2/3}$ and $f^{-8/3}$ power laws are indicated, and good correspondence to a Kolmogorov spatial spectrum over the 0.001–100-Hz frequency range is observed. Good agreement with the Kolmogorov model has also been obtained by others in laser propagation experiments over short horizontal paths (<150 m) with base lines of <30 cm.^{18,19}

From the frequency of intersection of the high- and low-frequency asymptotes of Fig. 6, an effective wind speed of 14 m/sec is estimated using Eq. (5). From the high-frequency asymptote $W_n(f) = 1.1 \times 10^{-14} f^{-8/3}$, a value of the coherence time $T_0 \approx 15$ msec at the effective wavelength of $0.7 \mu\text{m}$, or 11 msec at $0.55 \mu\text{m}$, is estimated using Eq. (2). By comparison, for the data of Fig. 5, the coherence time is estimated as 18 msec at $0.55 \mu\text{m}$.

The low-frequency asymptote of Fig. 6 is given by $W_n(f) = 2.0 \times 10^{-13} f^{-2/3}$, valid for frequencies between

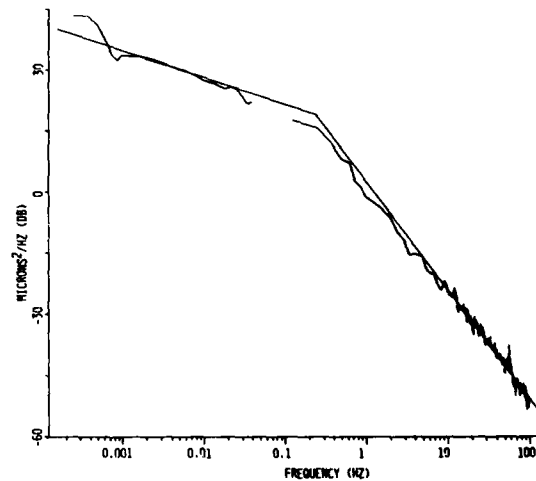


Fig. 6. Power spectrum of fringe position for β Cas, 25 Nov. 1986.

~ 0.001 and 0.1 Hz. Using this value and the effective wind speed of 14 m/sec in Eqs. (5) and (1) yields a value of the coherence diameter $r_0 \approx 25$ cm at $0.7 \mu\text{m}$, or 19 cm at $0.55 \mu\text{m}$, for seeing ($\approx \lambda/r_0$) of 0.5 sec of arc. Using Eq. (7), this value of the low-frequency asymptote corresponds to an atmospherically limited absolute astrometric accuracy of $0.147^{-1/6}$ sec of arc for long integration times or ~ 0.065 sec of arc for a 100-sec integration time. This value is somewhat smaller than the value estimated in Eq. (8), which assumed worse seeing, and should decrease as the square root of the number of switching cycles for a star-switched relative measurement.

At frequencies below 10^{-3} Hz, fluctuations with a power spectrum much steeper than $f^{-2/3}$ are observed in the data of Fig. 6. These can be identified as random instrumental errors, especially thermal drifts. Prior experiments investigating the thermal stability of the instrument characterized these instabilities as obeying power laws between f^{-3} and f^{-4} at very low frequencies. Rapid star switching, with cycles times much shorter than 1000 sec, should be adequate to eliminate astrometric errors due to these instabilities. It is possible that some fraction of these errors are due to imperfections in the siderostat bearings, an error which cannot be reduced by star switching. Additional laser metrology of the siderostats is required to eliminate this error source. Such a system should be installed on the Mark III instrument in 1987.²

At frequencies as low as 10^{-3} Hz, good correspondence is observed to a simple Kolmogorov model, i.e., one with an infinite outer scale. Using this frequency with a 14-m/sec wind, Eq. (10) places a lower bound on the value of the outer scale at ~ 2 km. As mentioned earlier, it is likely that the true value is still somewhat greater than this. Hopefully, future measurements with the Mark III interferometer will provide a better estimate of this parameter.

Figure 7 presents a power spectrum of fringe position for β Gem. Behavior similar to that of Fig. 6 is observed, with an identical high-frequency asymptote,

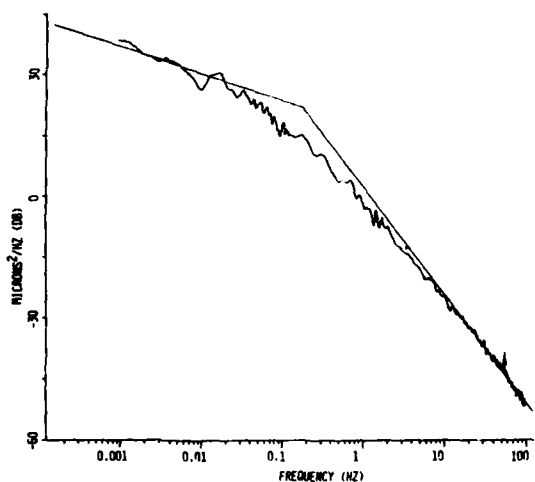


Fig. 7. Power spectrum of fringe position for β Gem, 30 Nov. 1986.

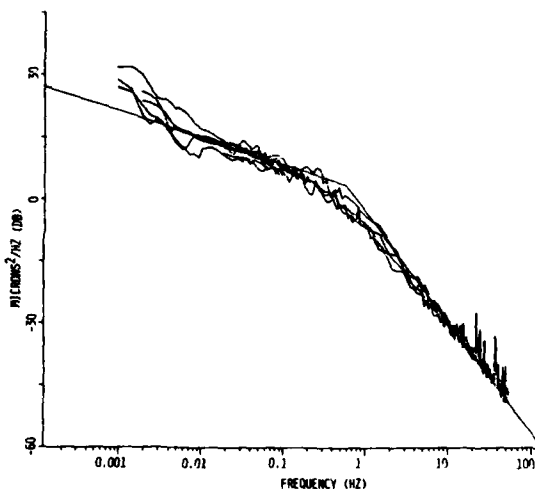


Fig. 8. Composite power spectrum of fringe position obtained with the Mark II interferometer, Aug. and Sept. 1983.

and a slightly larger low-frequency asymptote of $\sim 3.5 \times 10^{-13} f^{-2/3}$, corresponding to $r_0 \approx 14$ cm at $0.55 \mu\text{m}$. Finally, for comparison, Fig. 8 presents a composite power spectrum of several nights of data obtained in Aug. and Sept. 1983 with the earlier Mark II interferometer at Mt. Wilson. Instrumental parameters were similar to those for the Mark III instrument with the exception of a 3.1-m N-S base line. Low- and high-frequency asymptotes corresponding to a Kolmogorov spectrum are indicated. These data are characterized by values of r_0 and T_0 of ~ 25 cm and 24 msec at $0.55 \mu\text{m}$, with an effective wind speed of ~ 8.5 m/sec. Thermal instabilities in the instrument are worse than for the Mark III and are evident at frequencies below $\sim 10^{-2}$ Hz. These arose because the Mark II instrument was constructed on a steel optical table exposed to the nighttime air.

IV. Conclusions

A phase-coherent stellar interferometer, such as the Mark III interferometer, in addition to being a powerful astronomical instrument, is also capable of providing high-resolution measurements of the atmospheric phase process. Measurements of phase difference at a 12-m base line obtained with the Mark III interferometer agree well with the predictions of a Kolmogorov spatial spectrum over the 0.001–100-Hz frequency range. On the basis of these measurements, the outer scale for vertical propagation through the entire atmosphere does not appear to be smaller than a few kilometers. Measurements at Mt. Wilson indicate a one-color atmospherically limited absolute error standard deviation of ~ 0.065 sec of arc for a 100-sec integration in conditions of 0.5-sec of arc seeing. This error should decrease as the square root of the number of switching cycles for a star-switched relative measurement. Greater improvement should be possible with two-color techniques.

The authors wish to acknowledge the important contributions of P. Cheimets, J. Pohlman, and C. Papa in the design and construction of the precise mechanical components of the system as well as the staff of Mt. Wilson Observatory for their cooperation and aid during the construction of the instrument. This project was made possible with support from the following grants and contracts: N00014-84-C-2082, N00014-84-C-2137, N00014-85-C-2212, N00014-86-C-2105, N00014-86-C-2114 from the Naval Research Laboratory; from the Smithsonian Institution directly and through its Scholarly Studies Program; AST79-19553 from the National Science Foundation; NAS-2-50 and NSG-7176 from NASA; ONR N00014-80-C-0348 from the Office of Naval Research.

References

1. M. Shao, M. M. Colavita, D. H. Staelin, K. J. Johnston, R. S. Simon, J. A. Hughes, and J. L. Hershey, "The Application of Interferometry to Optical Astrometry," *Astron. J.* **93**, 1280 (1987).
2. M. Shao *et al.*, "The Mark III Stellar Interferometer," submitted to *Astron. Astrophys.* (1987).
3. M. M. Colavita, M. Shao, and D. H. Staelin, "The Two-Color Method for Optical Astrometry: Theory and Preliminary Measurements with the Mark III Stellar Interferometer," *Appl. Opt.* **26**, in press (1987), this issue.
4. D. L. Fried, "Statistics of a Geometric Representation of Wavefront Distortion," *J. Opt. Soc. Am.* **55**, 1427 (1965).
5. W. J. Tango and R. Q. Twiss, "Michelson Stellar Interferometry," *Prog. Opt.* **17**, 239 (1980).
6. D. P. Greenwood and D. L. Fried, "Power Spectra Requirements for Wave-Front-Compensative Systems," *J. Opt. Soc. Am.* **66**, 193 (1976).
7. A. Ishimaru, *Wave Propagation and Scattering in a Random Media*, Vol. 2 (Academic, New York, 1978).
8. M. M. Colavita, "Atmospheric Limitations of a Two-Color Astrometric Interferometer," Ph.D. Thesis, MIT, Cambridge, MA (1985).
9. R. S. Lawrence and J. W. Strohbehn, "A Survey of Clear-Air Propagation Effects Relevant to Optical Communications," *Proc. IEEE* **58**, 1523 (1970).

10. I. Lindegren, "Atmospheric Limitations of Narrow-Field Optical Astrometry," *Astron. Astrophys.* **89**, 41 (1980).
11. R. L. Fante, "Electromagnetic Beam Propagation in Turbulent Media," *Proc. IEEE* **63**, 1669 (1975).
12. G. W. Reinhardt and S. A. Collins, Jr., "Outer-Scale Effects in Turbulence-Degraded Light-Beam Spectra," *J. Opt. Soc. Am.* **62**, 1526 (1972).
13. D. P. Greenwood and D. O. Tarazano, "A Proposed Form for the Atmospheric Microtemperature Spatial Spectrum in the Input Range," RADC Tech. Rep. RADX-TR-74-19 (1974).
14. C. S. Gardner, "Effects of Random Path Fluctuations on the Accuracy of Laser Ranging Systems," *Appl. Opt.* **15**, 2539 (1976).
15. A. F. Dravskikh and A. M. Finkelstein, "Tropospheric Limitations in Phase and Frequency Coordinate Measurements in Astronomy," *Astrophys. Space Sci.* **60**, 251 (1979).
16. J. W. Armstrong and R. A. Sramek, "Observations of Tropospheric Phase Scintillations at 5 GHz on Vertical Paths," *Radio Sci.* **17**, 1579 (1982).
17. D. Mozurkewich *et al.*, "Preliminary Measurements of Star Positions with the Mark III Stellar Interferometer," submitted to *Astron. J.* (1987).
18. S. F. Clifford, G. M. B. Bouricius, G. R. Ochs, and M. H. Ackley, "Phase Variations in Atmospheric Optical Propagation," *J. Opt. Soc. Am.* **61**, 1279 (1971).
19. H. Matsumoto and K. Tsukahara, "Effects of the Atmospheric Phase Fluctuation on Long-Distance Measurement," *Appl. Opt.* **23**, 3388 (1984).

Two-color method for optical astrometry: theory and preliminary measurements with the Mark III stellar interferometer

M. Mark Colavita, Michael Shao, and David H. Staelin

The two-color method for interferometric astrometry provides a means of reducing the error in a stellar position measurement attributable to atmospheric turbulence. The primary limitation of the method is shown to be turbulent water vapor fluctuations, which limit the amount of improvement over a one-color measurement obtainable with a two-color estimate. Secondary atmospheric effects caused by diffraction from small refractive-index inhomogeneities and differential refraction for the observation of stars away from zenith are shown to introduce errors that behave as white noise and which should usually not be significant. Other potential error sources due to photon noise, systematic instrumental effects, and imperfect data reduction are also considered. The improvement in accuracy possible with the two-color method is estimated as a factor of 5–10 over the corresponding one-color measurement. Some preliminary two-color measurements with the Mark III stellar interferometer at Mt. Wilson are presented which demonstrate a factor of ~5 reduction in the amplitude of the atmospheric fluctuations in a stellar position measurement.

1. Introduction

The accuracy of conventional ground-based astrometric measurements suffers from the deleterious effects of atmospheric turbulence. Because of the nature of the low-frequency differential atmospheric phase fluctuations, which behave almost as 1// noise,¹ very long integration times are usually required to obtain highly accurate measurements of stellar positions.^{2,3} However, the accuracy of such long-duration measurements is typically limited by systematic instrumental errors. For the case of relative astrometry,³ the situation is somewhat improved. However, the ultimate limitation to high accuracies remains the turbulent atmosphere. The application of the two-color method to interferometric astrometry^{4,5} provides a means for reducing the atmospheric contribution to the error in a stellar position measurement.

Two-color techniques for the precise measurement of long paths through the open atmosphere have been

used successfully for geodetic ranging^{6,7} and have application to satellite ranging^{8,9} and altimetry.¹⁰ In this case, the problem which the two-color techniques address is the determination of the path-averaged refractive index needed to convert an apparent measurement to the proper vacuum distance. In astrometric applications of two-color techniques, the interest is in the measurement of angles. Large atmospheric scales are thus rejected, and the nonunity atmospheric refractive index does not introduce errors. In this case, the two-color method is employed to correct the errors caused by turbulent fluctuations in refractive index, which usually contribute only a small amount to the error in the range-finder case.

The use of two-color techniques is similar in both the range-finder and astrometric cases. For astrometry, let α_1 and α_2 be the stellar positions, i.e., the angles of arrival, observed at wavelengths λ_1 and λ_2 . The two-color estimate of the stellar position α_{2C} can be written

$$\alpha_{2C} = \alpha_1 - D(\alpha_2 - \alpha_1), \quad (1)$$

where D is the atmospheric dispersion,

$$D = [n(\lambda_1) - 1] / [n(\lambda_2) - n(\lambda_1)], \quad (2)$$

and $n(\lambda_1)$ and $n(\lambda_2)$ are the atmospheric refractive indices at wavelengths λ_1 and λ_2 . For $\lambda_1 = 0.7 \mu\text{m}$ and $\lambda_2 = 0.5 \mu\text{m}$, the dispersion is ~87.1. In Eq. (1), the quantity α_1 is a measure of the true stellar position plus the instantaneous atmospheric error, while, in principle, $D(\alpha_2 - \alpha_1)$ is a measure of the atmospheric error

David Staelin is with Massachusetts Institute of Technology, Cambridge, Massachusetts 02139; the other authors are with Smithsonian Astrophysical Observatory, Cambridge, Massachusetts 02138.

Received 29 April 1987.

0003-6935/87/194113-10\$02.00/0.

© 1987 Optical Society of America.

only. Thus the quantity α_{2c} should be a measure of the true stellar position.

In practice, the two-color estimate (1) will be affected by photon noise in the measurement of the angle of arrival $\alpha = x/B$, where x is the fringe position and B is the base line length. Let σ_1^2, σ_2^2 be the photon-noise variances in the measurement of fringe phase at wavelengths λ_1, λ_2 during a coherent integration time of length T_c . Then the astrometric error variance of a T -second two-color measurement due only to photon noise can be written for large D as

$$\sigma_{PN}^2 \approx \left(\frac{D}{B}\right)^2 (k_1^{-2}\sigma_1^2 + k_2^{-2}\sigma_2^2)T_c/T, \quad (3)$$

where k is a wave number $2\pi/\lambda$. The photon-noise error is minimized for long base lines and small values of D , the latter requiring both a large separation between the two colors, and also that one of the colors be located in the blue region of the spectrum, where the atmosphere is most dispersive. To estimate the magnitude of the photon-noise error, let $\lambda_1 = 0.7 \mu\text{m}$ and $\lambda_2 = 0.5 \mu\text{m}$, for which $D = 87.1$. Let $\sigma_1^2 = \sigma_2^2 = 0.3^2 \text{ rad}^2$, which corresponds to ~ 100 -photons/coherent integration time for a fringe of 0.5 visibility. With $B = 12 \text{ m}$ and $T_c = 4 \text{ msec}$, the rms error in a 100-sec integration due to photon noise is 0.4 msec of arc; for longer observations, this error decreases as the square root of the integration time according to Eq. (3). Thus despite the large multiplier D in Eq. (1), the photon-noise error is quite small in even a short two-color observation.

However, there are other errors in the two-color estimate attributable to atmospheric turbulence which are usually more significant than the photon-noise error. The primary atmospheric error is due to turbulent water vapor, which obeys a different dispersion relation than dry air. Essentially, turbulent water vapor introduces an error which has the appearance of low-level leakage of the one-color atmospheric error into the two-color measurement. Secondary atmospheric effects include diffraction from small refractive-index inhomogeneities and differential refraction for the observation of stars away from zenith. These effects will usually be smaller than the effect due to water vapor and in addition decrease as the square root of the integration time. Section II considers the effects of turbulent water vapor, while Secs. III and IV consider the effects of diffraction and refraction. Section V presents some requirements on the quality of the instrument and on the data reduction necessary to yield accurate two-color position estimates. Finally, Sec. VI presents some preliminary two-color observations from the Mark III astrometric interferometer at Mt. Wilson. These observations show a factor of 5 reduction in the amplitude of the atmospheric fluctuations in an angle-of-arrival measurement.

II. Atmospheric Water Vapor Effects

Atmospheric turbulence is driven by microfluctuations in temperature, pressure, and water vapor with temperature fluctuations making the dominant contribution to refractivity fluctuations in the optical region.

The two-color method can eliminate the astrometric errors caused by microfluctuations in temperature and pressure; however, the method cannot simultaneously eliminate the errors caused by microfluctuations in water vapor.

At optical frequencies, the atmospheric refractivity, $N(\lambda) = n(\lambda) - 1$, can be written¹¹

$$N(\lambda) = A(\lambda)P/T - B(\lambda)e/T, \quad (4)$$

where P is total pressure in millibars, e is the partial pressure of water vapor in millibars, and T is temperature in kelvins. The wavelength dependence of the refractive index is given by the dispersion relations $A(\lambda)$ and $B(\lambda)$ ¹¹:

$$A(\lambda) = 10^{-8}[2372.434 + 684255.24/(130 - \sigma^2) + 4549.40/(38.9 - \sigma^2)], \quad (5a)$$

$$B(\lambda) = A(\lambda) - 10^{-8}[6497.31 + 58.058\sigma^2 - 0.71150\sigma^4 + 0.08851\sigma^6], \quad (5b)$$

where $\sigma = 1/\lambda$ in μm^{-1} . At $\lambda = 0.55 \mu\text{m}$, Eq. (4) can be written

$$N = 10^{-6}(79.01P/T - 12.26e/T). \quad (6)$$

Linearizing Eq. (6) for small parameter fluctuations and using the relation $Q \approx 217e/T$ between water vapor partial pressure and water vapor density Q , in g/m^3 , yield¹²

$$\Delta N = -[A(\lambda)P/T^2]\Delta T + [A(\lambda)/T]\Delta P - [B(\lambda)/217]\Delta Q = -a(\lambda)\Delta T + b(\lambda)\Delta P - c(\lambda)\Delta Q. \quad (7)$$

At optical wavelengths, this expression is usually dominated by temperature fluctuations. At $\lambda = 0.55 \mu\text{m}$, $P = 1013.25 \text{ mbar}$, and $T = 288.16 \text{ K}$, the values of the parameters a , b , and c in Eq. (7) are 0.96×10^{-6} , 0.27×10^{-6} , and 0.056×10^{-6} .

Consider now the two-color measurement given by Eq. (1). In the geometric-optics approximation, angle of arrival is proportional to the difference in integrated refractivity between the two interferometer beams. With this interpretation of ΔN , the instantaneous angle of arrival α at wavelength λ_i can be written

$$\alpha_i \approx -a(\lambda_i)\Delta T + b(\lambda_i)\Delta P - c(\lambda_i)\Delta Q. \quad (8)$$

Thus the two-color measurement [Eq. (1)] can be written

$$\alpha_{2c} \approx -a(\lambda_1)(1 - D/D_T)\Delta T + b(\lambda_1)(1 - D/D_P)\Delta P - c(\lambda_1)(1 - D/D_Q)\Delta Q. \quad (9)$$

where

$$D_T = D_P = A(\lambda_1)/[A(\lambda_2) - A(\lambda_1)], \quad (10a)$$

$$D_Q = B(\lambda_1)/[B(\lambda_2) - B(\lambda_1)], \quad (10b)$$

with $A(\lambda), B(\lambda)$ as given in Eqs. (5). Evaluation of Eqs. (10) at $\lambda_1 = 0.7 \mu\text{m}$ and $\lambda_2 = 0.5 \mu\text{m}$ yields $D_T = D_P = 87.1$ and $D_Q = -61.1$. Thus, while the dispersion constants for temperature and pressure fluctuations are equal, the dispersion constant for water vapor fluctuations is different from both of these and of the opposite sign. Thus the effects of temperature, pres-

sure, and water vapor on the refractive index cannot be corrected simultaneously when only two wavelengths are observed.

At visible wavelengths, Eq. (9) will usually be minimized by choosing $D = D_T$, leaving the residual

$$\alpha_{2c} \propto -c(\lambda_1)(1 + |D_T/D_Q|)\Delta Q. \quad (11)$$

Thus the ratio of the variance of the error in a two-color measurement to the variance of the error in a one-color measurement can be written

$$\frac{(\alpha_{2c}^2)}{(\alpha_1^2)} \approx \left[\frac{c(\lambda_1)}{a(\lambda_1)} \right]^2 \left(1 + \left| \frac{D_T}{D_Q} \right| \right)^2 \left[\frac{\int_0^\infty C_Q^2(h) dh}{\int_0^\infty C_T^2(h) dh} \right]. \quad (12)$$

Using the previous values of a , c , D_T , and D_Q , the coefficient of the structure constant ratio in Eq. (12) is equal to 0.021.

The ratio of variances in Eq. (12) could just as well be a ratio of power spectral densities, since the spectral behavior of temperature and water vapor fluctuations is identical.^{13,14} Thus the residual error in a two-color measurement will behave like the error in a one-color measurement, reduced in energy according to Eq. (12). It should be noted that a three-color technique could simultaneously correct errors due to temperature, pressure, and water vapor fluctuations. However, with all three colors in the optical region, the appropriate dispersion constants are of the order of 10^3 – 10^4 , and implementation would be somewhat difficult.

To estimate the improvement in accuracy possible with the two-color method, the value of the simultaneous ratio of the integrated water vapor turbulence to the integrated temperature turbulence is required. However, from available simultaneous measurements, only the point ratio C_Q^2/C_T^2 at low altitudes can be determined. Since the water vapor scale height is only ~ 2 km vs ~ 8 km for the dry atmosphere, these measurements should provide a conservative estimate of the integrated ratio. While none of these measurements was performed at night at an observatory-quality site, the measurements of Gossard¹⁵ seem most applicable. These measurements were made slightly inland from the Pacific coast at an elevation of several hundred meters. From comparison of the simultaneously measured temperature and humidity spectra, a value of 0.4 is determined for the ratio C_Q^2/C_T^2 . The values of this ratio estimated from other inland measurements¹⁶⁻¹⁸ range from 0.05 to 0.57.

Some additional measurements of interest are those of Armstrong and Sramek¹⁹ of the atmospheric phase structure function as measured with the VLA for base lines between 1 and 10 km. Approximating their empirical structure functions with a Kolmogorov model matched at a 1-km separation yields a mean value for the integrated radio refractivity of $\int C_n^2(\text{radio}) dh = 3.4 \times 10^{-12} \text{ m}^{1/3}$. This mean value applies to approximately two-thirds of their observations; there was no clear detection of the atmosphere in their remaining observations, which appeared to have a detection threshold of approximately $\int C_n^2(\text{radio}) dh = 10^{-12} \text{ m}^{1/3}$. A typical value of the integrated optical refractivity can be estimated using, for example, a Hufnagel

turbulence profile,^{20,21} which corresponds to ~ 1 sec of arc seeing, yielding $\int C_n^2(\text{optical}) dh = 6.2 \times 10^{-13} \text{ m}^{1/3}$. At radio frequencies, assuming dominant humidity fluctuations, $C_n^2(\text{radio}) = 3.5 \times 10^{-11} C_Q^2$, while at optical frequencies, assuming dominant temperature fluctuations, $C_n^2(\text{optical}) = 9.3 \times 10^{-13} C_T^2$.¹⁸ The ratio of these quite different nonsimultaneous measurements yields a value for the ratio of the integrated water vapor turbulence to the integrated temperature turbulence of 0.15, somewhat smaller than the point measurement cited above.

Thus, using the above parameters in Eq. (12), it is estimated that a factor-of-5–10 improvement in accuracy (standard deviation) over a one-color measurement should be possible using the two-color method. For example, the error in a one-color absolute astrometric measurement under the assumption of Kolmogorov turbulence and 1-sec of arc seeing is of the order of 0.1 sec of arc for a 100-sec integration.^{3,22} Thus, assuming a stable instrument, a two-color measurement of the same quantity should provide an accuracy of 0.01–0.02 sec of arc for the same integration time. Similar improvements should also be obtained for relative measurements and star-switched measurements, which have smaller one-color atmospheric errors.^{3,22}

While water vapor fluctuations are the primary atmospheric limitation of the two-color method, there exist several smaller sources of error caused by atmospheric turbulence; these are discussed in the next two sections. In these sections, a dry atmosphere is assumed so that there is no error due to turbulent water vapor.

III. Diffractive Effects

When diffraction is considered in the solution of the wave equation for propagation through turbulence, it is found that phase fluctuations, observed at different optical wavelengths, become decorrelated when caused by small refractive-index inhomogeneities.²³⁻²⁶ With widely spaced wavelengths, the size of the inhomogeneities below which decorrelation occurs is of the order of the Fresnel zone size $\sqrt{\lambda L}$, where λ is the mean wavelength and L is the height of the particular turbulent layer. Thus, in the absence of water-vapor fluctuations, this decorrelation limits the effectiveness of the two-color method at high temporal frequencies. Related problems arise in adaptive optics systems when the pointer and tracker beams are at different wavelengths.²⁷⁻³¹

The power spectrum of the error introduced into a two-color astrometric measurement by diffraction $W_{\text{diff}}(f)$ can be determined as follows. Let S_1, S_2 be the optical phases at wavelengths λ_1, λ_2 observed at one aperture of the interferometer. It will be convenient to neglect atmospheric dispersion in calculating the statistics of the error; thus let $S_1^* = S_1$ and $S_2^* = [1 + (1/D)]S_2$, where D is the dry-air dispersion and S_1, S_2 are the phases which would be observed in a nondispersive atmosphere. Thus the path-length error $d(t)$ in a two-color distance measurement at a single aperture can be written

$$d(t) = k_1^{-1}S_1'(t) - D[k_2^{-1}S_2'(t) - k_1^{-1}S_1'(t)] \\ = (D+1)[k_1^{-1}S_1(t) - k_2^{-1}S_2(t)], \quad (13)$$

where $k_i = 2\pi/\lambda_i$, $k_1 < k_2$. The error $d(t)$ has the power spectrum

$$W_d(f) = (D+1)^2 k_1^{-2} W_{S1S1}(f) + k_2^{-2} W_{S2S2}(f) \\ - 2k_1^{-1}k_2^{-1} W_{S1S2}(f), \quad (14)$$

where the terms $W_{SiSj}(f)$ are the optical phase power spectra and cross spectra. These spectra can be written²⁶

$$W_{SiSj}(f) = 8\pi^2 k_i k_j \int_{-\infty}^{\infty} \int_{-\infty}^{\infty} d\kappa d\kappa' [(\kappa V)^2 - (2\pi f)^2]^{-1/2} \\ \times \int_0^{\infty} dh g(\kappa, h) \Phi(\kappa, h), \quad (15)$$

where $g(\kappa, h)$ is the spectral filter function for phase fluctuations

$$g_{SiSj}(\kappa, h) = \cos[(1 - k_i/k_j)h\kappa^2/2k_i] \\ + \cos[(1 + k_i/k_j)h\kappa^2/2k_i], \quad (16)$$

In these equations, V is the transverse wind velocity and $\Phi(\kappa, h)$ is the refractivity spatial spectrum.

The power spectrum $W_d(f)$, Eq. (14), can be rewritten as a single integral of the form of Eq. (15), with filter function

$$g_d(\kappa, h) = \{1 + \cos(h\kappa^2/k_1)\} + \{1 + \cos[(k_1/k_2)h\kappa^2/k_1]\} \\ - 2\{\cos[(1 + k_1/k_2)h\kappa^2/2k_1] \\ + \cos[(1 - k_1/k_2)h\kappa^2/2k_1]\}, \quad (17)$$

which can be rewritten as

$$g_d(\kappa, h) = 4 \sin^2[(1 - k_1/k_2)h\kappa^2/4k_1] \\ + 4 \sin^2[(1 + k_1/k_2)h\kappa^2/4k_1] \\ - 2 \sin^2[(k_1/k_2)h\kappa^2/2k_1] - 2 \sin^2(h\kappa^2/2k_1). \quad (18)$$

Each term of the filter function $g_d(\kappa, h)$ has the same form as the filter function for log intensity fluctuations²⁶

$$g_{inl}(\kappa, h) = 8 \sin^2(h\kappa^2/2k_i). \quad (19)$$

Thus it is expected that the power spectrum $W_d(f)$ will have the same form as the log intensity power spectrum; in particular, the spectrum will be white for frequencies $f \ll V/\sqrt{\lambda L}$, which implies an astrometric error which decreases as the square root of the integration time. Substituting a smoothly varying Kolmogorov spectrum into Eq. (15), combining Eqs. (14), (15), and (18), and solving for the low-frequency asymptote yield

$$W_d(f) = 8\pi^2(D+1)^2 \int_0^{\infty} \kappa d\kappa (\kappa V)^{-1} \\ \times \int_0^{\infty} dh g_d(\kappa, h) 0.033 C_n^2(h) \kappa^{-11/3}, \quad f \ll V/\sqrt{\lambda L}. \quad (20)$$

Evaluating the κ integral yields

$$W_d(f) = 2.0(D+1)^2 F(k_1, k_2) \\ \times [\int_0^{\infty} dh h^{4/3} C_n^2(h) V^{-1}(h)], \quad f \ll V/\sqrt{\lambda L}, \quad (21)$$

where the auxiliary function $F(k_1, k_2)$ is given by

$$F(k_1, k_2) = 2\{(1 - k_1/k_2)/2\}^{4/3} \\ + 2\{(1 + k_1/k_2)/2\}^{4/3} - (k_1/k_2)^{4/3} - 1. \quad (22)$$

This function can be approximated by its first term to an accuracy of 12% for wave number ratios $k_1/k_2 \geq 1/2$.

The power spectrum for log intensity fluctuations is computed similarly, using the filter function (19), yielding²⁶

$$W_{inl}(f, k) = 7.94 k^{2/3} \\ \times [\int_0^{\infty} dh h^{4/3} C_n^2(h) V^{-1}(h)], \quad f \ll 0.57V/\sqrt{\lambda L}. \quad (23)$$

Combining Eqs. (21) and (23) allows the power spectrum of the path-length error at one aperture to be written in terms of the log intensity:

$$W_d(f) = 0.25(D+1)^2 k_1^{-2} F(k_1, k_2) W_{inl}(0, k_1), \quad f \ll V/\sqrt{\lambda L}. \quad (24)$$

Diffraction effects, acting like scintillations, will be uncorrelated for transverse separations in excess of a few Fresnel zones.¹ Thus the path-length errors at each aperture of the interferometer can be considered essentially independent, so that the error in angle of arrival for an interferometer of base line B can be written

$$W_{diff}(f) = 0.50(D+1)^2 B^{-2} k_1^{-2} F(k_1, k_2) W_{inl}(0, k_1), \quad f \ll V/\sqrt{\lambda L}, \quad (25)$$

where $W_{inl}(0, k_1)$ and $F(k_1, k_2)$ are given by Eqs. (23) and (22). For realistic integration times, only the low-frequency asymptote of $W_{diff}(f)$ is needed. However, the high-frequency asymptote is easily computed by assuming uncorrelated fluctuations at each wavelength. This yields a high-frequency power spectrum proportional to $f^{-8/3}$.

The astrometric error variance in a T -second integration due to diffraction effects can be written

$$\sigma_{diff}^2 \approx W_{diff}(0)/2T, \quad T \gg \sqrt{\lambda L}/V \quad (26)$$

for an error standard deviation which decreases as the square root of the integration time. Using a Hufnagel turbulence profile, the integral $\int dh h^{4/3} C_n^2(h)$ is equal to $6.2 \times 10^{-8} \text{ m}^{5/3}$. Assuming $B = 12 \text{ m}$, $V(h) = V = 10 \text{ m/sec}$, and $\lambda_1 = 0.7 \mu\text{m}$, $\lambda_2 = 0.5 \mu\text{m}$, for which $D = 87.1$ and $F = 0.14$, the low-frequency asymptotes (23) and (25) have values $W_{inl}(0) = 0.002$ and $W_{diff}(0) = 10^{-16}$. These yield a two-color error of $\sim 0.15 \text{ msec}$ of arc rms for a 100-sec integration. This should be a conservative result due to the assumptions of point receivers and a zero inner scale. Thus the astrometric error in a two-color position measurement due to diffraction should be negligible.

IV. Refractive Effects

A first-order analysis of the two-color method assumes that the beam paths in each color are identical. However, for observation of stars away from zenith, dispersive refractivity gradients transverse to the direction of propagation cause the beams to bend and the different color beams to separate. Since the beams then pass through different turbulence, the effectiveness of the two-color correction is diminished. The effect just described is purely geometric. It occurs even in the geometric-optics limit of wave propagation where the previously derived diffraction effects are nonexistent. Related problems arise in two-color geo-

detic and satellite ranging; previous studies,^{8,32} however, have concerned path-length rather than angle-of-arrival effects.

A full wave-optics solution to the propagation problem for separated two-color beam paths shows that the astrometric error caused by the combination of diffractive and refractive effects is not separable. However, it can be shown that the effect of the two mechanisms is bounded above by the rms sum of the contribution due to diffraction, calculated assuming coincident beam paths, as in the last section, plus the contribution due to geometric beam separation, calculated in the geometric-optics propagation limit.³³ Therefore, the following analysis will be carried out assuming geometric optics.

Light from a star at zenith angle θ undergoes a systematic astronomical refraction which displaces the refracted beam from an unrefracted beam path. Assuming an exponential plane-parallel atmosphere, the transverse displacement of these beams as a function of height h above the observatory can be written^{31,34}

$$\delta(h) = h_0 N(\lambda_1) \tan(\theta) \sec(\theta) \exp(-h_1/h_0) \exp(-h/h_0), \quad (27)$$

where $N(\lambda_1) = n(\lambda_1) - 1$ is the atmospheric refractivity at wavelength λ_1 , h_1 is the height of the observatory above sea level, and $h_0 \approx 8.3$ km is the scale height of atmospheric density. Since the atmosphere is dispersive, different colors undergo different amounts of bending. Assuming that the different-color beams are coincident at the earth's surface, the transverse beam separation as a function of height can be written

$$\Delta(h) = [h_0 N(\lambda_1)/D] \tan(\theta) \sec(\theta) \times \exp(-h_1/h_0) [1 - \exp(-h/h_0)], \quad (28)$$

where D is the atmospheric dispersion. For example, for a star at a zenith angle of 15° , a sea-level observatory, and a dispersion of 100, the beam separation at the top of the atmosphere is 6.4 mm.

Let $W_Z(f)$ denote the power spectrum of the angle-of-arrival error caused by refractive effects as calculated in the geometric-optics limit. Except for a factor of $(D + 1)^2$, the desired power spectrum has the same form as the power spectrum of a relative astrometric measurement $W_r(f)$ (Refs. 3,33):

$$W_r(f) = 10.5B^{-4/3} \int_0^\infty dh C_n^2(h) V^{-1}(h) \Delta^2(h), \quad f \ll 0.17V/B; \quad \Delta \ll B, \quad (29)$$

where $\Delta(h)$ is the separation of the beams from one aperture as a function of height. Therefore, the power spectrum of the astrometric error will be white at low frequencies. Substituting Eq. (28) for $\Delta(h)$ and letting $(D + 1)/D \approx 1$ yield

$$W_Z(f) = 10.5B^{-4/3} [h_0 N(\lambda_1) \exp(-h_1/h_0)]^2 \tan^2(\theta) \sec^4(\theta) \times \int_0^\infty dh C_n^2(h) V^{-1}(h) [1 - \exp(-h/h_0)]^2, \quad f \ll V/B, \quad (30)$$

a result which is nearly independent of wavelength. This result includes the factor $\sec^2(\theta)$ to account for the lengthening of the propagation path and a worst-case reduction of transverse wind velocity with zenith angle.

The astrometric error variance of a T -second integration due to refractive effects can be written

$$\sigma_z^2 \approx W_Z(0)/2T, \quad T \gg B/V \quad (31)$$

for an error standard deviation which decreases as the square root of the integration time. Using a Hufnagel turbulence profile, the value of the integral $\int dh C_n^2(h) [1 - \exp(-h/h_0)]^2$ is $1.3 \times 10^{-13} \text{ m}^{1/3}$. As in the last section, assume $B = 12$ m, $V(h) = V = 10$ m/sec, and $\lambda_1 = 0.7 \mu\text{m}$. For $h_1 = 1.74$ km (the elevation of Mt. Wilson), the astrometric error in 100-sec integration is 0.5, 1.5, and 3.8 msec of arc rms for sources at 15° , 30° , and 45° from zenith. Again, these results should be conservative due to the assumptions of point apertures, a zero inner scale, and geometric optics. Thus refractive effects should be negligible for observation of stars near zenith, and even for sources at 45° , the refractive error in a 100-sec integration should still be at least a factor of 25 below the one-color absolute astrometric error. Thus, for most two-color observations, refractive effects should not be a limiting factor.

V. Instrumental/Data Processing Considerations

The previous sections have considered fundamental sources of error in applications of the two-color method attributable to photon noise and atmospheric turbulence. This section discusses some practical considerations relating to the instrument and the data processing necessary to yield accurate two-color position estimates.

A potentially serious source of systematic error in a two-color measurement is due to mismatches in the thicknesses of dispersive materials in each arm of the interferometer. Let t denote the thickness mismatch of a material with refractivity $N_m = n_m - 1$. Then the residual error in a two-color fringe-position measurement at wavelengths λ_1 and λ_2 can be written

$$e_{2C} = t N_m(\lambda_1) (1 - \bar{D}/D_m), \quad (32)$$

where \bar{D} is the value of the atmospheric dispersion assumed in the data reduction, and $D_m = N_m(\lambda_1)/[N_m(\lambda_2) - N_m(\lambda_1)]$ is the material dispersion. In principle, with relative measurements, this residual error is not significant as long as it is stable with time. However, with a wideband instrument, the wavelengths λ_1 and λ_2 , and hence the dispersion D_m , will be dependent on the color of the star. To estimate the magnitude of fluctuations in e_{2C} , model the interferometer channels as rectangular with passbands of $0.44\text{--}0.56 \mu\text{m}$ for blue and $0.56\text{--}0.86 \mu\text{m}$ for red. Furthermore, assume that the starlight can be modeled with a blackbody spectrum over that range of wavelengths. Finally, assume that the dispersive material is fused silica. Then, for a range of temperatures from 2500 to 25,000 K, which models most of the stars to be observed, the range of D_m is from 63.1 to 65.3. Setting \bar{D} equal to its mean value of 87.1, the fluctuations in e_{2C} over this range of blackbody temperatures are approximately $0.02t$ P-P. To keep this error smaller than $0.1 \mu\text{m}$ requires $t < 5 \mu\text{m}$. Fortunately, this degree of matching is readily obtained by adjusting the angle of a compensating

plate. With the instrument configured as a Fourier transform spectrometer, this optic is adjusted until the central fringes in both channels are aligned to within approximately one-fourth of a fringe.

A random error results from the use of the incorrect wavelength or dispersion in the two-color data reduction, which introduces a leakage of the one-color spectrum into the two-color result. Let $x_1(t), x_2(t)$ be the fringe positions at wavelengths λ_1, λ_2 . Each of these positions is given by the sum of the position of the laser-monitored delay line L and the phase of stellar fringe ϕ , i.e., $x = L + \phi/k$. Using a tilde to denote the value of a parameter assumed in the data reduction, let $\tilde{k}_i = k_i(1 - \epsilon_i)$, where ϵ_i is the fractional wavelength error at λ_i , and let $\tilde{D} = D(1 + \epsilon_D)$. Then, to first order the residual error in a two-color measurement can be written

$$e_{2c}(t) = -(\epsilon_2 + \epsilon_D)L(t) + k_1^{-1}(D+1)(\epsilon_1 - \epsilon_2) - \epsilon_D\phi_1(t). \quad (33)$$

The processes $L(t)$ and $\phi_1(t)$ behave as low-pass and high-pass filtered versions of the angle-of-arrival process $\alpha(t)$. Thus for long integration times, the phase leakage term should become negligible, and the astrometric error of the two-color measurement should approach that of a one-color measurement, reduced in amplitude by $\epsilon_2 + \epsilon_D$. Therefore, even with several percent errors in D and k , it is possible to realize a greater than order-of-magnitude improvement in astrometric accuracy over a one-color measurement.

VI. Two-Color Observations with the Mark III Interferometer at Mt. Wilson

The Mark III astrometric interferometer is a phase-coherent white-light stellar interferometer designed for astrometry. Employing at present a 12-m N-S base line, the instrument became operational at Mt. Wilson in Sept. 1986. It succeeds the Mark II instrument which operated on Mt. Wilson from Aug. 1982 until Sept. 1984. The interferometer measures the phase of the white-light fringe in two wide spectral channels covering $\sim 0.6\text{--}0.9 \mu\text{m}$ and $0.4\text{--}0.6 \mu\text{m}$. The fringe phase in the red channel serves as the error signal for a white-light fringe servo which controls the position of a laser-monitored delay line, while the fringe phase in the blue channel is used off-line with the two-color method. A coherent integration time for the red channel of 4 msec is employed, during which time the quadrature components of the fringe phase in each channel are recorded, along with the delay-line position and other information. Continuous fringe tracks range in length from a fraction of a second to tens of seconds, depending on the seeing. The instrument is discussed in detail in a separate paper,³⁵ as are some one-color atmospheric phase measurements³² and some preliminary astrometric measurements.³⁶

The data below are from a 3-h track of β Cas starting at 2.8-h UT on 25 Nov. 1986. With 2.5-cm diam apertures, photon fluxes of 500 and 650 per 4 msec were observed in the red and blue channels, respectively, with average fringe visibilities of 0.5 and 0.3. The mean wavelengths in the red and blue channels, ob-

tained from a least-squares fit to several seconds of data, were $\lambda_1 = 0.704 \mu\text{m}$ and $\lambda_2 = 0.529 \mu\text{m}$ for a dry-air dispersion $D = 110$. Good seeing characterized most of this observation, with approximate values for the coherence diameter and coherence time of $r_0 \approx 25 \text{ cm}$ and $T_0 \approx 15 \text{ ms}$ at $0.7 \mu\text{m}$, corresponding to $\sim 0.5\text{-sec}$ of arc seeing. The next several paragraphs describe the data processing applied to the raw data collected by the real-time system.

Every 4 msec, during a fringe-lock, the phase of the white-light fringe in the red channel is estimated as

$$\hat{\phi}_1 = \tan^{-1} \delta [(Y_1 - X_1)/(Y_1 + X_1)], \quad (34)$$

where X_1 and Y_1 are the quadrature components for the red channel. These are given by $X = C - A$ and $Y = D - B$, where A, B, C , and D are the four bins into which photons are accumulated during a fringe scan.³⁵ The near-unity constant δ corrects for the difference between the effective red wavelength and the length of the path-length modulation stroke s ; for $\delta = 1$, $\hat{\phi}_1 = \tan^{-1}(Y_1/X_1) - \pi/4$. The quantity δ is given by

$$\delta = \cos\left(\frac{\epsilon}{4}\right) / \left[1 + \sin\left(\frac{\epsilon}{4}\right)\right], \quad (35)$$

where $\epsilon = 2\pi(s - \lambda_e)/\lambda_e$ is the number of radians by which the path-length modulation stroke exceeds the effective wavelength. A value of $\delta = 1.17$ was used in these reductions corresponding to $s = 0.633 \mu\text{m}$. The fringe phase ϕ is the error of the fringe servo; fringe position is actually given by

$$x(t) = L(t) + \phi(t)/k, \quad (36)$$

where L is the position of the laser-monitored delay line and $k = 2\pi/\lambda$.

The two-color phase difference ϕ_2 is $\phi_2 - (\lambda_1/\lambda_2)\phi_1$, where ϕ_2 is the fringe phase in the blue channel. As discussed in the Appendix, the coherence time of this signal can be several seconds. A two-color coherent integration time of 100 msec, comprising 25 4-msec one-color coherent integration times, was used in these reductions. Such long integration times allow the application of two-color techniques to cool stars which provide relatively small photon fluxes in the blue channel. The quantities accumulated each 4 msec are the quadrature components for the two-color phase difference

$$X_2 = Y_1 \sin[(\lambda_1/\lambda_2)\hat{\phi}_1] + X_1 \cos[(\lambda_1/\lambda_2)\hat{\phi}_1], \quad (37a)$$

$$Y_2 = Y_1 \cos[(\lambda_1/\lambda_2)\hat{\phi}_1] - X_1 \sin[(\lambda_1/\lambda_2)\hat{\phi}_1], \quad (37b)$$

where X_2 and Y_2 are the quadrature components for the blue channel. The error due to the mismatch between the effective blue wavelength and the length of the path-length modulation stroke tends to average to zero when these quantities are accumulated due to the randomizing effect of the fluctuations in $\phi_1(t)$. The estimated phase in the red channel is incoherently averaged during this time to yield $\hat{\phi}_1$. Thus, every 100 msec, the average two-color phase difference is estimated as

$$\bar{\phi}_2 = \tan^{-1}(\sum Y_2 / \sum X_2) - \pi/4, \quad (38)$$

and the two-color fringe position is given as

$$\bar{x}_{2C} = L + \bar{\phi}_1/k_1 - D\bar{\phi}_2/k_2. \quad (39)$$

From a preliminary first pass through the data using only a coarse sampling of the laser positions, an approximate base line is determined and used to subtract the diurnal component $s(t)$ from $x_{2C}(t)$ to yield the discriminant $\bar{x}_{2C}(t)$. In the absence of atmospheric and instrumental instabilities, $\bar{x}_{2C}(t)$ should be exactly zero. However, the two-color technique is sensitive to errors in the measurement of the fringe phases, and some degree of data qualification is necessary to reject anomalous data to prevent the introduction of biases into the two-color position. Additional qualification is necessary to deal with the problems of fringe hopping and phase unwrapping.

Implicit in the definition of fringe phase is proper reference to the central white light fringe. While the true fringe phase is an unambiguous quantity, equal to zero at the midpoint of the central fringe, this phase must be reconstructed from the estimates provided by Eq. (34), which are necessarily modulo 2π . Due to the finite tracker bandwidth, excursions of ϕ_1 can exceed $\pm\pi$, and thus some sort of phase unwrapping is necessary to maintain an analytic estimate. In addition, there is an ambiguity when initializing the unwrapper memory. A simple first-difference phase unwrapper for ϕ_1 was employed in the data reduction, and references to ϕ_1 above actually refer to the unwrapped quantity.

To simplify the data processing and minimize the propagation of unwrapping errors, the unwrapper memory is reset at the beginning of each 100-msec integration. This is equivalent to assuming that the initial value of ϕ_1 is within $\pm\pi$ of true zero phase. If this is not the case, due to an undetected unwrapping error by the real-time system which caused a secondary fringe to be temporarily tracked, or just due to a large excursion from the proper track point, the average phase $\bar{\phi}_1$ will be in error by $2\pi n$, where n is the number of fringes the initial value of ϕ_1 was removed from the central fringe. The two-color phase difference $\bar{\phi}_2$ will then be in error by $\text{mod}(-2\pi n\lambda_1/\lambda_2)$, where the modulo function is over the interval $-\pi$ to π , and the two-color position \bar{x}_{2C} will be in error by $\sim Dk_2^{-1} \text{mod}(-2\pi n\lambda_1/\lambda_2)$. Most fringe-hop errors correspond to $n = \pm 1$ which lead, for the parameters determined above, to two-color errors of approximately $\pm 20 \mu\text{m}$. Most other errors, such as phase-unwrapping errors during the two-color coherent integration time, do not have such a characteristic signature and are more difficult to reject.

Data selection was performed every 100 msec. For the quantity \bar{x}_{2C} , windows of approximately $\pm 1/2 D(\lambda_1 - \lambda_2) \approx \pm 10 \mu\text{m}$ were used to detect most of the fringe-hop errors described above. While these points could, in principle, be edited for inclusion into the data set, their frequency was such that it was simpler to just reject them. Data were also selected on the basis of

the fringe-amplitude SNR in the red and blue channels. This quantity is estimated as

$$F = (\pi^2/4N)(X^2 + Y^2), \quad (40)$$

where \hat{N} is the estimated photon flux for that scan. Rejecting those data points with very low SNRs eliminates a number of anomalous data points. After performing a second pass through the data using somewhat tighter windows for \bar{x}_{2C} , the data were averaged in groups of 10 to provide nominal 1-sec estimates of x_{2C} . A modified median filter was employed which averaged the median eight out of ten 100-msec points, selected again on the basis of \bar{x}_{2C} . Due to data selection, the 100-msec points were not necessarily continuous, and times were also averaged with the fringe positions to provide a mean time for each nominal 1-sec data point. The maximum time interval over which this incoherent averaging was performed was limited to 10 sec to eliminate smoothing errors prior to subtraction of the sidereal rate. For comparison, the one-color fringe position was estimated simultaneously with the two-color position, using the same qualified data and the same averaging scheme.

Figures 1 and 2 show the one- and two-color fringe positions, nominally 1-sec/data point, after subtraction of the sidereal rate. Figures 3 and 4 show this same data after simple averaging in ten-point groups to provide a resolution of nominally 10 sec/point. From these figures, it is clear that the use of the two-color method has significantly reduced the intermediate-frequency noise, presumably mostly atmospheric in origin. However, a low-frequency residual is clearly evident. The presence of this residual in both the one- and two-color plots suggests that it is a systematic instrumental drift. (The slight difference between the residuals at the ends of the one- and two-color data is due to systematic residual astronomical refraction in the one-color data, which is not present in the two-color position.)

The relative performance of the one- and two-color estimates becomes much clearer in the frequency domain. Power spectra were obtained using the 1-sec averaged data, interpolated where necessary to approximate uniform sampling. These spectra are shown in Fig. 5. All the data were used to estimate the spectra at the very lowest frequencies, while only the first half of the data, where the fraction of interpolated points was smallest, was used at intermediate frequencies. The power spectra are terminated at a frequency below that at which interpolation artifacts become significant. Systematic instrumental effects are visible in both the one- and two-color spectra at frequencies below $\sim 10^{-3}$ Hz. These errors typically have a power spectrum obeying power laws between f^{-3} and f^{-1} and are likely due to thermal instabilities.

At frequencies above $\sim 10^{-3}$ Hz, the power spectra are mostly atmospheric in nature. The one-color spectrum obeys the expected $f^{-2/3}$ power law, whose asymptote is indicated in the figure; the one-color spectral height corresponds to a turbulence-limited absolute astrometric accuracy of ~ 65 msec of arc for a

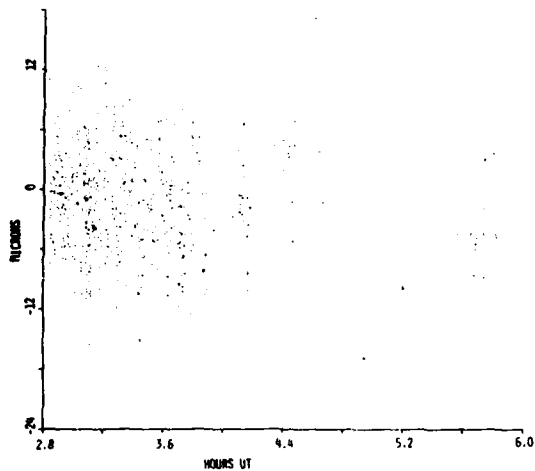


Fig. 1. One-color fringe position for β Cas, 25 Nov. 1986, at 1 sec/point.

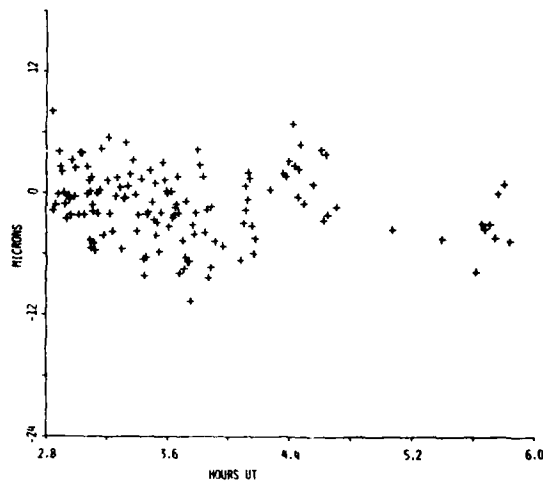


Fig. 3. One-color fringe position for β Cas, 25 Nov. 1986, at 10 sec/point.

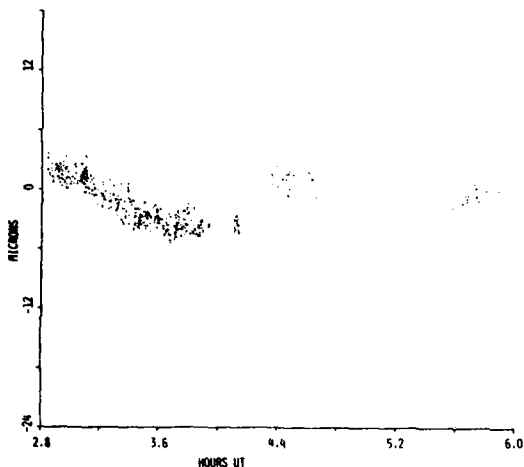


Fig. 2. Two-color fringe position for β Cas, 25 Nov. 1986, at 1 sec/point.

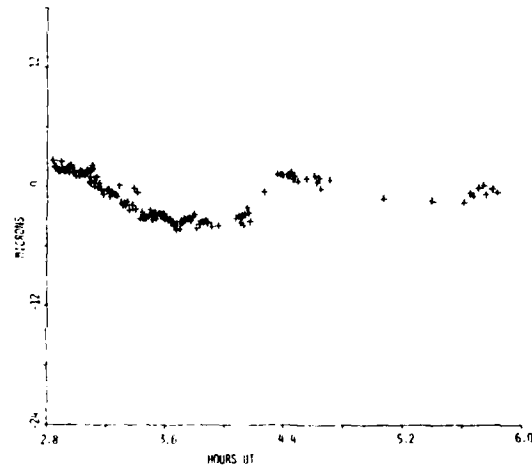


Fig. 4. Two-color fringe position for β Cas, 25 Nov. 1986, at 10 sec/point.

100-sec integration.²² Over most of the range above 10^{-3} Hz, the two-color spectrum shows about a 15-dB improvement over the one-color spectrum or a factor of ~ 5 reduction in error amplitude. The bump in the two-color spectrum near 0.0015 Hz is believed to be a siderostat drive error which is masked by atmospheric noise in the one-color spectrum. This error should be eliminated with additional laser metrology on the interferometer to be installed in the near future.

Thus, despite the limitations of the two-color method, which were discussed in the previous sections, these data indicate that a two-color absolute astrometric accuracy of ~ 13 msec of arc should be obtainable from a single 100-sec measurement. For star-switched relative measurements, this error should decrease as the square root of the number of switching cycles, so that wide-field relative accuracies of several msec of arc should be obtainable in a single night. While the effect of systematic errors and the applica-

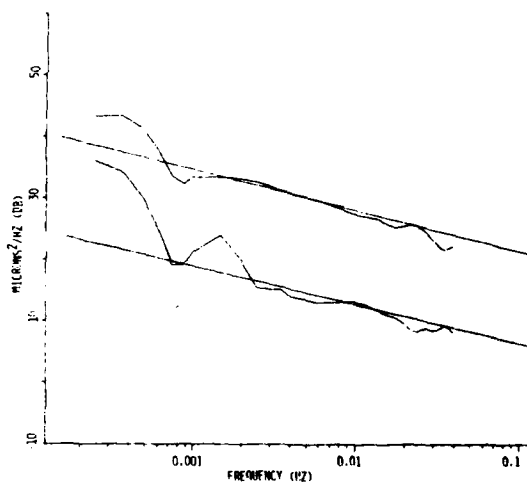


Fig. 5. Power spectrum of one- and two-color fringe positions for β Cas, 25 Nov. 1986.

tion of the two-color method to a large data set need to be explored experimentally, these preliminary results suggest that a significant improvement in the accuracy of ground-based astrometric measurements is possible with two-color techniques.

Appendix: Coherence of the Two-Color Phase Difference

Consider the two-color phase difference

$$\phi_2(t) = \phi_2 - (\lambda_1/\lambda_2)\phi_1, \quad (A1)$$

where ϕ_1 and ϕ_2 are the fringe phases at wavelengths λ_1 and λ_2 . Because of correlations between ϕ_1 and ϕ_2 , the coherence time of ϕ_2 will be much greater than that of either ϕ_1 or ϕ_2 . In the geometric-optics limit for observation of stars at zenith, ϕ_2 is equal to $(1/D)(\lambda_1/\lambda_2)\phi_1$, where D is the dispersion. As ϕ_2 is primarily a measure of the one-color atmosphere, water vapor can be ignored in this calculation. The atmospheric coherence time of the one-color phase ϕ_1 can be written^{22,27}

$$T_0 = 1.36[k_1^2 \int_0^\infty dh C_n^2(h) V^{5/3}(h)]^{-3/5}. \quad (A2)$$

Hence the coherence time T'_0 for the two-color phase difference ϕ_2 can be written

$$T'_0 = (D\lambda_2/\lambda_1)^{6/5} T_0. \quad (A3)$$

Using a Hufnagel turbulence profile with $V(h) = V = 10$ m/sec yields $T_0 = 13$ msec at $\lambda_1 = 0.7$ μm . Thus, with $\lambda_2 = 0.5$ μm , which gives $D = 87.1$, the two-color phase difference coherence time T'_0 is equal to 1.8 sec. With a coherent integration time for the two-color phase difference of T_c , the variance of the phase fluctuations about the interval mean can be written $\sigma_c^2 = (T_c/T'_0)^{5/3}$; these fluctuations cause a fractional visibility reduction of approximately $\sigma^2/2$ for $\sigma^2 \ll 1$. Thus, even with $T_c = 100$ msec, the reduction in fringe visibility is $<1\%$.

As discussed in Secs. III and IV, the effects of diffraction and refraction reduce the correlation between ϕ_1 and ϕ_2 . Consider the effects of diffraction for observation of a star at zenith. Assuming a low fringe-tracker bandwidth, the process ϕ_2 as given above will be proportional to $d(t)$ of Eq. (13). Therefore, the power spectrum of ϕ_2 will be proportional to $W_{\text{diff}}(f)$, Eq. (25). Using the notation of that section, the variance of ϕ_2 due to diffraction can be written

$$\sigma_d^2 = 0.50(\lambda_1/\lambda_2)^2 F(k_1, k_2) \sigma_{\text{int}}^2(k_1), \quad (A4)$$

where σ_{int}^2 is the variance of the log intensity.¹ The variance (A4) is an upper bound on the fluctuations about the interval mean which would occur in a finite coherent integration time. With a Hufnagel turbulence profile, the log intensity variance at 0.7 μm is given by $\sigma_{\text{int}}^2 \approx 0.2$. Thus, with $F(k_1, k_2) = 0.14$, the variance (A4) is given by $\sigma_d^2 = 0.03$ rad², which would lead to a maximum fractional visibility reduction of only 1.5%. Thus diffractive effects can be safely ignored.

Consider now the effect of refraction, computed, as in Sec. IV, in the geometric-optics limit. Assuming independent phase errors at each interferometer aper-

ture, the variance of ϕ_2 attributable to beam separation for a finite zenith angle is given by twice the phase structure function¹ evaluated at $\Delta(h)$, i.e.,

$$\sigma_z^2 = 2 \times 2.92 k_2^2 \int_0^\infty dh C_n^2(h) \Delta^{5/3}(h), \quad (A5)$$

where $\Delta(h)$ is given by Eq. (28) of Sec. IV. Substituting Eq. (28) into Eq. (A5) and incorporating an air mass correction yield

$$\begin{aligned} \sigma_z^2 = & 5.84 k_2^2 [h_0 N(\lambda_1) \exp(-h_1/h_0)/D]^{5/3} \\ & \times \tan^{5/3}(\theta) \sec^{8/3}(\theta) \int_0^\infty dh C_n^2(h) \\ & \times [1 - \exp(-h/h_0)]^{5/3}. \end{aligned} \quad (A6)$$

Using a Hufnagel turbulence profile, the final integral has a value of $1.5 \times 10^{-13} \text{ m}^{1/3}$. Using the parameters in Sec. IV, the variance σ_z^2 is equal to 0.03, 0.13, and 0.57 rad² for $\theta = 15, 30$, and 45° , which yields upper bounds to the fractional visibility reductions of $\sim 2, 7$, and 28% , respectively. These results were calculated assuming geometric optics, point apertures, and a zero inner scale for the turbulence. However, even at 45° zenith angle, the maximum beam separation is only ~ 3 cm; the Fresnel zone size, aperture diameter, and inner scale are all of this order. Therefore, these results should be fairly conservative, and refraction should not be a major limitation to long coherent integration times of the two-color phase difference.

The authors wish to acknowledge the important contributions of P. Cheimets, J. Pohlman, and C. Papa in the design and construction of the precise mechanical components of the system as well as the staff of Mt. Wilson Observatory for their cooperation and aid during construction of the instrument. This project was made possible with support from the following grants and contracts: N00014-84-C-2082; N00014-84-C-2137; N00014-85-C-2212; N00014-86-C-2105; N00014-86-C-2114 from the Naval Research Laboratory; from the Smithsonian Institution directly and through its Scholarly Studies Program; AST79-19553 from the National Science Foundation; NAS-2-50 and NSG-7176 from NASA; ONR N00014-80-C-0348 from the Office of Naval Research.

References

1. R. S. Lawrence and J. W. Strohbehn, "A Survey of Clear-Air Propagation Effects Relevant to Optical Communications," *Proc. IEEE* 58, 1523 (1970).
2. E. Høg, "Refraction Anomalies: The Mean Power Spectrum of Star Image Motion," *Z. Astrophys.* 69, 315 (1968).
3. L. Lindgren, "Atmospheric Limitations of Narrow-Field Optical Astrometry," *Astron. Astrophys.* 89, 41 (1980).
4. M. Shao and D. H. Staelin, "Long-Baseline Optical Interferometer for Astrometry," *J. Opt. Soc. Am.* 67, 81 (1977).
5. M. Shao and D. H. Staelin, "First Fringe Measurements with a Phase-Tracking Stellar Interferometer," *Appl. Opt.* 19, 1519 (1980).
6. K. B. Earnshaw and E. N. Hernandez, "Two-Laser Optical Distance-Measuring Instrument that Corrects for the Atmospheric Index of Refraction," *Appl. Opt.* 11, 749 (1972).
7. L. E. Slater and G. R. Huggett, "Multiwavelength Distance-Measuring Instrument for Geophysical Experiments," *J. Geophys. Res.* 81, 6299 (1976).

8. G. S. Gardner, "Effects of Random Path Fluctuations on the Accuracy of Laser Ranging Systems," *Appl. Opt.* **15**, 2539 (1976).
9. J. B. Abshire, "Pulsed Multiwavelength Laser Ranging System for Measuring Atmospheric Delay," *Appl. Opt.* **19**, 3436 (1980).
10. C. S. Gardner, "Technique for Remotely Measuring Surface Pressure from a Satellite using a Multicolor Laser Ranging System," *Appl. Opt.* **18**, 3184 (1979).
11. J. C. Owens, "Optical Refractive Index of Air: Dependence on Pressure, Temperature, and Composition," *Appl. Opt.* **6**, 51 (1967).
12. C. A. Friehe, J. C. La Rue, F. H. Champagne, and G. F. Dreyer, "Effects of Temperature and Humidity Fluctuations on the Optical Refractive Index in the Marine Boundary Layer," *J. Opt. Soc. Am.* **65**, 1502 (1975).
13. R. J. Hill, S. F. Clifford, and R. S. Lawrence, "Refractive-Index and Absorption Fluctuations in the Infrared Caused by Temperature, Humidity, and Pressure Fluctuations," *J. Opt. Soc. Am.* **70**, 1192 (1980).
14. E. E. Gossard, "Refractive Index Variance and its Height Distribution in Different Air Masses," *Radio Sci.* **12**, 89 (1977).
15. E. E. Gossard, "Power Spectra of Temperature, Humidity, and Refractive Index from Aircraft and Tethered Balloon Measurements," *IRE Trans. Antennas Propag.* **AP-8**, 186 (1960).
16. W. Kohsiek and M. H. A. J. Herben, "Evaporation Derived from Optical and Radio-Wave Scintillation," *Appl. Opt.* **22**, 2566 (1983).
17. G. A. McBean and J. A. Elliott, "Pressure and Humidity Effects on Optical Refractive-Index Fluctuations," *Boundary-Layer Meteorol.* **20**, 101 (1981).
18. R. W. McMillan, R. A. Bohlander, G. R. Ochs, R. J. Hill, and S. F. Clifford, "Millimeter Wave Atmospheric Turbulence Measurements: Preliminary Results and Instrumentation for Future Measurements," *Opt. Eng.* **22**, 32 (1983).
19. J. W. Armstrong and R. A. Sramek, "Observations of Tropospheric Phase Scintillations at 5 GHz on Vertical Paths," *Radio Sci.* **17**, 1579 (1982).
20. R. E. Hufnagel, "Variations of Atmospheric Turbulence," in *Technical Digest, Topical Meeting on Optical Propagation through Turbulence* (Optical Society of America, Washington, DC, 1974).
21. C. B. Hogge and R. R. Butts, "Frequency Spectra for the Geometric Representation of Wavefront Distortion due to Atmospheric Turbulence," *IEEE Trans. Antenna Propag.* **AP-24**, 144 (1976).
22. M. M. Colavita, M. Shao, and D. H. Staelin, "Atmospheric Phase Measurements with the Mark III Stellar Interferometer," *Appl. Opt.*, **26**, in press (1987), same issue.
23. P. A. Mandics and R. W. Lee, "On a Limitation of Multifrequency Atmospheric Probing," *Proc. IEEE* **57**, 685 (1969).
24. A. Ishimaru, "Temporal Frequency Spectra of Multifrequency Waves in Turbulent Atmosphere," *IEEE Trans. Antenna Propag.* **AP-20**, 10 (1972).
25. P. A. Mandics, J. C. Harp, R. W. Lee, and A. T. Waterman, "Multifrequency Coherences of Short-Term Fluctuations of Line-of-Sight Signals—Electromagnetic and Acoustic," *Radio Sci.* **9**, 723 (1974).
26. A. Ishimaru, *Wave Propagation and Scattering in a Random Media, Vol. 2* (Academic, New York, 1978).
27. V. P. Lukin, "Efficiency of Some Correction Systems," *Opt. Lett.* **4**, 15 (1979).
28. C. B. Hogge and R. R. Butts, "Effects of Using Different Wavelengths in Wave-Front Sensing and Correction," *J. Opt. Soc. Am.* **72**, 606 (1982).
29. J. F. Holmes and V. S. Rao Gudimetla, "Strehl's Ratio for a Two-Wavelength Continuously Deformable Optical Adaptive Transmitter," *J. Opt. Soc. Am.* **73**, 1119 (1983).
30. J. Winocur, "Dual-Wavelength Adaptive Optical Systems," *Appl. Opt.* **22**, 3711 (1983).
31. E. P. Wallner, "Comparison of Diffractive and Refractive Effects in Two-Wavelength Adaptive Transmission," *J. Opt. Soc. Am. A* **1**, 785 (1984).
32. G. D. Thayer, "Atmospheric Effects of Multiple Frequency Range Measurements," Environmental Science Service Administration, Rockville, MD, Tech. Rep. IER 56-ITSA 53 (1967).
33. M. M. Colavita, "Atmospheric Limitations of a Two-Color Astrometric Interferometer," Ph.D. Thesis, MIT, Cambridge, MA (1985).
34. R. H. Hudgin, "A New Turbulence Sensor using Atmospheric Dispersion," *Proc. Soc. Photo-Opt. Instrum. Eng.* **75**, 55 (1976).
35. M. Shao *et al.*, "The Mark III Stellar Interferometer," submitted to *Astron. Astrophys.* (1987).
36. D. Mozurkewich *et al.*, submitted to *Astron. J.* (1987).
37. W. J. Tango and R. Q. Twiss, "Michelson Stellar Interferometry," *Prog. Opt.* **17**, 239 (1980).

PRELIMINARY MEASUREMENTS OF STAR POSITIONS WITH THE MARK III STELLAR INTERFEROMETER

D. MOZURKEWICH, D. J. HUTTER,^{*)} K. J. JOHNSTON, AND R. S. SIMON
E. O. Hulburt Center for Space Research, Naval Research Laboratory, Washington, DC 20375

M. SHAO AND M. M. COLAVITA
Smithsonian Astrophysical Observatory, 60 Garden Street, Cambridge, Massachusetts 02138

D. H. STAELIN AND B. HINES
Massachusetts Institute of Technology, Cambridge, Massachusetts 02139

J. L. HERSHEY, J. A. HUGHES, AND G. H. KAPLAN
U.S. Naval Observatory, Washington, DC 20392-5100
Received 24 July 1987; revised 30 November 1987

ABSTRACT

Preliminary astrometric measurements with the Mark III optical stellar interferometer using a 12.005 m north-south baseline were made during seven nights in November 1986. A total of 22 stars were observed over large angles in a 3000-Å wide band centered at 7000 Å. As expected, the estimated precision of the relative positions increases with hour-angle coverage. For the ten stars observed over at least 90° of hour angle, the right ascensions are consistent at the 5 ms of time (1σ) level, while the uncertainties in declination are at the 22 mas (1σ) level. With this small data set, the question of systematic errors cannot be fully examined. A discussion of observational techniques, errors, limitations of this system, and future plans is presented.

I. INTRODUCTION

Determining accurate positions of stars over wide angles allows important measurements not otherwise possible. For example, fundamental constants, such as those of precession, nutation, and galactic rotation require wide-angle astrometry. Measurements at optical wavelengths are being supplanted by those made in the radio bands. Positions of extragalactic radio sources accurate to a few milliarcseconds are now available over the northern hemisphere from radio observations. A similar precision is needed in the visible, if we hope to independently align radio maps with optical images made with such systems as the *Hubble Space Telescope*, which will have a resolution of 80 mas.

Classical astrometry uses the meridian transit circle to determine the position of stars over large angles to accuracies of order 0.1 arcsec. The new FK5 optical reference frame is believed to be internally consistent at the 0.05 arcsec level at epoch 1987. The alignment of this reference frame with respect to the radio reference frame has yet to be determined. We believe that the radio reference frame is probably internally consistent at the level of a few milliarcseconds (Johnston and DeVegt 1986; Ma *et al.* 1986).

Modern techniques are evolving that promise improved accuracy in determining star positions. Space techniques such as the *HIPPARCOS* satellite promise a reference frame of stars down to magnitude 10 with accuracies of a few milliarcseconds. As space techniques are very costly and deployment in orbit is uncertain at this time, the development of ground-based techniques is very important. Initial measurements with an interferometer at Mount Wilson Observatory gave stellar positions accurate to 3 arcsec (Shao *et al.* 1987). A new-generation instrument, the Mark III stellar interferometer, is in the process of fabrication. Here we re-

port preliminary measurements with that instrument using the initial 12 m north-south baseline.

Further, interferometry appears to be a technology that offers improved accuracy for both ground and space observations. Before space-based observations are planned in detail using this technique, experience must be gained through the development of ground-based systems.

II. THE INSTRUMENT

The Mark III interferometer is the third in a series of optical interferometers built on Mount Wilson, California. Stellar fringes were first tracked with this instrument in September 1986. By November, the system was operating well enough to allow stellar observations to continue all night. This instrument was specifically built to do fundamental astrometry. Several features were incorporated into its design to allow it to accomplish this goal. The fringes were tracked in a closed-loop mode, to allow accurate measurement of the delay. Star tracking and fringe tracking were completely automated, allowing rapid switching between stars. One hundred sixty observations were accomplished during one night. The light from the siderostats was mixed in a central, temperature-controlled building, and the siderostats were mounted on massive concrete piers. As a result, the baseline is fairly stable at the micron level. Other features designed and built, but not yet operational, are expected to further improve the performance of the system. We will limit our description of the instrument to the points relevant to the astrometric performance. A full description of the instrument is given in Shao *et al.* (1988).

The interferometer consists of two 25-cm-diameter siderostats, mounted on massive, insulated concrete piers and currently operating with a north-south baseline of 12.005 m. Four additional piers have been constructed, allowing future observations with a 20 m north-south baseline, as well as with two oblique baselines. From the siderostats, the light

^{*)} Also Applied Research Corporation, Landover, MD.

passes through evacuated tubes into a central, temperature-controlled building. The light from each siderostat is directed into delay lines containing movable retroreflectors. Next, the light is combined at a beam combiner and the resulting fringes are detected with a photomultiplier tube using the technique described below. For the observations discussed here, the clear aperture was less than 2 in. and light from only one side of the beam combiner was detected. To maintain parallel wavefronts at the beam combiner, light from an annulus surrounding the central aperture was deflected into a star tracker which adjusts the angles of two flat mirrors. All of the optical hardware in the central building is on a superinvar table except the delay lines. However, the positions of the retroreflectors in the delay lines are measured relative to the superinvar table with a laser metrology system.

To detect fringes, the length of the delay line is dithered in a 500 Hz triangle wave with an amplitude of one optical wavelength. The 'stroke' is divided into four equal segments. The number of photons observed in each of the segments is used to determine the position of the fringe for real-time tracking. A wide-bandpass filter was used to increase the sensitivity and to decrease the contrast of all but the central fringe. Four milliseconds of data are coherently combined. This time constant was chosen to be short relative to the time constant of the atmosphere, so that atmospheric turbulence is frozen during a measurement.

III. DATA

The nightly observing procedure consisted of cycling through a list of stars. Each observation consisted of tracking the central fringe on one star for 100 s after the fringe position was found. During periods of poor seeing or at large zenith angles, the fringe tracker would occasionally lose the fringe and take several seconds to reacquire it. During good seeing, the fringe tracker would successfully track a fringe

for several minutes. As many as 160 observations were possible during a single night.

In reducing the data, an observation was first averaged to 1 s. These 1 s delays were averaged by differencing the observed and predicted delays and adding the mean difference to the predicted delay at the mean time. If an observation consisted of fewer than ten 1 s averages, it was discarded. The data were not edited in any other way. A plot of the observed delays as a function of time is shown for a typical night in Fig. 1. The large dots are the 100 s averages. Multiple observations of the same star are connected with small dots.

All of the astrometric information is contained in the observed delay. It is related to the star's position through

$$d = C_0 + \bar{B} \cdot \bar{S}, \quad (1)$$

where B is the baseline vector, S is a unit vector pointing in the unrefracted direction of the star, and C_0 is a constant which depends on the length of the optical path inside the central building and on the differential atmospheric path length between the receiving apertures. Note that for a horizontal baseline with a vacuum delay line, the air path is nearly identical for both arms of the interferometer, causing the effects of atmospheric refraction to cancel out (see the Appendix). We adopt the convention of measuring the delay as a length. Expanding this in a right-handed coordinate system, with Z axis parallel to the Earth's axis, and Y axis toward the east point on the horizon, gives

$$d = C_0 + B_z \sin(\delta) - B_y \cos(\delta) \sin(h) + B_x \cos(\delta) \cos(h), \quad (2)$$

where $h = t - \alpha$ is the instantaneous hour angle, t is the local sidereal time, and δ is the declination. As the coordinate frame depends upon the rotation of the Earth, the declinations are with respect to the instantaneous celestial pole while the right ascension zero point is arbitrary. Observa-

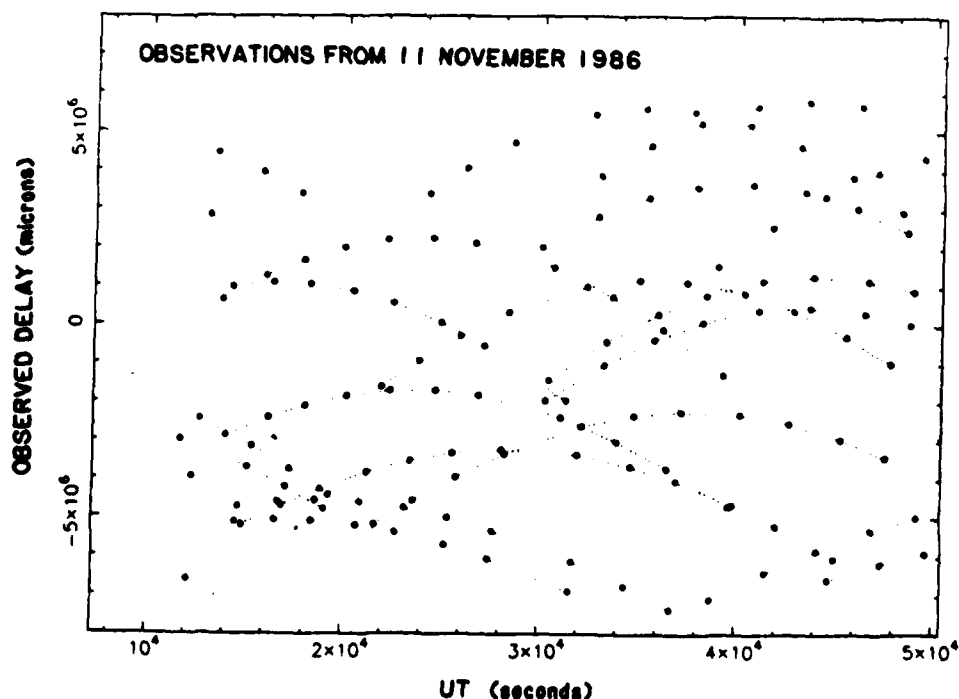


FIG. 1. Observed delay (in microns) versus universal time (seconds) on 5 November 1986. Note that each large dot is the mean of a 100 s integration. Small dots connect observations of the same star.

tions of the delay of a star as a function of time provide three independent measurements, the amplitude and phase of a sinusoid and a constant offset. A zero point for right ascension cannot be determined from these observations since there is no tie to either the ecliptic or to a well-defined local longitude reference. Observation of N stars at various declinations can be described by specifying $2N + 3$ parameters, the three components of the baseline, the delay constant, N declinations, and $N - 1$ right ascensions. With three independent measurements each, at least three stars must be observed to determine all of the parameters. In practice, this solution is not well constrained. Expanding Eq. (2) in terms of assumed baseline components and star position plus small corrections,

$$\begin{aligned}
 d_{\text{res}} &= d - C_0 - B_x \sin(\delta) + B_y \cos(\delta) \sin(h) \\
 &\quad - B_z \cos(\delta) \cos(h) \\
 &= \Delta C_0 + \Delta B_x \sin(\delta) + \Delta \delta B_z \cos(\delta) \\
 &\quad + \sin(h) [-\Delta B_y \cos(\delta) + \Delta \delta B_y \sin(\delta) \\
 &\quad + \Delta \alpha B_x \cos(\delta)] \\
 &\quad + \cos(h) [\Delta B_x \cos(\delta) + \Delta \alpha B_y \cos(\delta) \\
 &\quad - \Delta \delta B_x \sin(\delta)], \quad (3)
 \end{aligned}$$

where δ and h are now the assumed declination and hour

angle. Since $B_x \sim 6.8$ m and $B_z \sim 10$ m and $B_y \sim 3$ cm, the residuals are dominated by the B_x and B_z terms. If we want to determine equally good values for $\Delta \delta$ and $\Delta \alpha$, the coefficients of $\sin(h)$ and $\cos(h)$ must be determined to the same precision. With 6 hr of coverage, centered on transit, $\cos(h)$ changes by only ± 0.15 , whereas $\sin(h)$ varies by ± 0.7 . The $\cos(h)$ term can be separated from the constant term with only about one-fifth of the precision of the other terms. If the baseline or the delay varies slowly with time, more parameters must be added to the fit, further hindering their determination.

We used a two-step procedure to determine star positions from the observed delay. First, we solved for the baseline using *a priori* estimates of the star positions. Then we used the residual delays from this fit to determine improved star positions. Since we used *a priori* star positions to determine the baseline, the improved star positions are not absolute, but are relative to a mean position of the stars in the fit.

For the baseline fit, we used star positions taken from the FK5 catalog, transformed to apparent topocentric place of date in accordance with recent IAU resolutions (see Kaplan 1981). For the two binaries in our sample, the positions in the catalog correspond to the center of mass of the systems. We used the orbital positions determined by Worley (private communication) to determine the positions of the primaries. The parameters used are shown in Table I. In addition, the differential optical path length through the atmosphere was

TABLE I. Astrometric parameters for the observed stars.

Name	RA	DEC	μ_α	μ_δ	π	RV
	J2000.0	J2000.0	s/cen	" / cen	"	km/s
α And	00:08:23.265	29:05:25.58	1.039	-16.33	0.0240	-12
β Cas	00:09:10.695	59:08:59.18	6.827	-18.09	0.0720	11
α Cas	00:40:30.450	56:32:14.46	0.636	-3.19	0.0160	-4
γ_1 And	02:03:53.963	42:19:46.99	0.404	-5.17	0.0130	-12
α^1 Ari	02:07:10.403	23:27:44.66	1.383	-14.83	0.0430	-14
α Per	03:24:19.365	49:51:40.34	0.246	-2.46	0.0290	-2
γ Ori	05:25:07.857	6:20:58.74	-0.059	-1.39	0.0260	18
β Tau	05:26:17.511	28:36:26.67	0.169	-17.51	0.0180	9
β Aur	05:59:31.720	44:56:50.78	-0.541	0.03	0.0370	-18
γ Gem	06:37:42.725	16:23:57.43	0.293	-4.16	0.0310	-13
α Gem ^a	07:34:35.997	31:53:18.53	-1.347	-9.87	0.0720	-1
α CMi ^a	07:39:18.113	5:13:30.06	-4.755	-102.29	0.2880	-3
β Gem	07:45:18.946	28:01:34.26	-4.740	-4.59	0.0930	3
α Leo	10:08:22.315	11:58:01.89	-1.693	0.64	0.0390	6
β UMa	11:01:50.482	56:22:56.65	0.988	3.4	0.0420	-12
α UMa	11:03:43.666	61:45:03.22	-1.675	-6.65	0.0310	-9
γ Dra	17:56:36.367	51:29:20.21	-0.081	-1.94	0.0170	-28
α Lyr	18:36:56.332	38:47:01.17	1.726	28.61	0.1230	-14
α Aql	19:50:47.002	8:52:06.03	3.629	38.63	0.1981	-26.3
γ Cyg	20:22:13.704	40:15:24.14	0.035	0.03	0.0030	-8
α Cyg	20:41:25.917	45:16:49.31	0.027	0.23	0.	-5
ϵ Per	21:44:11.164	9:52:29.92	0.207	-0.06	0.0060	5

^a Position is for the center of mass of the binary system. To find the position of the observed star at the time of the observations add to α Gem $\Delta\alpha = -0.^{\circ}0793$ and $\Delta\delta = -0.^{\circ}158$ and to α CMi $\Delta\alpha = -0.^{\circ}0085$ and $\Delta\delta = -1.^{\circ}378$

estimated and removed from the data. A pivot-point correction to account for the siderostat geometry was tested but not included, since it had no significant effect on the results. The form and magnitude of these corrections are discussed in the Appendix.

Effectively, then, the baseline was determined relative to the FK5 system. The baseline was not constant, but drifted slowly during the observations. On four nights during the fall of 1986, a laser interferometer was operated in a vacuum tube between one of the unused piers and the central building, although not connected to the superinvar table. These data were taken before some of the final improvements were made to the system and may not be relevant to the stellar observations. Nevertheless, there were large variations in the path length for the first few hours after sunset. Later in the night, the length drifted by about $1 \mu\text{m}$ per hour. A constant drift rate provides an acceptable fit (less than $1 \mu\text{m}$ residuals) to the data later in the night. The large variations in the early evening are almost certainly due to large temperature changes that occur at sunset and should take place prior to the start of our observations in November. Therefore, we assumed that the delay constant and the components of the baseline varied linearly during the stellar observations. In Eq. (2), C_0 was replaced with $C_0 + C_1 t$, B_x with $B_{0x} + B_{1x} t$, etc.

There are two major sources of noise: variations in the baseline and atmospheric turbulence. (1) Noise due to baseline variations is caused by effects such as thermal drift, bearing errors, and flexure, and will occur over periods of hours or when comparing observations taken in different parts of the sky. (2) The atmospheric effects include both fluctuations about the mean delay and a systematic offset. The small offset occurs because the path length through the atmosphere is slightly different for the two siderostats. With a north-south baseline, this offset is mainly a function of declination. It has been estimated and removed using the procedure outlined in the Appendix. The fluctuations have an amplitude of as much as $15 \mu\text{m}$ at a frequency of a few tenths of a Hertz. Using data taken with this interferometer, Colavita *et al.* (1987) have shown that the power spectrum of these fluctuations goes as $f^{-2/3}$. Since this is close to $1/f$ noise, we assumed that the uncertainty of a 100 s average due to atmospheric turbulence was the rms width of the distribution of 1 s averages about the mean value. This is not strictly correct, since the noise should integrate down as the sixth root of the integration time. Thus the noise estimate used is roughly a factor of 2 larger than the noise expected from the atmosphere alone. A histogram of these values is presented in Fig. 2.

The baseline parameters were determined separately for each night's data using standard linear-regression analysis. In weighting the data, we assumed that the atmosphere contributed all of the noise. A plot of the residual delays as a function of time is shown in Fig. 3. The derived parameters were collected in Table II. The observing times, number of observations, mean uncertainties of the observations, and the rms and χ^2 of the fits are collected in Table III. The standard deviation of the residual delays varies from $4.6 \mu\text{m}$ on 14 November to $7.7 \mu\text{m}$ on 11 November. When data from all seven nights are combined, the standard deviation of the residuals is $6.5 \mu\text{m}$. The days with the largest systematic variations in the residuals (5 November, 10 November) are also days with large values of the reduced χ^2 . On four of the nights, the reduced χ^2 is less than 1.2, and the rms of the residuals after the fit is less than the mean uncertainty of the

HISTOGRAM OF ESTIMATED UNCERTAINTIES

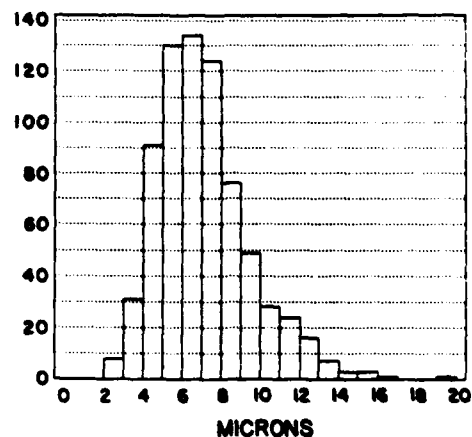


FIG. 2. Histogram of the assumed uncertainty (in microns) of the observations of all data from November 1986. The observations are 100 s in length, short enough to be dominated by atmospheric fluctuations. The data were averaged to 1 s before determining the rms. A change in declination of 1 arcsec corresponds to a change in delay of roughly $55 \mu\text{m}$.

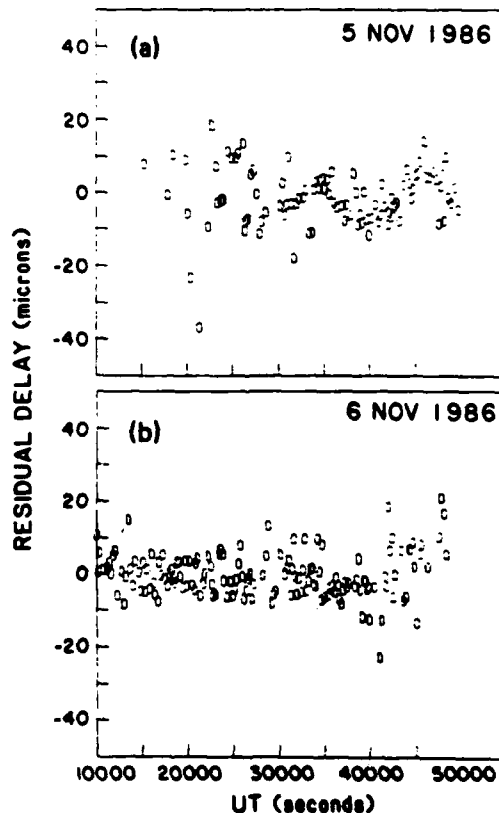


FIG. 3. Residual delay versus time. (a) 5 November 1986; (b) 6 November 1986. Note that the observations obtained on 5 November have systematic effects of $5\text{--}10 \mu\text{m}$ peak-to-peak.

TABLE II. Derived baseline parameters.

Date	C_0	B_x microns	B_y	B_z	C_1	B_{1x} microns/hour	B_{1y}	B_{1z}
5 Nov	-20782.2±16.4	6752705.1±15.5	31362.0± 5.7	-9926026.4±12.9	4.89± 2.7	-3.0± 2.5	1.3± 0.9	-5.9± 2.1
6 Nov	-20758.0± 5.6	6752697.2± 5.2	31365.3± 1.7	-9926050.4± 4.5	-1.71± 1.8	-1.6± 1.7	1.6± 0.6	-1.9± 1.5
9 Nov	-20788.5±28.7	6752716.6±27.9	31364.3± 8.5	-9926052.4±20.3	3.39± 4.0	-3.0± 3.9	2.6± 1.2	-5.2± 2.8
10 Nov	-20764.0± 6.8	6752707.9± 6.8	31371.4± 1.9	-9926082.3± 5.8	-3.28± 1.8	-1.8± 1.7	3.1± 0.5	-2.6± 1.5
11 Nov	-20778.4± 9.6	6752699.5± 9.4	31386.6± 2.7	-9926084.3± 7.4	2.18± 2.0	-1.1± 1.9	0.0± 0.6	-3.2± 1.6
12 Nov	-19938.8±11.2	6752692.5±10.7	31369.8± 3.5	-9926082.4± 8.5	2.44± 2.5	-0.7± 2.3	1.0± 0.8	-1.6± 2.0
14 Nov	-20643.9±43.5	6752738.1±40.4	31359.7±17.8	-9926027.2±32.7	10.36± 5.2	-5.9± 4.8	3.0± 1.9	-11.5± 3.8

data points. On these nights, the estimate of the uncertainties seems to be valid. However, recall that it is about a factor of 2 larger than that expected from the atmosphere. On the three remaining nights, the χ^2 is greater than 1.5 and the rms of the residuals is greater than the mean of the uncertainties. Two of these nights show large systematic shifts in a plot of the residual versus time (Fig. 3). These are three of the longest nights, but if data from half the night is deleted from the fit, the χ^2 is improved, but not to the level of the four good nights. Thus, on at least these three nights, we seem to be limited by a source of noise other than the atmosphere, presumably thermal or mechanical drifts of the baseline.

If data from all of the stars are combined, there is no systematic variation of the residual delay with hour angle. However, plots of individual stars (Fig. 4) show such trends. This implies that the fit could be improved by solving for corrections to the star positions.

Equation (3) was used to determine corrections to the star positions, assuming the fitted baseline was correct. Errors in the baseline estimate, caused by motions of the baseline more complicated than a linear drift, or by using incorrect star positions in the previous step, couple directly into the estimates of star positions. This two-step fitting does not allow absolute astrometry, but star positions are determined relative to the mean of the stars included in the fit. Again, a standard linear regression was used and the weighting was based on the estimate of the atmospheric noise. Star posi-

tions, relative to the assumed positions, determined from each night's data, as well as from a global fit to all of the data, are collected in Tables IV and V. The stars are arranged in order of increasing right ascension. Stars at the beginning and end of the list were only observed near setting, or rising, respectively, and on some nights have very few observations. If less than three observations were made of a star during a night, a fit position for that star was not included in the tables, although those observations were used for fitting the baseline and for the fit to all seven nights' data.

To determine at what level the data are self-consistent, χ^2 tests were performed on the positions in Tables IV and V. The fit to all seven nights' data was taken as the mean position. The positions and errors determined from each night were taken as the data points. There was one fit parameter for each star in the table. The reduced χ^2 came out to be 1.08 for the right ascensions and 0.97 for the declinations, with 91 degrees of freedom. Thus, the data are consistent with the (1σ) errors tabulated. That is, the formal errors from the least-squares fit are a good estimate of the precision (night-to-night repeatability) of the system.

Positions determined for stars observed only near rising or setting have very large errors. However, the errors are smaller for stars with total hour-angle coverage of at least 90° . These ten stars have a mean error in declination of 22 mas (1σ) and in right ascensions 5 ms of time using seven nights of data. We stress that these numbers show the preci-

TABLE III. Summary of observations.

Date	no. of obs.	rms μ m	σ μ m	χ^2	obs time hours
5 Nov	98	6.8	6.5	1.64	9.58
6 Nov	152	5.6	6.9	0.96	10.85
9 Nov	77	5.1	5.8	1.20	7.42
10 Nov	142	7.3	7.0	1.53	10.90
11 Nov	144	7.7	7.3	1.62	10.57
12 Nov	94	7.4	9.0	0.98	6.40
14 Nov	68	4.6	6.2	0.84	5.40
All	819	6.5	7.1	1.28	61.12

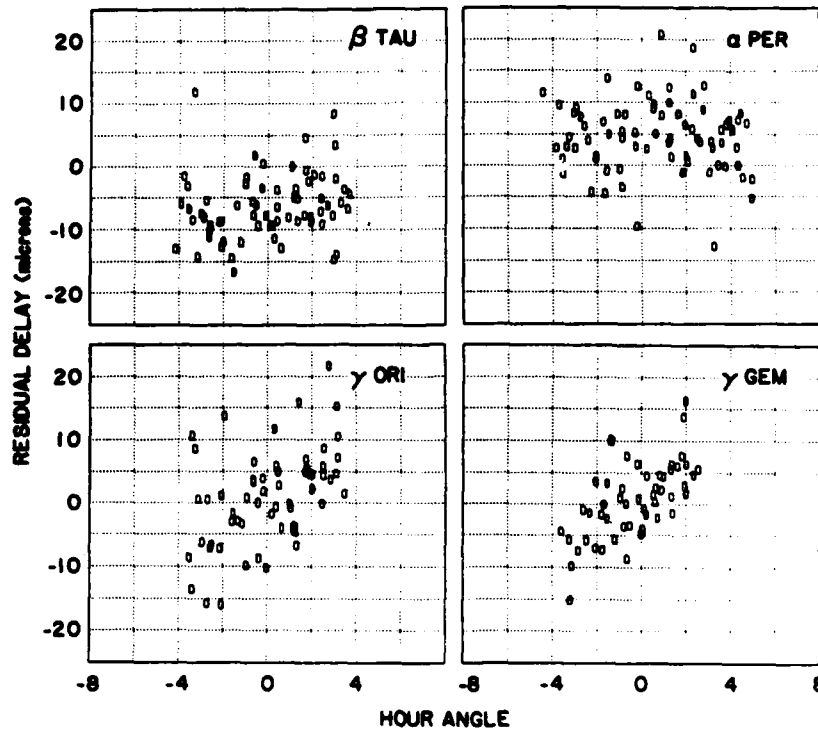


FIG. 4. Residual delays for individual stars versus hour angle. (a) β Tau, (b) α Per, (c) γ Ori, (d) γ Gem. These four stars show the largest systematic trends in the data. For our observing geometry, errors in declination correspond to an offset while errors in right ascension correspond to a nonzero slope. Note that the assumed positions for β Tau and α Per are off in declination, while the positions for γ Ori and γ Gem are off in right ascension.

TABLE IV. Derived corrections to right ascensions for observed stars in seconds of time.

star	5 Nov	6 Nov	9 Nov	10 Nov	11 Nov	12 Nov	14 Nov	mean
α And	-.0800 \pm .1714	.0081 \pm .0110	...	-.0045 \pm .0174	-.0221 \pm .0204	-.0002 \pm .0085
β Cas	-.1298 \pm .0816	.0134 \pm .0214	...	-.0208 \pm .0341	.0937 \pm .0593	.3318 \pm .52240056 \pm .0169
α Cas	-.0053 \pm .0420	-.0281 \pm .0183	-.0334 \pm .0670	-.0193 \pm .0290	-.0163 \pm .0327	-.1087 \pm .1538	...	-.0231 \pm .0129
γ Gem	.0291 \pm .0250	-.0034 \pm .0091	-.1247 \pm .0892	-.0015 \pm .0105	.0204 \pm .0131	.0028 \pm .0415	-.3185 \pm .8692	.0031 \pm .0058
α Ari	-.0201 \pm .0191	.0011 \pm .0084	-.0072 \pm .0524	.0027 \pm .0065	.0055 \pm .0086	.0460 \pm .03540024 \pm .0042
α Per	-.0053 \pm .0160	-.0110 \pm .0113	.0092 \pm .0246	-.0134 \pm .0108	-.0155 \pm .0115	-.0229 \pm .0306	-.0342 \pm .0458	-.0105 \pm .0057
γ Ori	-.0083 \pm .0092	.0242 \pm .0140	.0069 \pm .0091	.0400 \pm .0102	.0090 \pm .0081	-.0040 \pm .0143	.0203 \pm .0194	.0108 \pm .0040
β Tau	.0106 \pm .0098	.0097 \pm .0108	.0196 \pm .0092	.0131 \pm .0088	.0055 \pm .0381	.0193 \pm .0133	.0195 \pm .0171	.0125 \pm .0038
β Aur	.0009 \pm .0106	.0071 \pm .0105	.0067 \pm .0111	.0044 \pm .0102	-.0018 \pm .0115	.0033 \pm .0160	.0287 \pm .0174	.0052 \pm .0044
γ Gem	.0128 \pm .0106	.0354 \pm .0156	.0069 \pm .0130	.0002 \pm .0120	.0185 \pm .0090	.0147 \pm .0135	.0030 \pm .0130	.0126 \pm .0044
α Gem	-.0854 \pm .0142	-.0834 \pm .0204	-.0941 \pm .0145	-.0624 \pm .0128	-.0833 \pm .0092	-.0793 \pm .0161	-.1180 \pm .0213	-.0831 \pm .0052
α Chi	.0176 \pm .0118	.0051 \pm .0185	-.0129 \pm .0124	.0285 \pm .0158	.0143 \pm .0216	.0243 \pm .0174	-.0001 \pm .0116	.0084 \pm .0054
β Gem	.0310 \pm .0128	-.0053 \pm .0179	.0037 \pm .0135	.0033 \pm .0125	.0060 \pm .0101	.0050 \pm .0147	.0169 \pm .0144	.0093 \pm .0049
α Leo	.0233 \pm .0342	.0608 \pm .0824	-.0095 \pm .0237	-.0615 \pm .0382	.0075 \pm .0257	.0904 \pm .0840	.0034 \pm .0321	-.0003 \pm .0128
β UMa	-.0021 \pm .0193	...	-.0142 \pm .0241	-.0164 \pm .0284	.0561 \pm .0250	.0121 \pm .0276	.0266 \pm .0256	.0095 \pm .0099
α UMa0674 \pm .04740674 \pm .0474
γ Dra	...	-.2328 \pm .3883	-.2328 \pm .3883
α Lyr0312 \pm .20990274 \pm .40140303 \pm .1860
α Aql0366 \pm .0774	...	-.1512 \pm .1512	-.0023 \pm .0688
γ Cyg	...	-.0210 \pm .0361	...	-.1703 \pm .0657	.1774 \pm .1799	-.0486 \pm .0311
ϵ Cyg	...	-.0418 \pm .0397	...	-.0780 \pm .0565	.3698 \pm .1072	-.0182 \pm .0310
ϵ Per0027 \pm .0198	...	-.0844 \pm .0978	.0727 \pm .12140010 \pm .0191

TABLE V. Derived corrections to declinations for observed stars in seconds of arc.

star	5 Nov	6 Nov	9 Nov	10 Nov	11 Nov	12 Nov	14 Nov	mean
α And	-0.665±0.639	0.084±0.051	...	-0.089±0.095	-0.096±0.095	0.017±0.040
β Cas	-0.446±0.357	0.121±0.084	...	0.026±0.131	0.187±0.171	1.666±2.323	...	0.089±0.064
α Cas	-0.004±0.181	-0.138±0.071	-0.047±0.291	0.095±0.108	-0.139±0.133	-0.394±0.647	0.339±5.861	-0.074±0.050
γ Gem	0.175±0.113	0.030±0.047	-0.659±0.466	0.031±0.051	0.077±0.062	0.106±0.193	-1.695±5.301	0.048±0.028
α Ari	-0.084±0.090	0.057±0.039	0.023±0.260	-0.001±0.034	0.040±0.047	0.091±0.182	...	0.022±0.021
α Per	-0.110±0.077	-0.181±0.055	-0.040±0.114	-0.130±0.069	-0.200±0.059	-0.210±0.128	-0.208±0.192	-0.159±0.029
γ Ori	-0.057±0.046	-0.011±0.064	-0.023±0.045	0.081±0.044	-0.022±0.037	-0.084±0.063	0.021±0.065	-0.010±0.018
β Tau	0.166±0.040	0.151±0.057	0.210±0.042	0.106±0.045	0.129±0.042	0.156±0.061	0.200±0.073	0.157±0.018
β Aur	0.006±0.055	-0.064±0.073	-0.074±0.047	-0.016±0.071	0.040±0.052	-0.013±0.071	0.009±0.067	-0.016±0.022
γ Gem	0.003±0.045	-0.048±0.069	-0.030±0.036	-0.048±0.047	-0.031±0.046	-0.005±0.061	-0.069±0.051	-0.031±0.018
α Gem	-0.028±0.047	-0.019±0.119	-0.035±0.048	-0.080±0.069	-0.083±0.042	0.065±0.072	-0.131±0.061	-0.051±0.021
α Chi	-0.083±0.045	-0.069±0.084	-0.039±0.040	-0.056±0.072	-0.041±0.086	0.010±0.067	-0.026±0.040	-0.043±0.020
β Gem	-0.013±0.051	0.069±0.138	-0.006±0.048	0.006±0.075	0.009±0.059	0.031±0.064	-0.069±0.048	-0.011±0.022
α Leo	-0.048±0.216	-0.509±0.616	0.141±0.156	0.440±0.253	0.067±0.126	-0.506±0.568	0.057±0.156	0.081±0.073
β UMa	-0.141±0.446	...	0.759±0.570	0.849±1.342	-0.415±0.409	-0.867±1.295	-0.395±0.302	-0.199±0.195
α UMa	-0.695±0.739	-0.695±0.739
γ Dra	...	-1.266±1.996	-1.266±1.996
α Lyr	...	0.332±1.160	...	0.178±2.396	0.302±1.044
α Aql	...	-0.031±0.642	...	-1.329±1.051	-0.226±0.408
γ Cyg	...	-0.097±0.183	...	-0.944±0.338	0.861±0.969	-0.257±0.158
α Cyg	...	-0.229±0.163	...	-0.327±0.282	1.969±0.480	-0.077±0.135
ϵ Per	...	-0.012±0.090	...	-0.378±0.537	0.122±0.654	-0.019±0.087

sion of the measurements and not the absolute accuracy. Larger systematic errors may still be present in the data.

Figure 5 shows the difference between the observed and the FK5 star positions at the epoch of observation for the ten stars with extensive hour-angle coverage. The error bars are 1 standard deviation. Declinations for two stars deviate significantly from the assumed positions (more than 5 standard deviations). The most significant deviation in right ascension is 3 standard deviations. These deviations are larger than expected, given our noise estimates. The χ^2 is 1.8 per degree of freedom for the right ascensions and 2.6 for the declinations. If we assume that the rms errors in the FK5

catalog at epoch 1987 average around 0^h00^m5 in right ascension and 0^h04^m0 in declination, and add these errors quadratically to our formal errors, then the χ^2 is 1 per degree of freedom, as expected for Gaussian noise. Alternatively, the FK5 catalog may be more accurate than this if there are systematic errors in our data.

If there is flexure in the siderostat systems, or if the differential atmospheric delay was not properly estimated, there may be a systematic error in the star positions as a function of declination. The data are plotted in Fig. 6. There is no apparent systematic trend in the plot.

IV. FUTURE PLANS

The accuracy of our measurements of star positions is limited by three effects. The observed delay contains an additional term proportional to the index of refraction of the

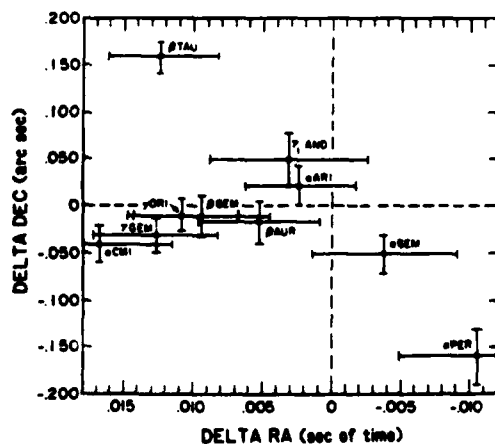


FIG. 5. Difference between the fit position and the FK5 position for the observed stars with the corresponding (1 σ) errors. The uncertainties in right ascension are roughly five times larger than the uncertainties in declination because we used a north-south baseline. A large east-west component will decrease the errors in right ascension.

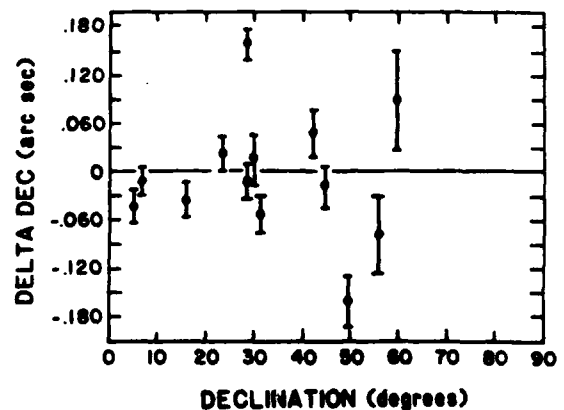


FIG. 6. Errors in declination versus declination. There are no systematic effects present in this small data set.

atmosphere. Turbulence produces changes in the index of refraction, which in turn causes the atmospheric delay to wander about the expected value. The expected value has been estimated and removed, but the fluctuations limit our ability to estimate the observed delay. This noise is $f^{-2/3}$, which implies that the signal-to-noise increases as the sixth root of the integration time. Second, errors in the estimate of the baseline produce a residual delay which is then interpreted as an error in the calculated star positions. The baseline errors are dominated by rapid drifts, due to effects such as imperfect ball bearings in the siderostats, flexure, and the pivot-point correction, as well as slower, thermal drifts. Finally, correlations in the fit parameters can cause the wrong baseline to be fit to the data, with resulting errors in the derived star positions.

Four major improvements will be incorporated into this system during 1987. Each of them should have a significant effect on the sources of noise discussed above.

First, observations will be performed in two colors simultaneously. After the light from the two siderostats is combined, it passes through a dichroic mirror. This directs the blue light and red light into separate photomultiplier tubes. Because the atmosphere is a dispersive medium, the atmospheric delay is different in red and blue light, with the difference proportional to the atmospheric delay in either color alone. Thus, by measuring this difference, and either measuring or assuming the dispersion, the effects of the atmosphere can be greatly reduced. Some preliminary two-color data have already been taken. Colavita *et al.* (1987) estimate that two-color observations should produce, roughly, a factor of 5 decrease in the atmospheric noise.

Second, a more extensive laser metrology system will measure the position of each siderostat mirror relative to the concrete piers on which they are mounted. Changes in the baseline due to motion of the siderostats, imperfect ball bearings, and thermal motions of the siderostats will be measured and corrected. However, drifts due to changing separation of the piers will still have to be estimated from the data. In addition, an internal light source and retroreflectors mounted on the siderostat mirrors will provide a direct measurement of the delay constant up to 20 times each night. These measurements should reduce the systematic variations seen in the residual delays. However, the metrology system imposes limits on siderostat motion which will restrict sky coverage.

Third, an additional baseline with a substantial E-W component will soon be in operation. Switching between baselines will take only a few minutes and will be possible roughly once each hour during observing. This should reduce the correlations between the parameters, allowing the determination of absolute declinations.

Finally, a more sophisticated star tracker will be installed, allowing observations of objects 2-4 mag fainter than our current third-magnitude limit. This will allow more stars to be observed and hence a better determination of the baseline.

Shao *et al.* (1987) used the Mark II optical interferometer with a 3.1 m baseline and achieved a precision of 3 arcsec. They estimated that the precision could be improved by a factor of 300 by improving the mechanical and thermal stability of the system and by monitoring the siderostat positions with a laser metrology system. In this paper, we show a factor of 100 improvement over the Mark II system and have not yet incorporated the laser metrology system. Since the noise in our data is still a factor of 2 larger than that expected

from the atmosphere, measurement of the siderostat positions should improve the data by a similar factor.

V. SUMMARY

Preliminary astrometric data from a white-light fringe-tracking optical interferometer have been presented. After fitting a baseline to the data, the residual delays were $6.5 \mu\text{m}$ rms. The noise was still two to three times that expected from the atmosphere and was probably dominated by mechanical roughness and thermal drifts. The residual delays were used to determine new positions for the observed stars. The data demonstrate that relative astrometry can be performed with a precision of better than 22 mas in declination and 5 ms of time in right ascension. The agreement with the FK5 positions is reasonable considering the accuracy of the FK5 catalog and the limitations of our small data set.

APPENDIX

a) Correction for the Atmosphere

Since the index of refraction of air is greater than 1, the optical path length differs from the geometric path length. We determined this difference (1.89 m) for a star at the zenith by integrating the index of refraction as a function of altitude. We used a standard model atmosphere starting at the altitude of Mount Wilson and the standard dependence of the index of refraction on temperature and density. For a plane-parallel atmosphere, possible on a flat Earth without weather, this effect is identical for each siderostat, and the atmosphere has no systematic effect on the observed delay. However, pressure gradients along the baseline will result in index-of-refraction gradients and the correction to the delay will be different for the two siderostats. This effect is small enough to ignore. Making the standard assumption that the pressure gradient balances the Coriolis force, a 10 m/s wind perpendicular to the baseline translates into a change of optical path length of $0.25 \mu\text{m}$. A more important effect is due to the curvature of the Earth. The zenith direction differs for the two siderostats. This angle is 0.4° for a 12 m baseline. The difference in zenith angle to the star can be, at most, this much. We assume a plane-parallel atmosphere at each siderostat and write the correction to the delay as

$$\Delta d = 1.89 \times 10^6 [\sec(z_1) - \sec(z_2)], \quad (\text{A1})$$

where z_1 and z_2 are the zenith angle of the star as viewed from the two siderostats and Δd is in microns. For a north-south baseline, this effect is mainly a function of declination. However, if we change the delay constant and the Z component of the baseline, residual delays are produced which mimic Eq. (A1). Figure 7 shows the residual delays due to the atmosphere (dashed lines) as well as the residuals for $\Delta D_0 = 3.0 \mu\text{m}$ and $\Delta B_z = -5.53 \mu\text{m}$ (solid lines). The fit is much better than $1 \mu\text{m}$ for all parts of the sky.

b) Pivot-Point Correction

In a non-ideal siderostat, the two axes will not intersect and neither will be in the surface of the mirror. Thus the mirror will translate as well as rotate when moving between stars in different parts of the sky. The change in baseline due to this motion can be written as

$$\delta B = E + A \cos(\phi_E), \quad (\text{A2})$$

where E is the distance of the center of the mirror from the elevation axis, A is the separation of the two axes and ϕ_E is

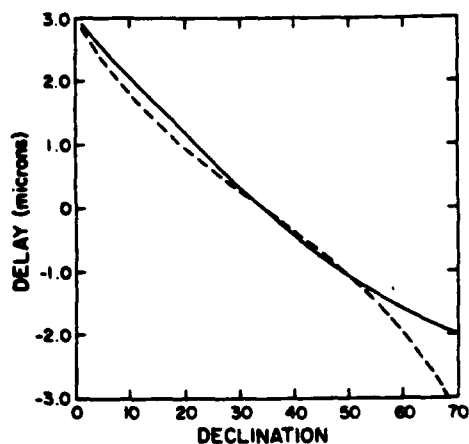


FIG. 7. The dashed line is the atmospheric correction, in microns, as a function of declination. For a north-south baseline, the correction is almost independent of hour angle. The solid line is the change in delay for $\Delta C_0 = 3.0 \mu\text{m}$ and $\Delta B_1 = -5.53 \mu\text{m}$. Note that if the atmospheric correction were not included, the residual delay due to the atmosphere would be fit to within a micron by a change in the baseline. The star positions determined from the data would not be affected.

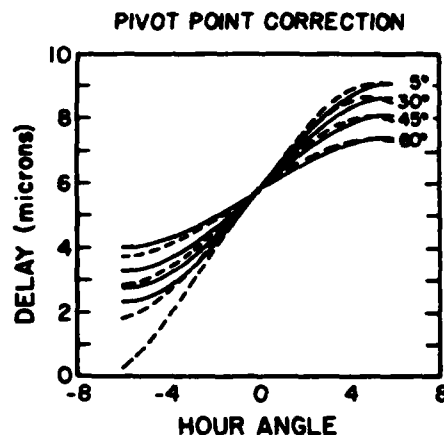


FIG. 8. The dashed lines show the size of the pivot-point correction as a function of hour angle for four selected declinations. The solid lines show the change in delay for the same declinations and a change in the baseline of $\Delta B_1 = -3.4 \mu\text{m}$ and $\Delta C_0 = 5.7 \mu\text{m}$. Again, the errors in the residual delay caused by not including the pivot-point correction are less than a micron for all parts of the sky we observed.

the rotation of the elevation axis. The azimuth (fixed) axis of each siderostat is pointed toward the west and 15° above the horizon. Since the orientations of the siderostats are almost identical, we can write the change in delay as

$$\begin{aligned} \delta d &= (\delta B_1 - \delta B_2) (\bar{M} \cdot \bar{S} + \bar{M} \cdot \bar{F}) \\ &= 2(\delta B_1 - \delta B_2) \bar{M} \cdot \bar{S}, \end{aligned} \quad (A3)$$

where the subscripts refer to the two siderostats and \bar{M} , \bar{S} , and \bar{F} are unit vectors normal to the siderostats and toward the star and feed mirror, respectively. For identical siderostats, the correction vanishes. After installing plastic shims, A and E were measured for the two siderostats. They were $A_S = -91.1 \mu\text{m}$, $A_N = -92.3 \mu\text{m}$, $E_S = -3.4 \mu\text{m}$, and E_N

$= +1.3 \mu\text{m}$, where the subscripts refer to the south and north siderostats. For these values, the correction is shown as the dashed lines in Fig. 8. The solid lines show the change in delay corresponding to a change in the baseline ($\Delta B_1 = -3.4 \mu\text{m}$ and $\Delta D_0 = 5.7 \mu\text{m}$). Except for more than 4 hr to the east at low declinations, the pivot-point correction mimics the residual delay from the baseline change. If either atmospheric or pivot-point corrections are not applied, the baseline parameters will not correspond to the geometric baseline, but the star positions will not be affected. When the pivot-point corrections were applied to the data, the residuals did not decrease. Since we are not sure of the stability of the offsets at the micron level, we decided not to include the corrections in the final fit.

REFERENCES

- Colavita, M. M., Shao, M., and Staelin, D. H. (1987). *Appl. Opt.* **26**, 4106.
 Johnston, K. J., and de Vegt, C. (1986). *Highlights Astron.* **7**, 103.
 Kaplan, G. H., editor (1981). U. S. Naval Obs. Circ. No. 163.
 Ma, C., Clark, T. A., Ryan, J. W., Herring, T. A., Shapiro, I. I., Corey, B. E., Hinteregger, H. F., Rogers, A. E. E., Whitney, A. R., Knight, K. A., Lundqvist, G. L., Shaffer, D. B., Vandenberg, N. R., Pigg, J. C., Schipler, B. R., and Ronnang, B. O. (1986). *Astron. J.* **92**, 1020.
 Shao, M., Colavita, M. M., Hines, B. E., Staelin, D. H., Hutter, D. J., Johnston, K. J., Mozurkewich, D., Simon, R. S., Hershey, J. L., Hughes, J. A., and Kaplan, G. H. (1988). *Astron. Astrophys.* (in press).
 Shao, M., Colavita, M. M., Staelin, D. H., Johnston, K. J., Simon, R. S., Hughes, J. A., and Hershey, J. L. (1987). *Astron. J.* **95**, 1280.